

Ingvild Mariannedatter Solheim

# Effect of Stockbridge Dampers on the Vibration Response of Suspension Bridge Hangers

Master's thesis in Mechanical Engineering

Supervisor: Ole Andre Øiseth

Co-supervisor: Knut Andreas Kvåle, Tengjiao Jiang

June 2022





Ingvild Mariannedatter Solheim

# **Effect of Stockbridge Dampers on the Vibration Response of Suspension Bridge Hangers**

Master's thesis in Mechanical Engineering  
Supervisor: Ole Andre Øiseth  
Co-supervisor: Knut Andreas Kvåle, Tengjiao Jiang  
June 2022


Norwegian University of Science and Technology  
Faculty of Engineering  
Department of Structural Engineering





## MASTER THESIS 2022

SUBJECT AREA: Structural Dynamics	DATE: 08.06.2022	NO. OF PAGES: 13+46+17
--------------------------------------	---------------------	---------------------------

TITLE: <b>Effect of Stockbridge Dampers on the Vibration Response of Suspension Bridge Hangers</b>  Effekten av Stockbridge Dempere på Vibrasjoner i Hengestengene på en Hengebro	
BY:  Ingvild Mariannedatter Solheim	

SUMMARY: Vibrations in the hangers at the Hålogaland bridge caused by shedding vortices was observed in the completing stages of the construction of the bridge. Vibration mitigating Stockbridge dampers were installed, but several of the dampers failed during a storm shortly after installation. Uncertainty regarding the cause of the failure remain. To evaluate the possible causes of failure, investigations of the damper behaviour and hanger response needs to be carried out. Consequently, the objective of this thesis is to characterize the vibration response of the hangers at the Hålogaland bridge and analyze the effect the dampers have on these vibrations. For this purpose, damper tests are performed to obtain information regarding the energy dissipation and displacement response of the damper for different exciting frequencies. The time-varying vibration response of the hangers are analyzed through the application of the short-term Fourier transform, enabling the comparison of the contemporaneous wind conditions and hanger responses. Theoretical shedding frequencies are compared to the measured vibration frequencies of the hangers to verify the cause of the vibrations. The presence and magnitude of the response is characterized based on the wind-direction and its inherent stability, the wind magnitude, and the magnitude of the turbulence. Through the analysis of time series known to induce vortex induced vibrations, differences in response of the hangers with and without dampers are evaluated. Comparisons on the differences in response due to various damper installations will be made both with respect to the same hanger over time, and with respect to different hangers within the same time series. Findings include that the vibration response of the hangers are closely aligned with the theoretical shedding frequencies. Furthermore, measurement data indicate that the dampers are highly effective in mitigating vibrations of frequencies lower than 25 Hz, whereas the damper effect is found to be negligible for frequencies upwards of 30 Hz. These observations from the measurement data are in good correspondence with the results from the damper tests. Finally, possible causes of damper failure and measures to reduce the magnitude of vibrations are discussed.
---

RESPONSIBLE TEACHER: Prof. Ole Andre Øiseth
SUPERVISOR(S): Ph.D. Knut Andreas Kvåle, Ph.D. Tengjiao Jiang
CARRIED OUT AT: The Department of Structural Engineering, NTNU.

## **Abstract**

Vibrations in the hangers at the Hålogaland bridge caused by shedding vortices was observed in the completing stages of the construction of the bridge. Vibration mitigating Stockbridge dampers were installed, but several of the dampers failed during a storm shortly after installation. Uncertainty regarding the cause of the failure remain. To evaluate the possible causes of failure, investigations of the damper behaviour and hanger response needs to be carried out. Consequently, the objective of this thesis is to characterize the vibration response of the hangers at the Hålogaland bridge and analyze the effect the dampers have on these vibrations.

For this purpose, damper tests are performed to obtain information regarding the energy dissipation and displacement response of the damper for different exciting frequencies. The time-varying vibration response of the hangers are analyzed through the application of the short-term Fourier transform, enabling the comparison of the contemporaneous wind conditions and hanger responses. Theoretical shedding frequencies are compared to the measured vibration frequencies of the hangers to verify the cause of the vibrations. The presence and magnitude of the response is characterized based on the wind-direction and its inherent stability, the wind magnitude, and the magnitude of the turbulence. Through the analysis of time series known to induce vortex induced vibrations, differences in response of the hangers with and without dampers are evaluated. Comparisons on the differences in response due to various damper installations will be made both with respect to the same hanger over time, and with respect to different hangers within the same time series. Findings include that the vibration response of the hangers are closely aligned with the theoretical shedding frequencies. Furthermore, measurement data indicate that the dampers are highly effective in mitigating vibrations of frequencies lower than 25 Hz, whereas the damper effect is found to be negligible for frequencies upwards of 30 Hz. These observations from the measurement data are in good correspondence with the results from the damper tests. Finally, possible causes of the damper failure are discussed based on the findings from the measurement data and the damper tests. Both fatigue failure and aerodynamic instabilities causing large amplitude vibrations were considered feasible causes for the damper failure. Measures to reduce the magnitude of both types of vibrations are introduced.

## Sammendrag

Vibrasjoner i hengestengene på Hålogalandsbrua forårsaket av virvelavløsning ble observert under byggingen av broen. Vibrasjonsdemperer ble installert for å redusere amplituden til vibrasjonene, men flere av demperne ble ødelagt under en storm som inntraff kort tid etter installasjon. Usikkerheten rundt årsaken til at demperne ble ødelagt består. For å finne årsaken til ødeleggelsene er det nødvendig å gjennomføre undersøkelser av oppførselen til demperne og responsen i hengestengene. Følgelig er hovedmålet med denne oppgaven å karakterisere vibrasjonene i hengestengene på Hålogalandsbrua samt analysere effekten demperne har på disse vibrasjonene.

I denne sammenheng er dempertester utført med mål om få økt kunnskap angående responsen av demperen og energien den tar opp ved forskjellige frekvenser. Vibrasjonene i hengestengene er analysert ved bruk av *short-term Fourier transform* som viser det varierende frekvensinnholdet i målingene over tid. Dette muliggjør sammenligning av vindmålinger og korresponderende frekvensinnhold i vibrasjonene av hengestengene. Teoretiske virvelavløsnings-frekvenser blir sammenlignet med frekvensene i responsen til hengestengene, for å verifisere at virvelavløsning faktisk er årsaken til vibrasjonene. Forekomsten og amplituden på vibrasjonene er karakterisert ut ifra retningen på vinden samt stabiliteten i denne retningen, vindhastigheten, og intensiteten i turbulensen i vinden. Forskjellene i respons for hengestengene med demper kontra uten blir analysert ved å se på måledata der vindmålingene, ut i fra tidligere funn, tilsier at virvelavløsning vil skape store vibrasjoner. Eventuelle forskjeller i respons forårsaket av et ulikt antall demperer på hengestengene blir evaluert både ved å sammenligne responsen i forskjellige hengestenger på samme tidspunkt, men også ved å sammenligne samme hengestang ved forskjellige tidspunkter. Måledataen impliserer at vibrasjonene i hengestengene på Hålogalandsbrua og de teoretiske virvelavløsnings-frekvensene basert på vindmålingene er tilnærmet identiske. Videre observasjoner fra måledataen tilsier at demperne fungerer svært godt for vibrasjoner med tilhørende frekvenser under 25 Hz. I motsetning til dette indikerer måledataen at effekten av demperen er neglisjerbar for frekvenser over 30 Hz. Resultatene fra dempertestene viser samme trend som måledataen, med redusert effekt for høyere frekvenser. Avslutningsvis diskuteres mulige årsaker til at demperne ble ødelagt basert på funn fra måledataen og resultater fra dempertestene. Blant mulige årsaker til hendelsen blir både utmattingsbrudd og vibrasjoner med tilhørende store amplituder som følge av aerodynamisk ustabilitet trukket frem. Mulige tiltak for å redusere begge de to typene vibrasjons-respons er foreslått.

## **Acknowledgements**

I would like to thank my supervisor Professor Ole Andre Øiseth and co-supervisors Ph.D. Knut Andreas Kvåle and Ph.D. Tengjiao Jiang for the academic support throughout this thesis.

A special thanks to Ole Andre Øiseth and Knut Andreas Kvåle for the guidance on the analysis of the measurement data and signal processing related to this work. Likewise, a special thanks to Tengjiao Jiang for all the help on the damper test, executed in the lab here at NTNU.

## List of Abbreviations

CF	Cross-flow
DOF(s)	Degree(s) of Freedom
DFT	Discrete Fourier Transform
FFT	Fast Fourier Transform
IDFT	Inverse Discrete Fourier Transform
IL	In-line
PSD	Power Spectral Density
RMS	Root Mean Square
SD	Stockbridge Damper
TF	Time Frequency
TMD	Tuned Mass Damper
VIV	Vortex Induced Vibrations

## List of Figures

1.1	Illustrating figure of a single-hanger suspension bridge. . . . .	14
2.1	Aliasing. . . . .	18
2.2	Time series and PSD of a narrow band process, figure adapted from <i>An introduction to random vibrations, spectral &amp; wavelet analysis</i> <sup>[1]</sup> . . . . .	19
2.3	Time series and PSD of a broad band process, figure adapted from <i>An introduction to random vibrations, spectral &amp; wavelet analysis</i> <sup>[1]</sup> . . . . .	20
2.4	Spectrogram. . . . .	20
3.1	Cross-flow and in-line vibration response. . . . .	22
3.2	Lock-in phenomenon, figure adapted from <i>Theory of Bridge Aerodynamics</i> <sup>[2]</sup> . . . . .	22
3.3	Theoretical shedding frequencies for the hangers at the Hålogaland bridge. . . . .	23
4.1	Stockbridge damper, figure adapted from Hubbell <sup>[3]</sup> . . . . .	24
4.2	Node and anti-node placing of the damper. . . . .	24
4.3	Energy dissipation of the SD given in terms of Watts, as presented in <i>TESolution damper performance test</i> . . . . .	25
4.4	Damper test setup. . . . .	26
4.5	Displacements for an excitation frequency of 15 Hz and RMS of $5 \text{ m/s}^2$ . Courtesy of Tengjiao Jiang. . . . .	27
4.6	Displacements for an excitation frequency of 21 Hz and RMS of $5 \text{ m/s}^2$ . Courtesy of Tengjiao Jiang. . . . .	27
4.7	Displacements for an excitation frequency of 23 Hz and RMS of $5 \text{ m/s}^2$ . Courtesy of Tengjiao Jiang. . . . .	28
4.8	Displacements for an excitation frequency of 25 Hz and RMS of $5 \text{ m/s}^2$ . Courtesy of Tengjiao Jiang. . . . .	28
4.9	Displacements for an excitation frequency of 30 Hz and RMS of $5 \text{ m/s}^2$ . Courtesy of Tengjiao Jiang. . . . .	29
5.1	Sensor overview south end. . . . .	31
5.2	Cardinal directions and local directions at the bridge site, map images from Kartdata ©2022. . . . .	32
5.3	Damper and accelerometer installations on hanger 1 and 3 at the Hålogaland bridge. . . . .	33
6.1	Faulty measurements for directions of $180^\circ$ . . . . .	35
6.2	Vibration response and corresponding wind measurements. . . . .	37
6.3	Turbulence intensity. . . . .	37
6.4	Spectrograms of vibration response in hanger 1. . . . .	37
6.5	VIV in x-direction for mean wind range 10-18 m/s. . . . .	38
6.6	VIV in x-direction for mean wind range 2.5-10 m/s. . . . .	38
7.1	Wind measurements from time series started at 08:00 the 16 <sup>th</sup> of July 2021 . . . . .	40
7.2	Response time series, 16 <sup>th</sup> of July 2021. . . . .	40
7.3	Standard deviations of response, 16 <sup>th</sup> of July 2021. . . . .	41
7.4	Spectrograms of vibrations in x-direction, 16 <sup>th</sup> of July 2021. . . . .	41
7.5	Wind measurements from time series started at 08:00 the 19 <sup>th</sup> of July 2021 . . . . .	42
7.6	Response time series, 19 <sup>th</sup> of July 2021. . . . .	43
7.7	Standard deviations of response, 19 <sup>th</sup> of July 2021. . . . .	43
7.8	Spectrograms of vibrations in x-direction, 19 <sup>th</sup> of July 2021. . . . .	44
7.9	Wind measurements from time series started at 16:00 the 27 <sup>th</sup> of February 2022 . . . . .	45
7.10	Response time series, 27 <sup>th</sup> of February 2022. . . . .	45
7.11	Standard deviations of response, 27 <sup>th</sup> of February 2022. . . . .	46
7.12	Spectrograms of vibrations in x-direction, 27 <sup>th</sup> of February 2022. . . . .	46
7.13	Wind velocities and corresponding standard deviations of vibrations in x-direction for hanger 1. . . . .	47
7.14	Standard deviations of vibrations in x-direction for hanger 2. . . . .	48
7.15	Standard deviations of accelerations in y-direction. . . . .	48
8.1	Ice accretion on hangers. . . . .	53
8.2	Displacements for an excitation frequency of 5 Hz and RMS acceleration of $2 \text{ m/s}^2$ . Courtesy of Tengjiao Jiang. . . . .	55



8.3	Illustration of helical strakes and dimples. . . . .	57
A.1	Sensor overview . . . . .	64
A.2	Anemometer at hanger 7, mounted to the south-side of the hanger. . . . .	65
A.3	Connection of the hangers to the bridge deck, with equivalent connections to the main cables. . .	66
B.1	Tracking points with corresponding numbering. . . . .	67

# Contents

<b>1</b>	<b>Introduction</b>	<b>14</b>
1.1	Background . . . . .	14
1.2	Problem Description . . . . .	15
<b>2</b>	<b>Dynamic Formulations and Signal Processing</b>	<b>16</b>
2.1	Modal Analysis . . . . .	16
2.2	Random Processes . . . . .	16
2.2.1	Correlation and Auto-Correlation . . . . .	17
2.3	Frequency Analysis . . . . .	17
2.3.1	Fourier Analysis . . . . .	17
2.3.2	Sampling . . . . .	18
2.3.3	Window . . . . .	18
2.3.4	Power Spectral Density . . . . .	19
2.3.5	Bandwidth of Signal . . . . .	19
2.4	Time-Frequency Analysis . . . . .	20
2.4.1	Short-Term Fourier Transform . . . . .	20
<b>3</b>	<b>Wind-induced Vibrations</b>	<b>21</b>
3.1	Wind Field Characteristics . . . . .	21
3.2	Vortex Induced Vibrations . . . . .	21
3.2.1	Lock-in Phenomenon . . . . .	22
3.2.2	Theoretical Shedding Frequencies at the Hålogaland Bridge . . . . .	22
<b>4</b>	<b>Stockbridge Damper</b>	<b>24</b>
4.1	Dynamics of the Stockbridge Damper . . . . .	24
4.1.1	Location of the Damper . . . . .	24
4.2	TESolution Damper Performance Test . . . . .	25
4.3	Damper Test of Displacement Response . . . . .	25
4.3.1	Results . . . . .	27
<b>5</b>	<b>Data Collection and Processing</b>	<b>31</b>
5.1	Measurement System . . . . .	31
5.1.1	Accelerometers on Hangers . . . . .	31
5.1.2	Anemometers . . . . .	32
5.2	Damper Installations at the Hålogaland Bridge . . . . .	33
5.3	Processing of Measurement Data . . . . .	34
5.3.1	Pre-processing . . . . .	34
5.3.2	Post-processing . . . . .	34
<b>6</b>	<b>Presence and Magnitude of Vortex Induced Vibrations</b>	<b>35</b>
6.1	Direction of the Wind . . . . .	35
6.1.1	Tower Shadowing . . . . .	35
6.1.2	Wind Directions Causing Vortex Induced Vibrations . . . . .	36
6.2	Turbulent Conditions . . . . .	36
6.2.1	Magnitude of the Turbulence . . . . .	36
6.2.2	Stability in Wind Direction . . . . .	38
6.3	Mean Wind Range . . . . .	38
<b>7</b>	<b>Effect of Dampers</b>	<b>40</b>
7.1	Vibration Response Characteristics . . . . .	40
7.1.1	Dampers on Selected Hangers . . . . .	40
7.1.2	Dampers on all Hangers . . . . .	45
7.2	Operating Range of the Stockbridge Damper . . . . .	47

7.2.1	Effect of Multiple Dampers	48
7.2.2	Damper Effectiveness for Small Response Amplitudes	48
7.3	Causes of Error in Response Analysis	49
7.3.1	Turbulence Levels	49
7.3.2	Temperature Effects	49
7.3.3	Basis of Comparison	50
<b>8</b>	<b>Discussion</b>	<b>51</b>
8.1	Correspondence of the Damper Tests and Measurement Data	51
8.2	Possible Causes of Damper Failure	52
8.2.1	Background Information	52
8.2.2	Large Amplitude Vibrations	52
8.2.3	Fatigue Life of the Damper	54
8.2.4	Lessons from the Damper Test	54
8.3	Measures to Reduce the Magnitude of the Vibrations	56
8.3.1	Amount of Dampers and Damper Location	56
8.3.2	Surface Roughness of Hangers	56
8.3.3	Hanger Material	57
8.4	Limitations of the Study	57
<b>9</b>	<b>Conclusion</b>	<b>58</b>
9.1	Further Work	58
	<b>Appendix</b>	<b>62</b>
A	Technical Drawings and Installation Configurations	63
A.1	Sensor Overview	63
A.2	Anemometer Installation	65
A.3	Connections of the Hangers	66
B	Damper-test	67
B.1	Tracking Points	67
C	Python-scripts	68
C.1	clean_data.py	68
C.2	functions.py	69
C.3	acc_response.py	70

# 1 Introduction

## 1.1 Background

Due to the low traffic load, suspension bridges constructed to serve as fjord-crossings in Norway are especially light, slender and flexible, making the structures more susceptible to aerodynamic instabilities<sup>[4]</sup>. The bridge deck of a suspension bridge is usually examined in a wind tunnel prior to construction. In contrast, hangers are installed with vibration mitigating measures during the completing stages of the bridge construction if vibrations are observed. As research imply, vibrations in the cables of cable-stayed bridges, and in the hangers of suspension bridges, is a recurrent problem<sup>[5;6]</sup>. There are many different types of vibration response, but a commonly observed one is the vibrations caused by shedding vortices, often referred to as vortex induced vibrations (VIV)<sup>[7]</sup>. A theoretical relation for the estimation of the shedding frequencies exists, and is dependent upon the wind magnitude and the nature of the cross section subjected to the wind flow<sup>[2]</sup>. Although the response related to VIV rarely induces critical levels of stresses in the material, dampers are often installed as the vibrations significantly reduces the fatigue life<sup>[8]</sup>. As for the specific type of damper, the Stockbridge damper(SD) is an obvious choice for suspension bridges with single hangers, like the Hålogaland bridge. Other damping systems often require physical connections to the bridge deck, or connections between the individual cables or hangers, only compatible with stay-cable bridges or suspension bridges where hangers are located in close proximity of each other<sup>[9]</sup>.

The Hålogaland bridge was opened to traffic the 9<sup>th</sup> of december 2018, eliminating the previously hazardous road stretch connecting Narvik and Øyjord, and shortening the European route E6 by 18 km. The bridge has a main span of 1145 meters and is currently the second longest suspension bridge in Norway, only outdone by the Hardanger bridge at 1380 meters. Shortly prior to the completion of the Hålogaland bridge, vibrations in the hangers caused by shedding vortices was observed. SD's were installed to mitigate these vibrations, and worked perfectly fine until several of the dampers failed during the storm Frank in early 2021<sup>[10]</sup>. Uncertainty regarding the cause of the failure remain. Consequently, investigations have been initiated to evaluate the damper behaviour and hanger response in search of the cause of the damper failure.

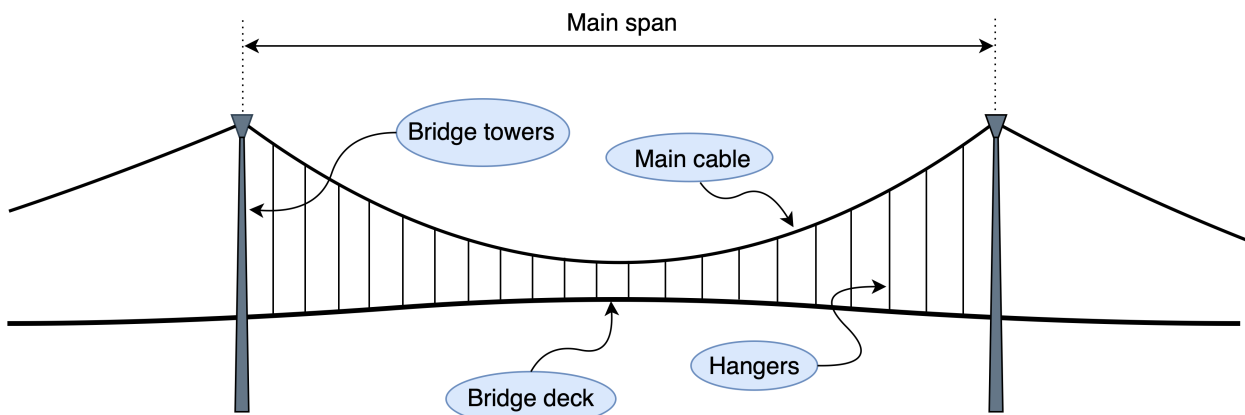


**Figure 1.1:** Illustrating figure of a single-hanger suspension bridge.

## 1.2 Problem Description

The overall objective of this thesis is to characterize the vibration response of the hangers at the Hålogaland bridge, and analyze the effect the dampers have on these vibrations. To carry out this research, damper tests are performed to evaluate the response and effectiveness of the dampers for different exciting frequencies. Furthermore, measurement data from the hangers at the Hålogaland bridge is investigated, where the response of the hangers without any dampers are compared to the response of the combined hanger-damper system.

An identical damper to the ones installed at the Hålogaland bridge is investigated in the lab here at NTNU, and by the producer *TESolution*. Displacements of various points along the damper was measured for different excitation frequencies during the damper test executed at NTNU. The producer of the dampers, *TESolution*, performed a test measuring the energy dissipation through the damper for different frequencies. Evaluated together, the two damper tests provide an overview of the damper behaviour and properties to be compared with the measurement data from the bridge site.

Measurement data from the three longest hangers at the south end of the bridge, all installed with accelerometers, is investigated in this thesis. Theoretical shedding frequencies for the hangers are derived based on the measured mean wind velocity, sampled at the anemometer located closest to the studied hangers. Thereafter, the measured vibration frequencies of the hangers are compared to the theoretical shedding frequencies to verify the cause of vibration. Based on findings in the measurement data, the presence and magnitude of the vibrations for different wind conditions such as wind direction, wind magnitude and turbulence levels will be described. Throughout the measurement period there has been variations in the damper installations on the hangers. Measurements from 2021 include data where the three studied hangers had either one, two and no dampers installed. For the measurement period in 2022, all hangers were installed with two dampers. Based on time series of wind conditions found to induce large amplitude vibrations in the hangers, the differences in response of the hangers with and without dampers will be analyzed. Comparisons on the differences in response due to various damper installations will be made both with respect to the same hanger over time, and with respect to different hangers within the same time series.

The ability of the damper to dissipate energy from the hanger vibrations will be described, where findings from the damper tests are compared to the response of the combined hanger-damper system. Furthermore, possible causes of damper failure based on measurement observations, available data from the damper tests and other research will be discussed. Also included are suggestions of measures to reduce the magnitude of vibrations in the hangers, as well as limitations and deficiencies in the conducted research.

## 2 Dynamic Formulations and Signal Processing

This chapter will provide the reader with a brief introduction to dynamic formulations and signal processing applied in processing and analysis of the data covered in this thesis.

### 2.1 Modal Analysis

Modal analysis is based on explicit equations formulated in terms of known system properties, such as stiffness and mass, where the aim is to describe the dynamic response of the given system<sup>[11]</sup>. The governing equation of a dynamic system is often referred to as the equation of motion, as given in equation 2.1. This equation gives the dynamic equilibrium of a linear system in the time domain. Following this equation, the dynamic system can be characterized by deterministic values for natural frequencies and corresponding mode shapes. Given a discretized system of  $N$  degrees of freedom (DOFs), the mass matrix  $\mathbf{M}$ , viscous damping matrix  $\mathbf{C}$  and stiffness matrix  $\mathbf{K}$  will be of dimension  $N \times N$ .

$$\mathbf{M}\ddot{\mathbf{u}}(t) + \mathbf{C}\dot{\mathbf{u}}(t) + \mathbf{K}\mathbf{u}(t) = \mathbf{p}(t) \quad (2.1)$$

Neglecting the effects of damping, the steady state free vibration response is governed by:

$$\mathbf{M}\ddot{\mathbf{u}}(t) + \mathbf{K}\mathbf{u}(t) = \mathbf{0} \quad (2.2)$$

Where the displacement vector  $\mathbf{u}$  can be expressed as:

$$\mathbf{u} = \text{Re}(\Phi e^{i\omega t}) \quad (2.3)$$

Combining equation 2.2 and 2.3, the resulting equation may be written as:

$$(\mathbf{K} - \omega_n^2 \mathbf{M}) \phi_n = \mathbf{0}, \quad \text{For } n = 1, 2, \dots, N \quad (2.4)$$

which is formally known as the eigenvalue problem. The solution to the eigenvalue problem gives the eigenvalues or natural frequencies of the system,  $\omega_n$ , and the corresponding eigenvectors or mode shapes,  $\phi_n$ , to each of the  $N$  modes of the system. Each mode shape  $\phi_n$  gives the response in all DOFs to the corresponding natural frequency  $\omega_n$ <sup>[12]</sup>. The total matrix of eigenvectors is given as:

$$\Phi = [\phi_1, \phi_2, \dots, \phi_N] \quad (2.5)$$

$$\phi_n = [\phi_{1n}, \phi_{2n}, \dots, \phi_{Nn}]^T \quad (2.6)$$

### 2.2 Random Processes

There are two different types of processes; deterministic processes and random processes. Deterministic processes are characterized by known input values, such as system parameters and loading, which enables the prediction of response in time and space. Random processes on the other hand are often characterized by random loads that can only be described in terms of probabilistic terms. In contrast to a deterministic process, the response of a system subjected to a load given by a random process can only be described in terms of probabilistic terms.

A random process, or stochastic process, is the term used to describe every possible realization of a random phenomenon<sup>[11]</sup>. A random process is often described in terms of expected value, as given in equation 2.7, and variance, as given in equation 2.8.  $p(x)$  is the corresponding probability density function for the given stochastic process  $x(t)$ <sup>[13]</sup>. The accuracy of the estimated parameters depend both on the length and the number of time series evaluated.

$$\mu_x(t) = E[x_k(t)] = \int_{-\infty}^{\infty} x_k(t) p(x) dx \quad (2.7)$$

$$\sigma_x^2(t) = E [(x_k(t) - \mu_x(t))^2] = \int_{-\infty}^{\infty} (x_k(t) - \mu_x(t))^2 p(x) dx \quad (2.8)$$

Assuming the process is a *weakly stationary process*, the mean value and variance of the process will be time invariant, resulting in  $\mu_x(t) = \mu_x$  and  $\sigma_x^2(t) = \sigma_x^2$ . Equivalently, if the statistical properties are space invariant, the stochastic process is said to be *homogeneous*.

Ensemble averaging is the process of averaging the statistical properties for several realizations of the stochastic process, to improve the estimates. For a total number of realizations,  $K$ , the statistical properties of each realization  $x_k(t)$  is averaged to obtain the statistical properties of the stochastic process  $x(t)$ , as given in 2.9<sup>[1]</sup>.

$$\mu_x = \frac{1}{K} \sum_{k=1}^K E [x_k(t)] \quad (2.9)$$

For a random process where all the statistical properties can be determined from a single sufficiently long time series, the process is said to be *ergodic*<sup>[11]</sup>.

### 2.2.1 Correlation and Auto-Correlation

Correlation is a measure of how two processes are related and coupled. The processes can be anti-correlated, uncorrelated or correlated, to different extents. Correlated processes gives correspondingly large values for both processes, anti-correlated processes gives correspondingly opposite extreme values of the processes. Lastly, if the processes are uncorrelated, there is no distinct pattern between the two processes.

Furthermore, correlation can be used to indirectly describe the frequency content of a time series. Assuming the stochastic process is stationary, the auto-correlation can be interpreted as the correlation of a time series with a time-shifted version of it self, and is given as in equation 2.10<sup>[1]</sup>.

$$R_{xx}(\tau) = E[x(t)x(t + \tau)] \quad (2.10)$$

## 2.3 Frequency Analysis

### 2.3.1 Fourier Analysis

A continuous and periodic signal with period  $T$  may also be represented as a sum of infinitely many harmonic components, referred to as a Fourier series, as given in equation 2.11. The Fourier series is composed of a constant part,  $a_0$ , representing the mean value of the signal. The other constants  $a_k$  and  $b_k$  represents the amplitudes of each harmonic component with corresponding frequency  $\omega_n$ , as given in equation 2.12.

$$x(t) = a_0 + \sum_{k=1}^{\infty} (a_k \cos(\omega_k t) + b_k \sin(\omega_k t)) \quad (2.11)$$

$$\omega_k = \frac{2\pi k}{T} \quad (2.12)$$

In the limit where  $T \rightarrow \infty$ , the frequency spacing  $\Delta\omega = \frac{2\pi}{T} \rightarrow 0$ , and we obtain the Fourier integral, also referred to as the continuous Fourier transform. The Fourier transform converts a signal from the time-domain representation to the frequency domain representation. In complex form, it is given as:

$$X(\omega) = \frac{1}{2\pi} \int_{-\infty}^{\infty} x(t) e^{-i\omega t} dt \quad (2.13)$$

The signal may also be converted back to the time domain through the inverse continuous Fourier Transform, given as:

$$x(t) = \int_{-\infty}^{\infty} X(\omega) e^{i\omega t} d\omega \quad (2.14)$$

For most processes, the continuous description of the time series is unknown and the process needs to be measured at discrete points in order to obtain a time history of the process. If the time series is sampled using sufficiently small time intervals, the reproduction of the signal is able to represent the original continuous time series. To obtain the frequency representation of the discrete signal, the Discrete Fourier transform (DFT) is applied, as given in equation 2.15. In the same way a continuous signal can be converted back from the frequency domain to the time domain using the inverse Fourier transform, a discrete signal can be converted back to the time domain by the application of the inverse discrete Fourier transform (IDFT), as given in equation 2.16<sup>[1]</sup>:

$$X_k = \frac{1}{N} \sum_{r=0}^{N-1} x_r e^{-2\pi i(\frac{kr}{N})}, \quad \text{For } k = 0, 1, 2, \dots, (N-1) \quad (2.15)$$

$$x_r = \sum_{k=0}^{N-1} X_k e^{2\pi i(\frac{kr}{N})}, \quad \text{For } r = 0, 1, 2, \dots, (N-1) \quad (2.16)$$

An effective and well known algorithm for calculations of the DFT is developed by *J. Cooley et al*, and referred to by the name Fast Fourier Transform (FFT)<sup>[14]</sup>.

### 2.3.2 Sampling

For the representation of a continuous signal through measurements, the original signal needs to be sampled at discrete points. The choice of sampling frequency needs to be carefully considered to avoid loss of information from the original signal. If the sampling frequency is not sufficient, aliasing may occur, which refers to the misinterpretation of the original signal, as shown in figure 2.1.

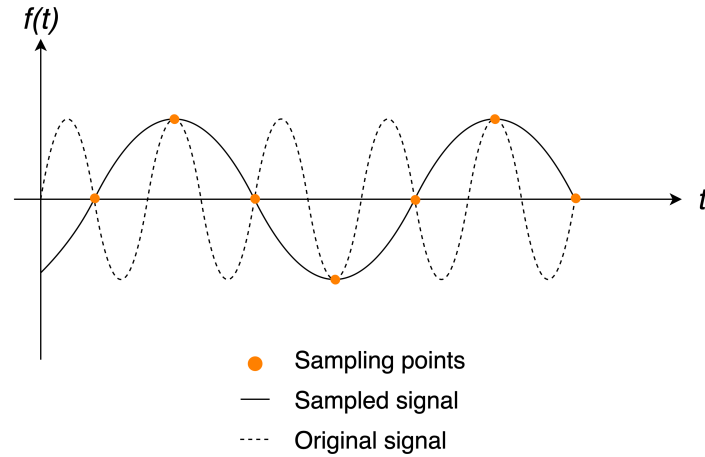


**Figure 2.1:** Aliasing.

To avoid loss of information from the original signal, the signal needs to be sampled at least two times per period, said in other words, the the sampling frequency needs to be at least two times the highest frequency of the signal. This sampling frequency is commonly referred to as the Nyquist frequency<sup>[15]</sup>. In some cases one may wish to reduce the sampling rate of a signal, for example to reduce the use of storage. Considering a discrete signal sampled at a given sample rate, the same signal may be represented by the use of less samples. Keeping only one out of every  $D$  samples to represent the signal is called *downsampling* by a factor of  $D$ <sup>[16]</sup>.

### 2.3.3 Window

The length of the window, of which the FFT is applied to, also effects the spectral content of the results. If the window size is chosen inappropriately to the signal, so that there are discontinuities at the ends of the sampled segment of the original signal, spectral leakage may occur. This is the phenomenon where amplitudes are falsely attributed to nearby frequencies of the actual signal, also resulting in lower amplitude for the original frequency of the signal<sup>[17]</sup>.



To reduce the effect of spectral leakage associated with the finite record length, spectral windows, or weighting functions as they are, are applied to the signal to reduce the discontinuities at the ends of the sampled segment. The window functions have amplitudes close or equal to zero at the end of the sampled segment, so that no discontinuities appear. To avoid loss of data due to the small amplitudes at the ends of each window, an overlap of segments is used<sup>[1]</sup>.

### 2.3.4 Power Spectral Density

The Fourier transform of the auto-correlation function is called the auto-spectral density, often referred to as the power spectral density(PSD), and is as given i equation 2.17. As the auto-correlation function and spectral density is Fourier transform pairs, one ends up at the auto-correlation function again if the inverse Fourier transform is applied to the PSD, as shown in equation 2.18.

$$S_{xx}(\omega) = \frac{1}{2\pi} \int_{-\infty}^{\infty} R_{xx}(\tau) e^{-i\omega\tau} d\tau \quad (2.17)$$

$$R_{xx}(\tau) = \int_{-\infty}^{\infty} S_{xx}(\omega) e^{i\omega\tau} d\omega \quad (2.18)$$

Setting  $\tau = 0$  in equation 2.18, one ends up with the following relation, manifesting that the area under the curve of the PSD is equal to the variance of the process. Following this, the PSD provides information regarding the distribution of the variance of the process, for different frequencies. The units of the spectral density will be the mean square per unit of frequency<sup>[1]</sup>.

$$R_{xx}(\tau = 0) = \int_{-\infty}^{\infty} S_{xx}(\omega) d\omega = E[x^2] \quad (2.19)$$

The PSD can either be given as a two-sided spectrum, containing both positive and negative frequencies, or as a one-sided spectrum, containing only positive frequencies and amplitudes twice of that the two-sided spectrum<sup>[11]</sup>.

### 2.3.5 Bandwidth of Signal

Processes are often characterized by the bandwidth of the signal. *Narrow band* is the term used for processes where the variance of the process is focused around a small frequency range. Typical for these processes are the similarities to harmonic oscillations, with one up-crossing per peak. An example of a narrow band process is included in figure 2.2, where to the left is a time series, and to the right is a PSD of the time series. Opposite of narrow band processes are *broad band* signals, or in the extreme case, white noise. These processes are composed of a wide range of frequencies, as shown in the PSD to the right in figure 2.3. To the left in the same figure is an example of a time series of a broad banded signal.

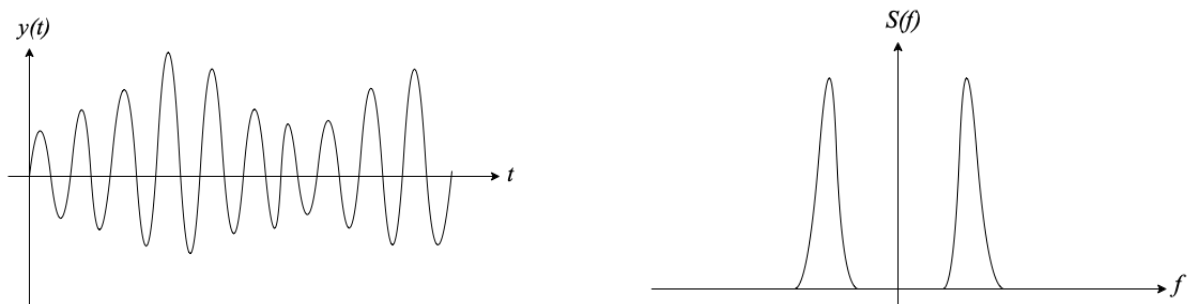


**Figure 2.2:** Time series and PSD of a narrow band process, figure adapted from *An introduction to random vibrations, spectral & wavelet analysis*<sup>[1]</sup>.

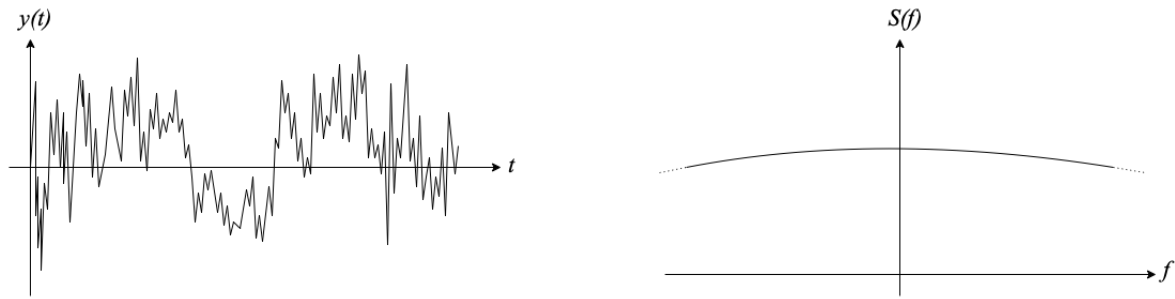


**Figure 2.3:** Time series and PSD of a broad band process, figure adapted from *An introduction to random vibrations, spectral & wavelet analysis*<sup>[1]</sup>.

When capturing an analogous signal by measurements at discrete points, unwanted high-frequency noise might occur in the representation of the signal. Likewise, for the previously mentioned leakage effect in section 2.3.3, unwanted frequency components contribute to contamination of the original signal. To remove these unwanted frequencies digital filters may be applied to the original signal, leaving a signal comprised of the desired frequencies only. In other cases, the original analogue signal is naturally comprised of several different frequency components, where only a certain range of frequencies are of interest. Here, band-pass filters may be used to isolate the wanted frequency range of the original signal<sup>[18]</sup>.

## 2.4 Time-Frequency Analysis

### 2.4.1 Short-Term Fourier Transform

Time-frequency (TF) signal processing methods enables the study of the frequency content of a non-stationary signal at a particular time<sup>[15]</sup>. One of the most well-known TF-techniques is called the *short-term Fourier transform* (STFT). This technique is based on dividing the original signal into smaller segments with a chosen overlap between the segments, before taking the Fourier transform of each of the segments. To reduce the effects of leakage, a window function is applied to each of the Fourier transforms comprising the total signal.

Window size needs to be of a certain length in order to capture the frequency of the oscillations in the signal, to provide good estimates of the vibration frequencies with a clear frequency resolution. However, a larger window size decreases the time localization of the results. Following this, the length of the window will always be a compromise between time localization and frequency resolution of the results<sup>[19]</sup>.

The results are often presented as a spectrogram, as shown in figure 2.4, where the color of the plot corresponds to the amplitude values of the PSD for the given sampled segment. The color ranges from dark blue to yellow, where dark blue color indicate amplitudes close to zero, and yellow indicate higher amplitudes. Consequently, scattered results of yellow color suggests that the signal is composed of a wider range of frequencies, whereas a clear yellow line focused around a smaller frequency range indicate the opposite, that the signal is more narrow-banded.

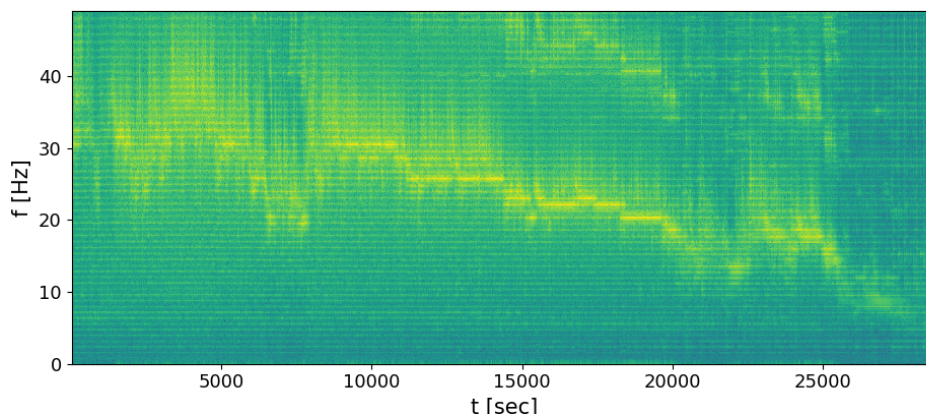


**Figure 2.4:** Spectrogram.

### 3 Wind-induced Vibrations

This chapter includes a brief description of wind-field characteristics and the theory of vortex induced vibrations in bluff bodies. Lastly, theoretical shedding frequencies related to vortex induced vibrations of the hangers at the Hålogaland bridge will be presented.

#### 3.1 Wind Field Characteristics

The presence and magnitude of wind-induced vibrations will vary depending on the wind-conditions, hence it is useful to introduce some statistical terms to describe the wind field. The wind flow, as a random process, is commonly separated in a constant part, the mean wind, and a fluctuating part, the turbulence of the wind flow. Assuming the random process is stationary, the mean wind may be calculated as the time averaged wind speed over a finite interval, as given in equation 3.1. Here,  $T$  denotes the length of the finite interval or window,  $V$  denotes the mean wind and  $V(t)$  denotes the time varying magnitude of the wind.

$$V = \frac{1}{T} \int_0^T V(t) dt \quad (3.1)$$

The turbulence intensity provides a measure that compares the magnitude of the fluctuating part to the constant part of the wind flow, and is given as in equation 3.2. Here,  $I$  denotes the turbulence intensity,  $\sigma$  denotes the standard deviation of the process, and  $V$  denotes the mean wind<sup>[20]</sup>.

$$I = \frac{\sigma}{V} \quad (3.2)$$

#### 3.2 Vortex Induced Vibrations

A particular type of wind-induced vibration response is the vortex induced vibrations(VIV). For a bluff body subjected to wind flow, a laminar boundary layer will be created along the structure surface. At some point, flow separation occurs creating shedding vortices in the wake of the structure. Typically, these vortices are shed alternately causing fluctuating loads on the structure, in turn giving rise to vibration response. The frequency of which the vortices are shed, and hereby also the frequency of which the fluctuating loads operate, is often referred to as the *vortex shedding frequency*,  $f_s$ , or just the *shedding frequency*. The numerical value of this frequency is in general a function of the mean wind velocity and the nature of the cross section of the structure. For a line-like structure with a circular cross section, the shedding frequency is given by the relation:

$$f_s = St \cdot \frac{V}{D} \quad (3.3)$$

where  $St$  is the Strouhal Number,  $V$  is the mean wind velocity and  $D$  is the the diameter of the cylinder<sup>[2]</sup>. The Strouhal Number is found to be approximately constant and equal to 0.185 for Reynold numbers corresponding to wind velocities in the range 1-30 m/s<sup>[21]</sup>. Vortex induced vibrations are comprised of two different types of vibration response; inline vibrations and cross-flow vibrations, as shown in figure 3.1. Cross-flow vibrations causes motion perpendicular to the oncoming flow direction, and will in general cause greater amplitudes and lower vibration frequencies compared to the inline vibrations. For a given mean wind and shedding frequency causing cross-flow vibrations, the inline vibration frequency will be twice of that the cross-flow vibration frequency, so that  $f_{s,inline} = 2 \cdot f_{s,cross-flow}$ <sup>[22]</sup>.

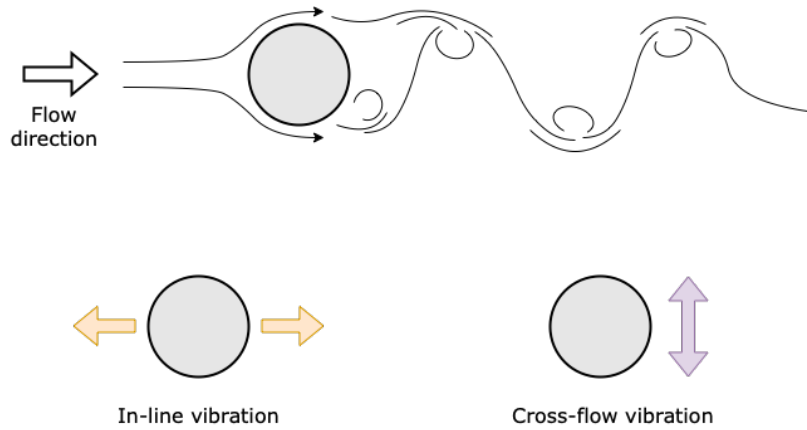


Figure 3.1: Cross-flow and in-line vibration response.

### 3.2.1 Lock-in Phenomenon

Theoretically, forces from shedding vortices operating at any shedding frequency corresponding to a natural frequency of the system, will cause resonant response. As the shedding frequency varies along with the magnitude of the wind, the wind-speed determines which mode of the structure is activated. For frequencies close to an eigenfrequency of the structure, interaction between the flow and the oscillating structure causes the shedding frequency to remain constant even for slightly varying wind speeds. Characteristics of this effect, the so called *lock-in phenomenon*, is shown in figure 3.2. This phenomenon can cause accelerations of large amplitudes, however, the effect is also self-limiting<sup>[23;2]</sup>.

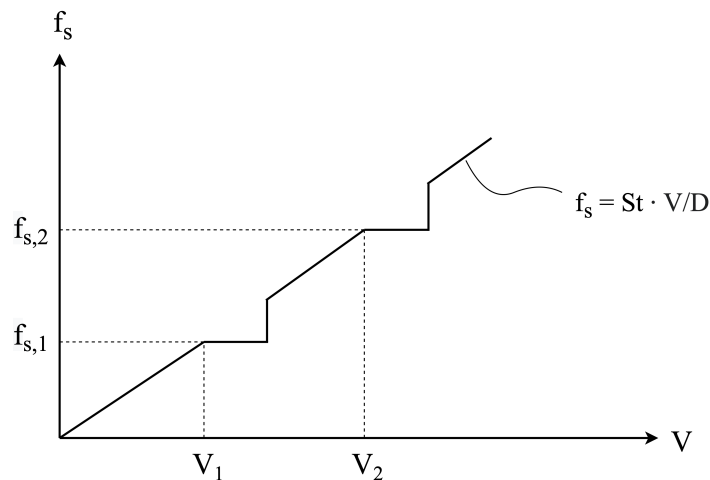
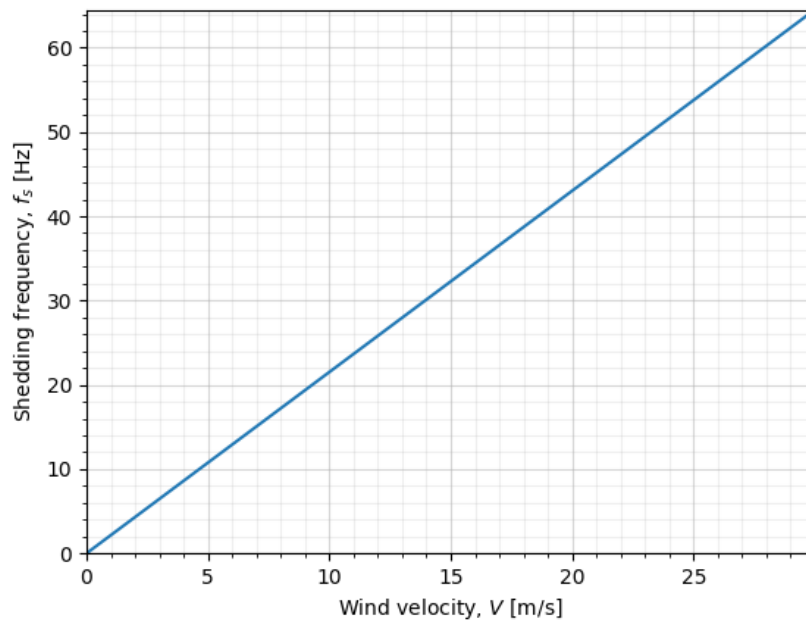


Figure 3.2: Lock-in phenomenon, figure adapted from *Theory of Bridge Aerodynamics*<sup>[2]</sup>

### 3.2.2 Theoretical Shedding Frequencies at the Hålogaland Bridge

The diameter of the hangers at the Hålogaland bridge is 86 mm, whilst a Strouhal number of 0.185 was used in the estimation of the theoretical shedding frequencies for the hangers. Following this, a relation between the wind velocity and shedding frequency as given in figure 3.3 was obtained. As shown in figure 3.2, the measured shedding frequencies for a cylinder would normally include steps of constant shedding frequencies around the natural frequencies of the structure. However, prediction of lock-in response is not included as the natural frequencies of a long cylinder in tension are closely spaced<sup>[24]</sup>. Following this, the actual vibration response and the corresponding shedding frequency is expected to be fairly well aligned with the theoretical shedding frequency. In addition, different wind characteristics and directions may also influence the response, even if the velocity of the wind remains constant. Following this, the reader is provided with theoretical shedding frequencies alone, with the notion that actual shedding frequencies may deviate depending on environmental conditions.



**Figure 3.3:** Theoretical shedding frequencies for the hangers at the Hålogaland bridge.

## 4 Stockbridge Damper

This chapter will cover the idea and dynamics behind the Stockbridge damper. Furthermore, two damper tests are included; a test measuring the energy dissipation through the damper at different frequencies and a test measuring the displacements of the damper at different frequencies.

### 4.1 Dynamics of the Stockbridge Damper

Stockbridge damper (SD) is a type of tuned mass damper used to suppress vortex induced vibrations of cables. The damper consists of a clamp that connects the damper to the hanger or cable, a messenger cable, and two masses at each end of the messenger cable, as shown in figure 4.1.

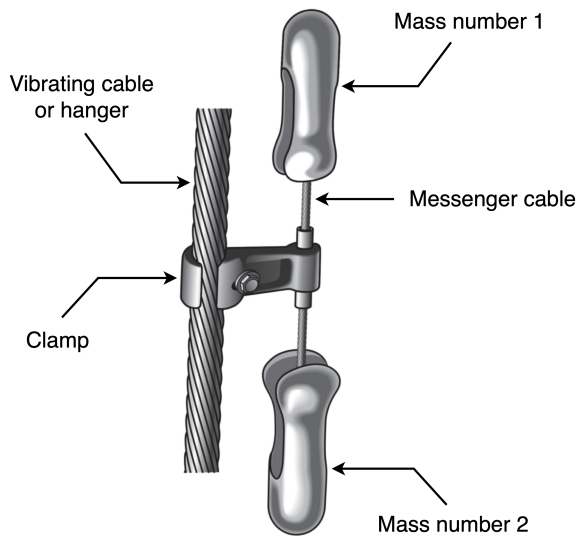


**Figure 4.1:** Stockbridge damper, figure adapted from Hubbell<sup>[3]</sup>

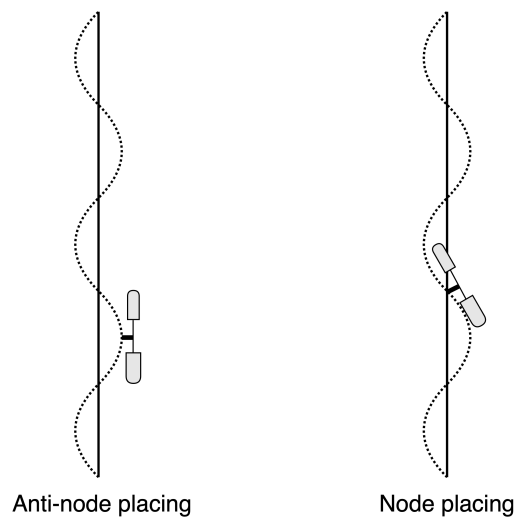


**Figure 4.2:** Node and anti-node placing of the damper.

Inherent damping and energy dissipation is quite high, owing to the internal sliding between the individual wires of the messenger cable, causing dry-friction during vibration<sup>[25]</sup>. Furthermore, the SD exerts non-linear damping behaviour in the sense that the amount of energy dissipated by the damper is highly dependent upon both vibration amplitude and vibration frequency<sup>[26;27]</sup>.

For structures in need of vibration mitigating measures, dampers are often altered to obtain the highest efficiency at the most critical frequencies for the structure, commonly referred to as frequency tuning. Frequency tuning is obtained through changing the masses or changing the length or diameter of the messenger cable. The damper may also be tuned to several vibration modes by making the damper asymmetric. This involves changing the position of the clamp on the messenger cable, or changing the masses so that they are unequal. Several dampers may also be installed for multi-mode vibration control<sup>[9]</sup>.

#### 4.1.1 Location of the Damper

The location of the damper also severely affects the ability of the damper to dissipate energy from the system. Placed closer to an anti-node of the given mode shape, the SD produces larger damping compared to the same SD placed at a node of the mode shape. Although the damper does offer some damping through the rocking motion in the node-position, as indicated in figure 4.2, the effect of the damper is significantly lower for this position<sup>[9;28]</sup>.

## 4.2 TESolution Damper Performance Test

The producer of the dampers at the Hålogaland bridge, TESolution, executed a damper performance test on some of the dampers from the bridge still intact after the storm Frank. Results from the damper test was presented in a report with restricted access and will consequently not be cited or appended to this thesis. However, selected content relevant for this thesis will be reproduced, where the original test report will be referred to as *TESolution damper performance test* or just *TESolution damper test*.

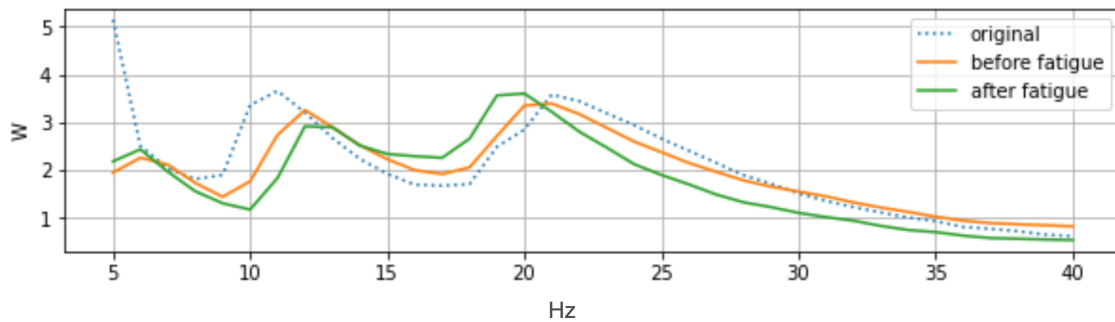


**Figure 4.3:** Energy dissipation of the SD given in terms of Watts, as presented in *TESolution damper performance test*.

One of the tests included in the report was a dynamic test where the amount of energy dissipated by the damper was measured. The tested damper was one of the original dampers sent to the Hålogaland bridge site, but had never been in use. The damper was mounted to an exciter where measurements were performed at a constant excitation velocity of  $0.1\text{ m/s}$ . Frequencies in the range of 5 to 40 Hz was tested, where an increment of 1 Hz was used. The results from the test are presented in figure 4.3, where the orange line represents the unused damper sent back from the bridge site, and the green line represents the same exact damper after it had undergone a fatigue test. The fatigue test included a total of  $10^7$  cycles, with an excitation frequency of 26 Hz and displacement amplitude of  $\pm 1\text{ mm}$ . As seen from the figure, the graph has 3 prominent peaks where the energy dissipation through the damper reaches a local maximum. The first and smallest one at around 7 Hz, the second one in the range 12-13 Hz, and the third and final one at around 20 Hz. For excitation frequencies above 20 Hz, the energy dissipation through the damper is monotonically decreasing. Also worth pointing out is the reduced damping effects for excitation frequencies above 20 Hz for the damper subjected to the fatigue test, compared to the unused damper.

## 4.3 Damper Test of Displacement Response

A SD equivalent to the ones installed at the Hålogaland bridge was tested in the lab at NTNU. The damper was mounted to a shaker where the the excitation motion was executed at a constant root mean square (RMS) value of the acceleration, causing different displacement amplitudes for different frequencies. Vibration response of the damper for different excitation frequencies, measured in terms of displacements, was investigated. Stickers were placed along the vertical centre-line of the damper, as shown in figure 4.4a, where the displacements of the given points was sampled. The sampling points were chosen carefully to obtain both the translational displacements as well as the rotational motion of the masses, each capable of inducing bending behaviour and dry friction in the messenger cable. The camera used to capture the response of the dampers, shown in figure 4.4b, had a sampling frequency of 260 Hz. Vibration shapes for each of the excitation frequencies tested for is presented by a series of 4 reproductions of the vibration shape of the damper, based on equally spaced samples within the span of one full single cycle of vibration response. The distance between the weakly dashed vertical lines in the figures correspond to a 1 mm distance in all the figures presented below, except for the figure with an excitation frequency of 15 Hz where the vertical lines are positioned at every 2 mm.



It should be pointed out that vibration shapes might vary slightly, as the excitation motion in many cases does not induce a perfect harmonic response in the different parts of the damper. Additionally, some cases where the exciter was not able to force a perfect harmonic displacement response was also observed. The ability of the exciter to induce a perfect harmonic response in point number 4, where point number 4 corresponds to the clamp of the damper as indicated in section B.1 of the appendix, seems to be dependent upon both the excitation frequency and the value of the RMS acceleration. Tests revealed that the exciter was not able to induce a perfect harmonic excitation for excitation frequencies in the range of 20-25 Hz and a corresponding RMS acceleration value of  $2 \text{ m/s}^2$ . In contrast, when the RMS acceleration was increased to a value of  $5 \text{ m/s}^2$ , the excitation motion was close to a perfect harmonic oscillation. For an excitation frequency of 30 Hz, opposite characteristics was observed. The excitation motion was close to a perfect harmonic oscillation for a RMS acceleration value of  $2 \text{ m/s}^2$ , whereas a RMS acceleration value of  $5 \text{ m/s}^2$  did not induce a perfect harmonic response. Nonetheless, the figures of the vibration response of the damper, as presented below, provides a reasonably good approximation, indicating which masses are activated for the different excitation frequencies and the corresponding displacement characteristics of this response.



(a) Stickers on the damper.



(b) Camera used to capture the motions.

**Figure 4.4:** Damper test setup.



### 4.3.1 Results

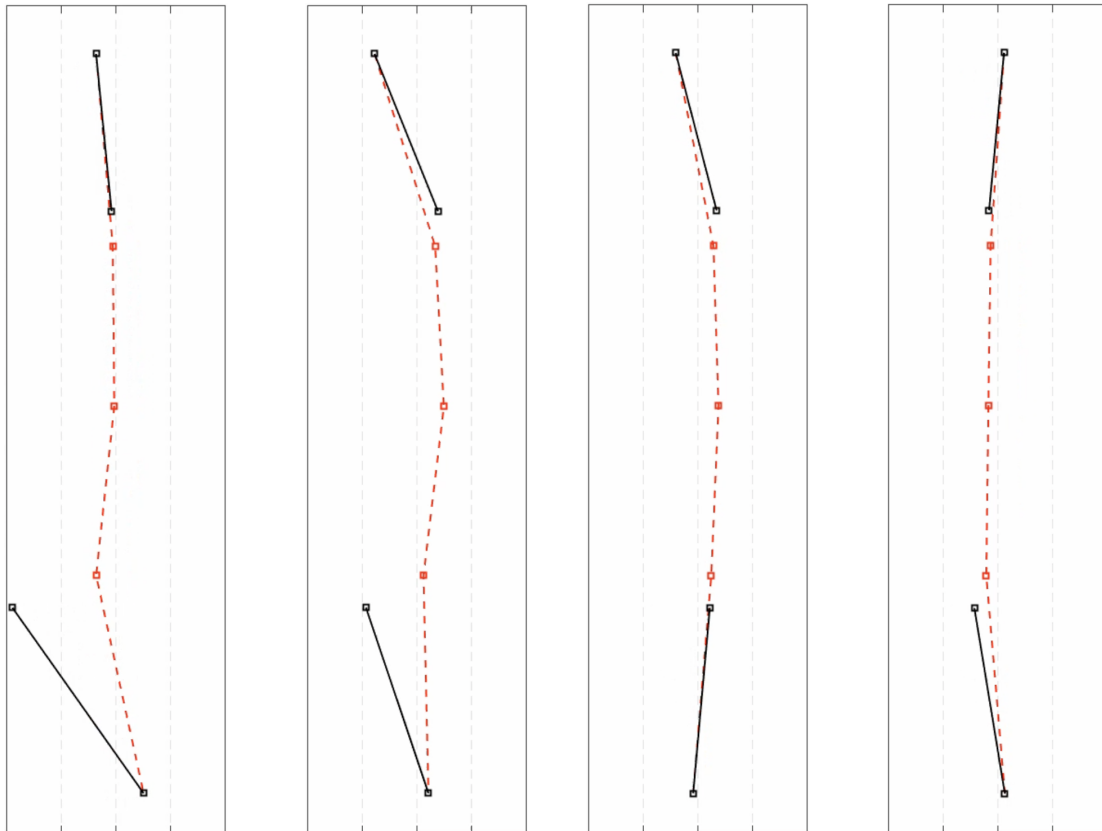


**Figure 4.5:** Displacements for an excitation frequency of 15 Hz and RMS of  $5 m/s^2$ . Courtesy of Tengjiao Jiang.

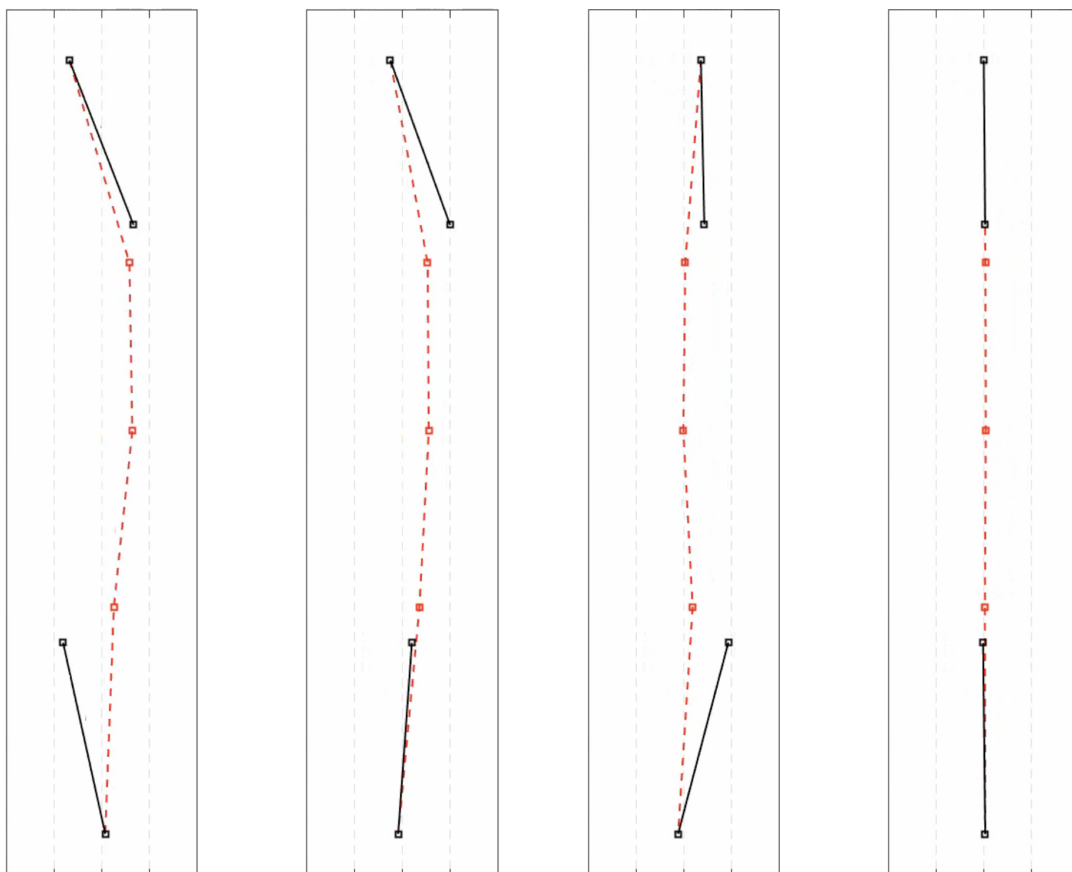


**Figure 4.6:** Displacements for an excitation frequency of 21 Hz and RMS of  $5 m/s^2$ . Courtesy of Tengjiao Jiang.

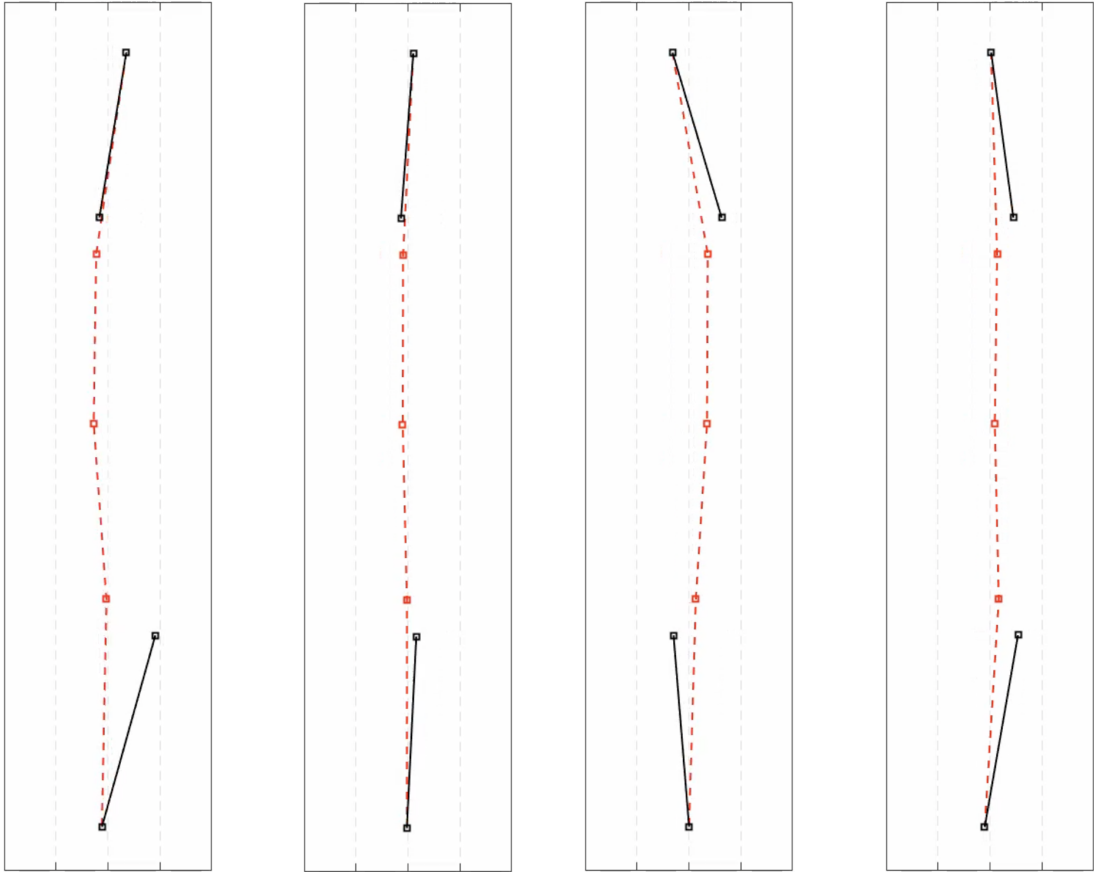


**Figure 4.7:** Displacements for an excitation frequency of 23 Hz and RMS of  $5 \text{ m/s}^2$ . Courtesy of Tengjiao Jiang.

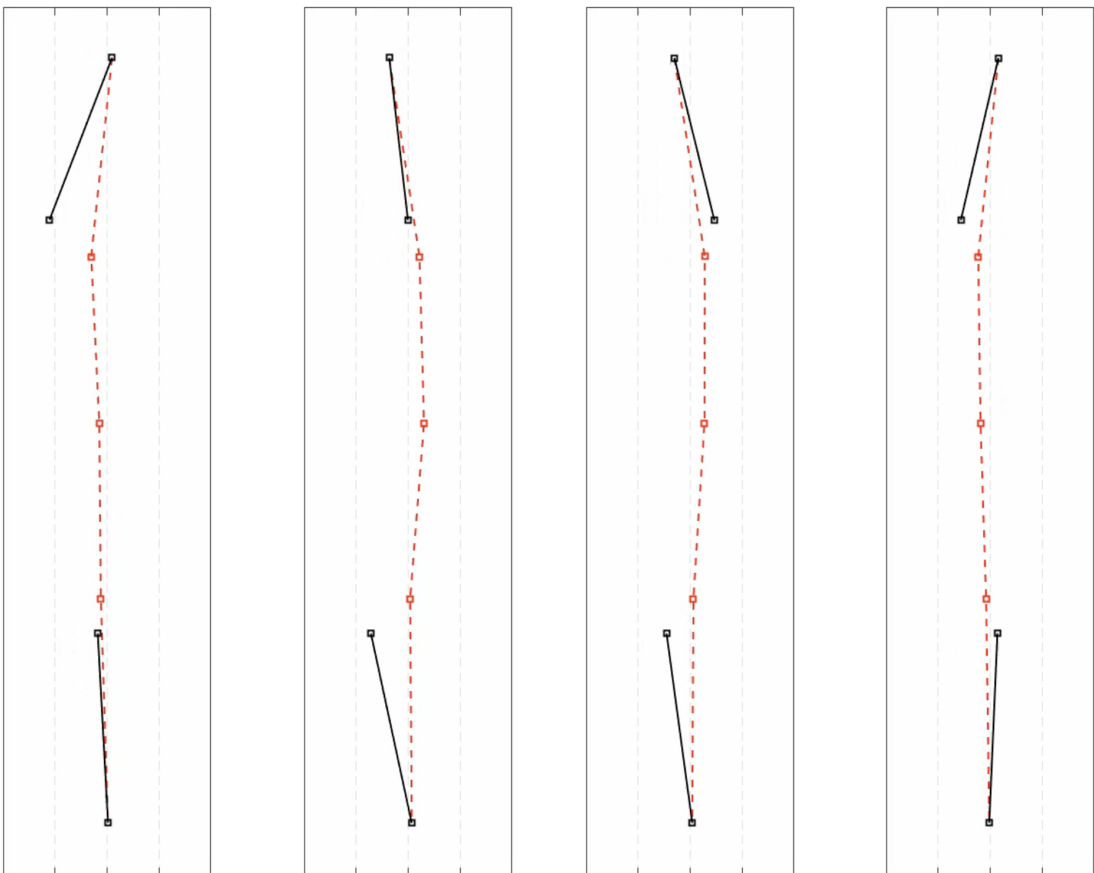


**Figure 4.8:** Displacements for an excitation frequency of 25 Hz and RMS of  $5 \text{ m/s}^2$ . Courtesy of Tengjiao Jiang.

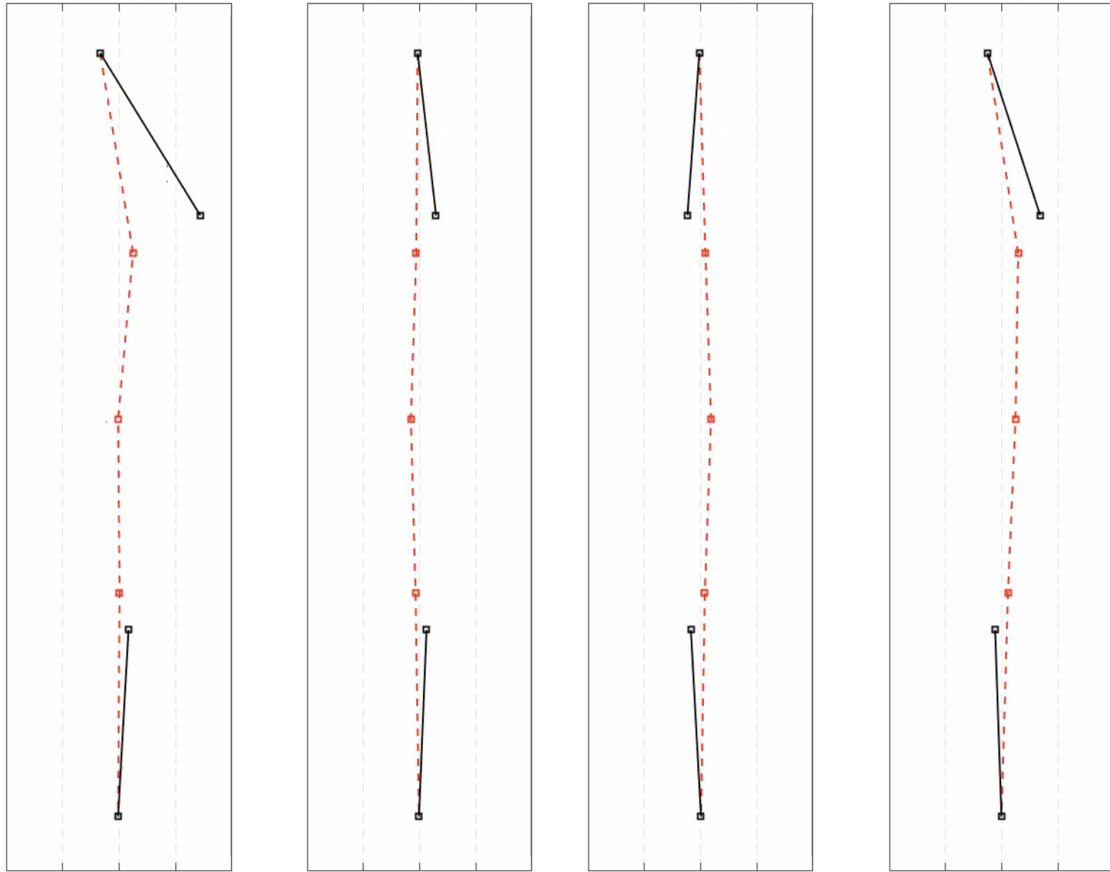


**Figure 4.9:** Displacements for an excitation frequency of 30 Hz and RMS of  $5 \text{ m/s}^2$ . Courtesy of Tengjiao Jiang.

For the excitation frequency of 15 Hz, shown in figure 4.5, the response of the bottom mass is relatively large, whilst the response of the top mass is smaller and more aligned with the curvature of the messenger cable. The excitation frequency of 21 Hz, shown in figure 4.6, demonstrate similar response characteristics as the previously introduced vibration shape. A rotational motion of the bottom mass occurs where the bottom-most sampling point has negligible displacements compared to the sampling point at the top of the bottom mass. The displacements of the top mass, in contrast to the bottom mass, are more aligned with the curvature of the messenger cable. Both the rotation of the bottom mass and the translation of the top mass will induce bending behaviour in the messenger cable, causing dry friction between the wires and dissipation of energy. Next, the excitation frequency of 23 Hz is shown in figure 4.7. There is bending in the top messenger cable, seen by the curvature of the displacements, while the rotation of the bottom mass causes bending in the bottom messenger cable. Although the displacements of the free end of the masses relative to the messenger cable is smaller for this excitation frequency compared to the previous ones, there is still curvature in the messenger cable, dissipating energy from the vibrations. Also worth noting is the fact that both masses are activated in the vibration response of the damper.

Figure 4.8 exemplify the displacements of the damper for an excitation frequency of 25 Hz. In contrast to the vibration shapes of lower excitation frequencies, the top mass now obtains larger responses. Additionally, the very top sampling point has far smaller displacements simultaneously as the displacements of the lower sampling point of the top mass is increased. This is similar response characteristics to what is observed in the bottom mass for the lower excitation frequencies. Likewise as for the previously introduced excitation frequencies, there is bending in both the top and bottom messenger cable, producing damping effects. For an excitation frequency of 30 Hz, presented in figure 4.9, there is a clear difference in response compared to the previous measurements. The bottom mass is now almost at a stand still, both with respect to rotational and translational response. In contrast, the response of the top mass is substantially larger, mainly characterized by a rotational response. The low degree of activation of the bottom mass causes negligible bending in the bottom messenger cable, and will correspondingly not be likely to produce any noteworthy energy dissipation through the bottom messenger cable.

The results demonstrate that different masses are activated as the excitation frequency goes from 15 Hz to 30 Hz. For an excitation frequency of 15 Hz, bending in both sections of the messenger cable occurs, however, the bottom mass obtains substantially larger displacements compared to the top mass. For the excitation frequency of 30 Hz, the response of the bottom mass is negligible whilst the response of the top mass is now characterized by a rotational response. In other words, the motion of the damper is transferred from the bottom mass to the top mass as the excitation frequency increases from 15 Hz to 30 Hz. However, as described in section 4.1, the response of the damper is dependent on both the excitation frequency and the amplitude of the excitation motion. As the test is performed by the use of a constant RMS value of the accelerations, the actual displacements of the excitation motion might differ to the ones in the measurement-data from the Hålogaland bridge, causing different damping effects.

## 5 Data Collection and Processing

This chapter will provide the reader with an overview of the measurement system installed at the Hålogaland bridge. The chapter also covers information of when measurements have been performed and the corresponding damper installations at the given time, and lastly, how the measurement data is processed.

### 5.1 Measurement System

A comprehensive measurement system is installed at the Halogaland bridge to obtain response data as well as data of the environmental conditions, such as wind conditions and ambient temperature. The measurement system includes 15 accelerometers in total; 2 placed inside the bridge towers, 5 placed either on a hanger or main cable of the bridge, while the remaining are placed inside the bridge girder. As for the wind-measurements there is 10 anemometers in total, unevenly spaced along the longitudinal direction of the bridge. Amongst other measurement data available is temperature and strain data at different locations along the span of the bridge. Technical drawings of the bridge with a full overview of the sensor installations at the bridge can be found in section A.1 of the appendix.

The main purpose of this thesis is to evaluate the response of the hangers at the Hålogaland bridge, following this, only response data of the hangers are evaluated, whilst response data from the girder and towers are neglected in this study. The hangers installed with accelerometers are the 3 longest hangers, located at the south end of the bridge, and logging data to BOX2. The wind measurements used in this thesis is collected from the anemometer placed on the 7<sup>th</sup> hanger, counting from the south tower of the bridge, as indicated in figure 5.1. In the same figure, the red crosses indicate the hanger accelerometers in which measurement data is collected from, while the blue dot indicates the anemometer providing measurements of the wind.

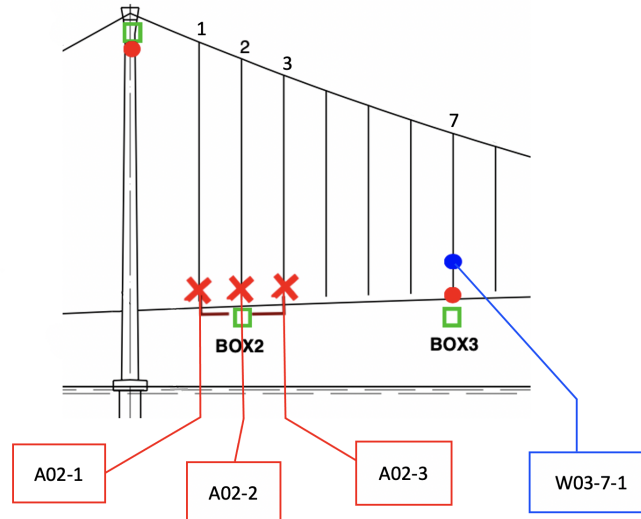


Figure 5.1: Sensor overview south end.

#### 5.1.1 Accelerometers on Hangers

Accelerometers used to measure the vibrations of the hangers are Dytran 3063B piezoelectric IEPE 3-axis accelerometers. The accelerometers are mounted to the hangers on the west-side of the bridge, about 2 meters above the bridge deck. Further positional data of the accelerometers is provided in table 5.1, where the origin of the local coordinate system is positioned at the midpoint of the bridge, and positive x- and y-directions is as indicated in figure 5.2. Acceleration measurements from the hangers include accelerations in x-, y- and z-direction. The accelerometers have an inherent sampling frequency of 200 Hz, and are accordingly able to represent signals with a frequency content up to 100 Hz.

**Table 5.1:** Accelerometer properties.

Hanger number	Accelerometer name	Position of accelerometer (x,y,z) [m]	Sampling frequency
1	A02-1	(-540.0, 7.7, 45.0)	200 Hz
2	A02-2	(-520.0, 7.7, 45.8)	200 Hz
3	A02-3	(-500.0, 7.7, 46.5)	200 Hz

### 5.1.2 Anemometers

Anemometers used for the wind measurements are Gill Windmaster Pro 3-axis anemometers, with a sampling frequency of 32 Hz. The anemometers are all placed 8 meters above the bridge deck, where they are mounted to either the hangers or to a light mast. Nine out of the ten anemometers are placed at the west side of the bridge, whilst the last anemometer is placed at the east side of the bridge. Measurement data from the anemometers include wind magnitude of the horizontal component and corresponding direction of this component, and vertical wind velocity.



**Figure 5.2:** Cardinal directions and local directions at the bridge site, map images from Kartdata ©2022.

The  $0^\circ$  axis of the anemometers is aligned with the longitudinal direction of the bridge, pointing towards the north direction. Positive y-direction is aligned with the global  $90^\circ$  axis, as indicated in figure 5.2. The measurements of the wind direction is given in terms of degrees and describe the direction the wind is travelling to. Following this, wind directions of about  $270^\circ$  correspond to winds perpendicular to the longitudinal direction of the bridge, coming in from the west. Anemometer “W03-7-1” is the anemometer located closest to the instrumented hangers studied in this thesis, consequently, wind-measurements from this anemometer is used in the estimation of the theoretical shedding frequencies for the hangers. Positional data of the anemometer is included in table 5.2. As illustrated in table 5.2 and 5.1, the anemometer is located at a distance of 80-120 meters from the hangers.

**Table 5.2:** Anemometer properties.

Hanger number	Anemometer name	Position (x,y,z) [m]	Sampling Frequency
7	W03-7-1	(-420.0, 7.6, 49.1)	32 Hz

## 5.2 Damper Installations at the Hålogaland Bridge

To start of with, dampers for both x- and y-directions were installed on the three longest hangers at the south end of the Hålogaland-bridge, corresponding to the hangers shown in figure 5.1 in section 5.1. During a winter storm in January of 2021, before measurements of the vibrations in the hangers had begun, some of the dampers were damaged leaving only 3 out of the original 6 dampers intact<sup>[10]</sup>. Hanger 1 was left with no dampers at all, hanger 2 had the damper for the y-direction still intact whilst hanger 3 had both dampers intact. The first measurement period ranges from the 25<sup>th</sup> of may to the 15<sup>th</sup> of October 2021, comprising measurement data with damper installations corresponding to what is described above.

On the 20<sup>th</sup> of December 2021 dampers were again installed, so that all three hangers at the south end of the bridge had dampers in both x- and y-directions. Measurement data of the vibrations of the hangers was re-initiated on the 1<sup>st</sup> of February 2022, and ended the 30<sup>th</sup> of April 2022. However, the response data analyzed in this thesis only covers the period from the 1<sup>st</sup> of February to 23<sup>rd</sup> of March. The above mentioned measurement period from 2022 will in this thesis be referred to as the second measurement period. All dampers, both before and after the 20<sup>th</sup> of December 2021 were installed 8 m above the bridge deck, and with the biggest mass pointing downwards as recommended by TESolution.



**Figure 5.3:** Damper and accelerometer installations on hanger 1 and 3 at the Hålogaland bridge.

## 5.3 Processing of Measurement Data

### 5.3.1 Pre-processing

Measurement data from the anemometers have accompanying status codes which, for each sample, indicate the quality of the corresponding measurement. There are in total 12 different status codes where 2 of the status codes, namely *00* and *0A*, denote samples of sufficient quality for direct usage in further research. The remaining samples with other status codes are removed from the original data, and linear interpolation is applied to preserve the original sampling rate of the signal. An error-ratio, in this case the number of samples removed from the data divided by the total length of the data, is calculated for each time series. Time series with a corresponding error-ratio exceeding 2% have been excluded from further research. Measurement data from the accelerometers have also been adjusted. Samples where the measured acceleration exceeds the value of 10 times the standard deviation of the accelerations for the entire recorded signal, is excluded and removed from the data. Likewise as for the wind-time series, original sampling rate is preserved through linear interpolation. For more details on the procedure, the python-code is available in section C.1 of the appendix. After spurious samples of the acceleration data have been removed from the signal, the mean value of the data is subtracted from the signal, leaving only the oscillating part of the signal.

### 5.3.2 Post-processing

Displacements are obtained through frequency domain integration of the acceleration data. The FFT algorithm is applied to the acceleration time series, converting the time series from the time domain to the frequency domain. In the frequency domain, the signal is integrated to obtain the displacements before the inverse FFT is applied to the signal and displacements in the time domain is obtained<sup>[29]</sup>. Mean value estimates of two different window sizes have been used throughout the post-processing of the response data. Both estimates have been calculated using a centered window. For the orange line indicating the mean values of the wind magnitude and wind direction in several plots, a moving window of 600 seconds has been applied. Standard deviations of the accelerations and displacements for different mean winds are calculated using a mean wind estimate with a moving window of 60 seconds. For the standard deviations of both the accelerations and the displacements, a resolution of 0.25 m/s have been used for the mean wind. The continuous standard deviations of the entire measurement period is calculated and downsampled based on consecutive 3-second windows, keeping only the single sample per window. The turbulence intensity of the wind magnitude has been calculated using consecutive windows of 10 minutes throughout the time series, with no overlap.

The calculation of the theoretical shedding frequencies are based on an estimation of the mean wind using a moving window of 60 seconds. As previously mentioned, a Strouhal number of 0.185 is assumed. The theoretical shedding frequencies are marked by a thin red line in the spectrograms for the x-direction vibrations. For the spectrograms of the y-direction vibrations, the theoretical inline shedding frequencies are marked by a thin red line. The consecutive FFT's calculated in the STFT for the spectrograms have a corresponding window size of 10 seconds with a 5 second overlap between each segment. A window function called *Tukey window* with a shape parameter equal to 0.25 has been applied to each section, also known as a tapered cosine window. The shape parameter represents the fraction of the window inside the cosine tapered section, and can take values in the range of 0 to 1, where the value 0 corresponds to a rectangular window and 1 corresponds to a *Hanning window*<sup>[30]</sup>. The signals have not undergone any type of band-pass filter prior to the TF representation of the signal. For more details on the procedure, the reader is referred to the python-codes available in section C.2 and C.3 of the appendix.



## 6 Presence and Magnitude of Vortex Induced Vibrations

This chapter will cover the prerequisites for vibrations in hangers without any dampers to occur, based on findings from the measurement data.

### 6.1 Direction of the Wind

Time series where the wind approaches either from the north or south cardinal direction, corresponding to directions of  $180^\circ$  or  $0^\circ$  respectively, is in general characterized by vibrations of lower magnitudes. Additionally, measurement data of the direction of the wind is often abnormal in the sense of rapid changes, jumping from minimum to maximum values for subsequent samples, as shown in figure 6.1. Mean wind velocities close to zero often result in unstable wind directions as the turbulent part of the wind almost solely contributes to the entire magnitude of the wind, giving rise to rapid and fluctuating wind directions. However, poor quality measurement data of the wind direction is also observed for time series of higher mean wind ranges, suggesting other feasible causes for the instabilities. Especially for directions of around  $180^\circ$ , the measurement data is composed of rapid changes and jumps between  $0^\circ$  and over  $300^\circ$ .

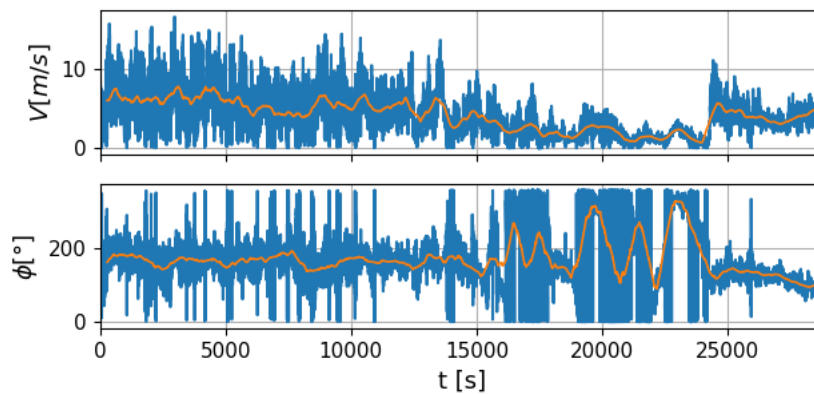


Figure 6.1: Faulty measurements for directions of  $180^\circ$ .

#### 6.1.1 Tower Shadowing

Measurement data of the wind is sampled at the anemometer mounted to hanger 7, at the south side of the hanger, as shown in section A.2 of the appendix. The given configuration gives rise to tower shadowing from the hanger in which the anemometer is mounted to, for winds coming in from the north. Correspondingly faulty measurements occur because the anemometer is located in the wake of the tower, or in this case hanger. Experimental studies performed by *S. Orlando et al* suggest the readings from the anemometers are highly affected from tower shadowing in ranges of about  $\pm 10^\circ$  offset from the direction corresponding to wind flow in the  $180^\circ$  direction. Furthermore, the magnitude of the free wind speed in front of the hanger was found to influence the percentage reduction in measured wind speed in the wake of the structure, where lower wind speeds resulted in higher reduction in the wind speed sampled by the anemometer<sup>[31]</sup>.

Tower shadowing effects in the hangers of the bridge might occur for both southerly and northerly winds, where the laminar wind flow is disrupted either by a bridge tower or hanger. The south tower of the Hålogaland bridge is located just 32,5 meters from hanger 1, with a width of about 4,4 meters in comparison to the diameter of the hangers at 86 mm. Consequentially, flow may become turbulent in addition to a reduction in wind velocity in the wake of the tower, both explaining the low vibration amplitudes for southerly winds. Similar effects may be present for northerly winds, although anemometer measurements are expected to be more severely affected than the vibration response for the given direction, as the hangers are located further away from each other than the anemometer and the corresponding hanger it is mounted to.

## 6.1.2 Wind Directions Causing Vortex Induced Vibrations

In most cases, the cross-flow and inline vibration response will be composed of both x- and y-direction vibrations, as the wind rarely approaches directly perpendicular to or along the longitudinal direction of the bridge. Followingly, spectrograms will often show two distinct lines of vibration response corresponding to the cross-flow and inline vibration response, as in the y-direction spectrogram in figure 6.4b. The line with the lowest frequency content aligns with the theoretical shedding frequency and hereby the cross-flow vibration response, denoted by a red line in the x-direction spectrogram. The line with the highest frequency content aligns with the inline vibration frequency, at twice the shedding frequency, denoted by a red line in the y-direction spectrogram.

Westerly or easterly winds are found to induce the largest vibrations in the hangers. The indicated directions would typically cause cross-flow vibration response in the x-direction, and correspondingly large amplitude vibrations. Vibrations in the y-direction would mainly be caused by inline shedding forces, causing vibration response of relatively smaller amplitudes compared to the vibrations in the x-direction. Correspondingly, northerly or southerly winds should in theory cause cross-flow vibration response in the y-direction, resulting in larger vibration amplitudes for the y-direction compared to the x-direction. However, measurement data indicate otherwise. Cross-flow and inline vibration response in the y-direction is found to induce vibrations of equivalent magnitudes. Furthermore, in many cases, vibration amplitudes in the y-direction is larger for the inline vibration response compared to the cross-flow vibration response. In all, vibration amplitudes in the y-direction, caused either by inline or cross-flow vibration response, is negligible compared to the cross-flow vibration response in the x-direction. The same goes for the inline vibration response in the x-direction.

The previously mentioned tower shadowing might explain the differences in response amplitudes. Possible different directional properties of the hangers might also influence the differences in the response amplitudes. Here, the connections of the hangers to the bridge girder and main cables, shown in section A.3 of the appendix, are relevant to consider. *Olsen et al* performed tests on the hangers at the Hardanger bridge, comparing the lengths, estimated from the measured frequencies and theoretical relations, to those given in the technical drawings of the bridge. Findings include the estimated length of the same hanger differ depending on the direction in which the vibration frequencies are measured, suggesting the stiffness of the pin joint is not equal in all directions<sup>[32]</sup>. Nevertheless, amplitudes of the vibration response in the y-direction is negligible compared to what is observed for the x-direction. Hence, taking into account the coupled response will not influence the maximum total accelerations in any significant manner, where numerical values of x- and y-direction vibration amplitudes will be discussed further in section 7.2. Following this, cross-flow vibration response in the x-direction will be attributed the most attention in further investigations of the vibration response in the hangers.

## 6.2 Turbulent Conditions

The amplitudes of the VIV in the hangers are also greatly influenced by the stability, or lack of stability, in the wind flow. Both the magnitude of the turbulent part of the wind flow, as well as the stability in the direction of the wind, seem to affect the presence and magnitude of VIV.

### 6.2.1 Magnitude of the Turbulence

An increase in turbulence will often result in a reduction in the strength of vortex shedding, also resulting in a significant reduction in vibration amplitudes<sup>[20]</sup>. Equivalent response characteristics are observed for the hangers at the Hålogaland Bridge; figure 6.2 demonstrate wind measurements and corresponding acceleration measurements of hanger 1, for two different time series, both from the 16<sup>th</sup> of July 2021. The measurement data reveal time series of relatively identical mean wind ranges and directions of the wind. However, the magnitude of the response between the two time series of the same hanger differ by quite a lot.

Turbulence intensities, as shown in figure 6.3, are in general higher for the measurement starting at midnight. The increased turbulence intensity at around 6000-8000 seconds for the time series starting at 08:00 may be attributed to the temporary reduced mean wind, resulting in relatively larger standard deviations. Furthermore, the time series starting at 00:00 has larger fluctuations in the direction of the wind, amplifying the effect of the already unstable wind conditions resulting in low response amplitudes.

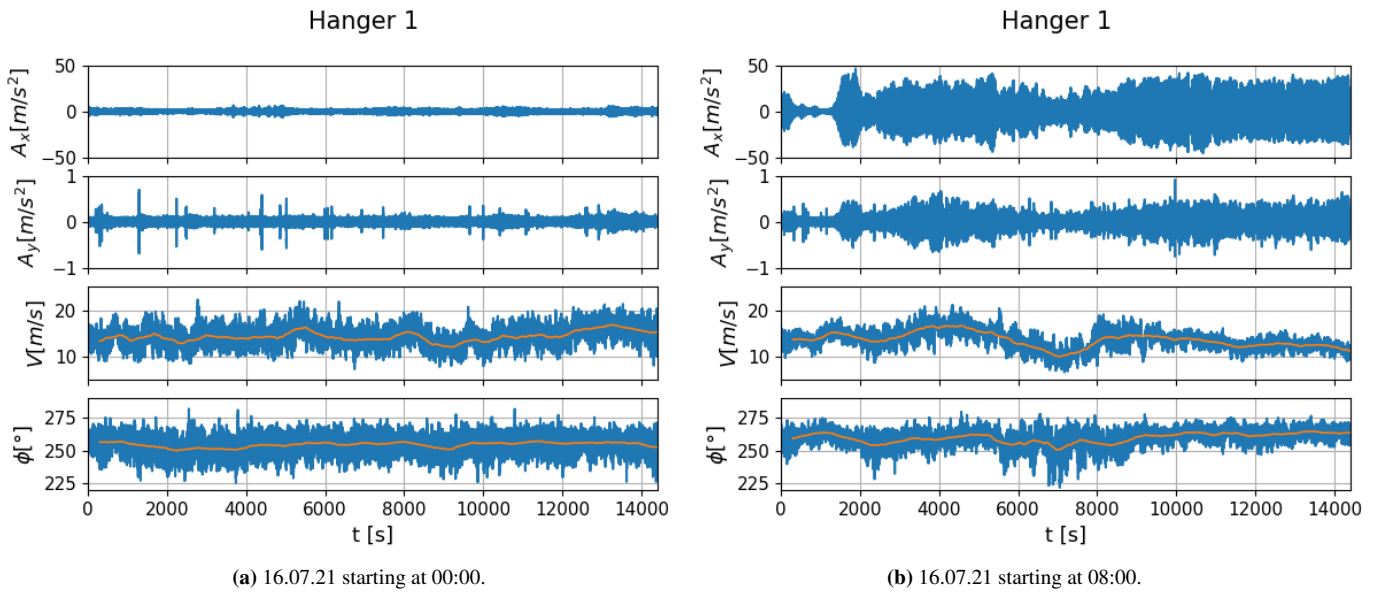


**Figure 6.2:** Vibration response and corresponding wind measurements.

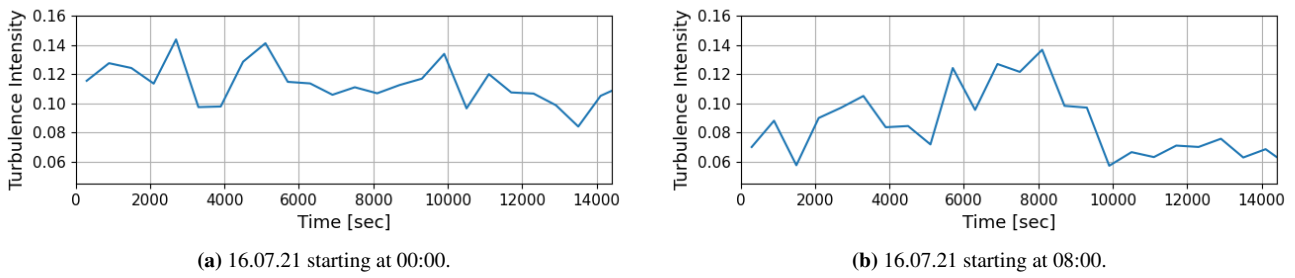


**Figure 6.3:** Turbulence intensity.

Corresponding to the previous descriptions of the differences in response characteristics between the two measurements, figure 6.4 further illustrates these differences. The time series starting at 00:00, given in figure 6.4a, show no results of any detected vibration frequency at all. In contrast, the time series starting at 08:00 show vibration response in good agreement with the theoretical shedding frequency, indicating VIV is present.

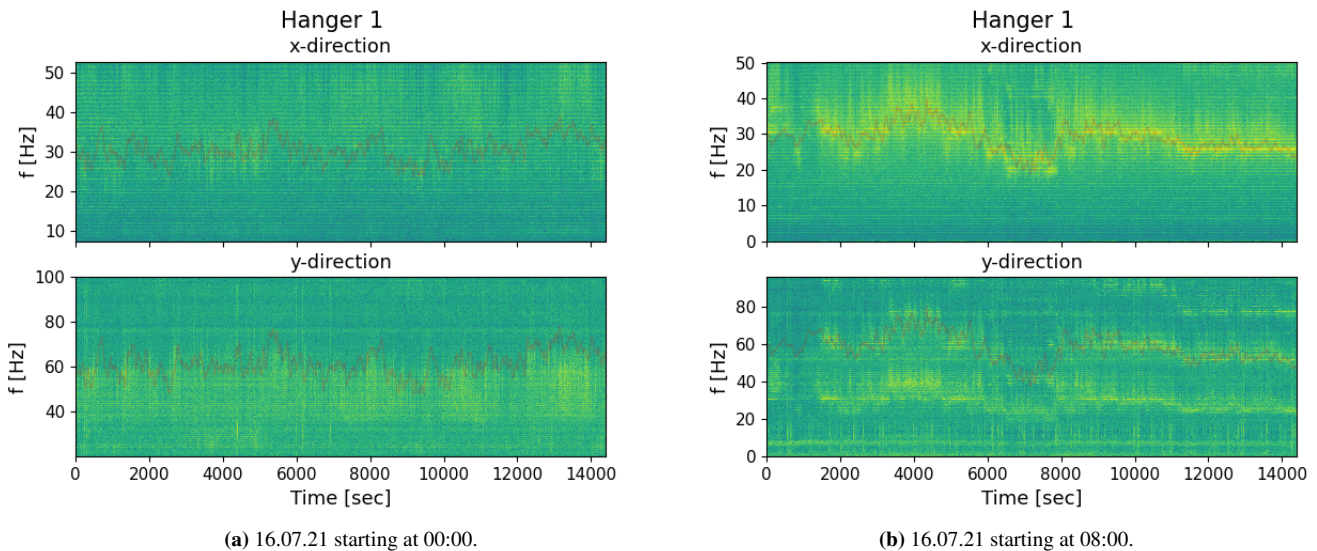


**Figure 6.4:** Spectrograms of vibration response in hanger 1.

### 6.2.2 Stability in Wind Direction

Looking at the time series given in figure 6.2b, the magnitude of the turbulence is relatively constant throughout the time series up until 10 000 seconds, where it is slightly reduced. Nevertheless, response amplitudes are temporarily reduced between 6000-8000 seconds into the time series, corresponding to the temporary increase in the instabilities of the wind direction. A temporary reduction in the mean wind is also observed, however, response amplitudes of hanger 1 is in fact found to reach its maximum levels of response for mean wind of this range, further discussed in section 7.2. Consequently, the temporary reduction in response amplitudes have to be caused by the increase in the instabilities in the direction of the wind. In all, results indicate that the amplitude of the vibrations are determined both by the magnitude of the turbulence and the stability in the direction of the wind, and that high levels of both limit the presence of the vibrations quite significantly.

### 6.3 Mean Wind Range

Wind conditions characterized by relatively low turbulence and stable westerly or easterly wind directions, are likely to induce VIV in the hangers. For the given conditions, vibrations corresponding to the theoretical shedding frequency is easily detectable for wind magnitudes in the range of about 3-20 m/s, although the bandwidth of the vibration signal varies with the different wind magnitudes. As shown in figure 6.5 and 6.6, high wind magnitudes seem to induce a broad-banded vibration response while the lower wind magnitudes seem to induce a more narrow-banded response. The differences in the bandwidth of the signal might be correlated to the wind velocity, however, the differences might also be caused by the varying magnitude of the turbulence, which will be discussed further in section 7.3.

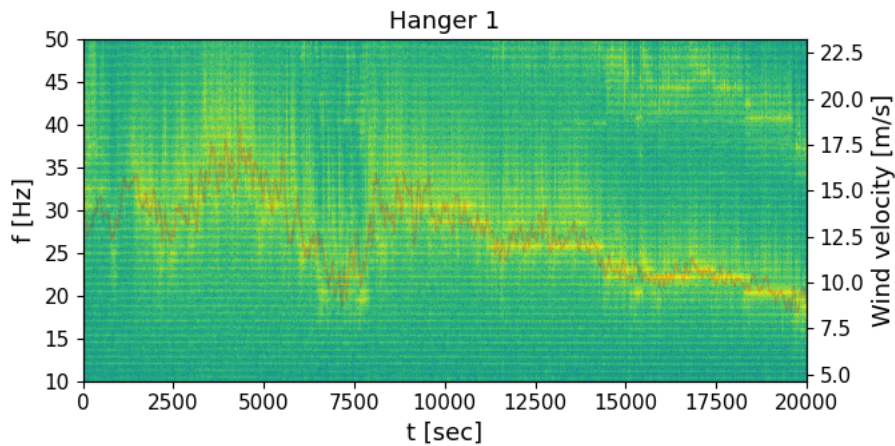


Figure 6.5: VIV in x-direction for mean wind range 10-18 m/s.

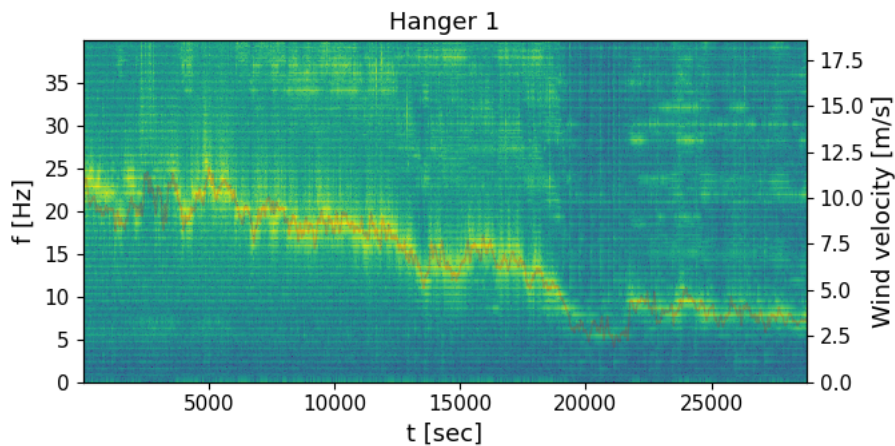


Figure 6.6: VIV in x-direction for mean wind range 2.5-10 m/s.

The close alignment of the actual vibration frequencies to the theoretical shedding frequencies validates the presence of VIV in the hangers. Well known characteristics of the behaviour corresponding to VIV is also observed for the hangers. In figure 6.5 lock-in behaviour is clearly noticeable at around 12000-14000 seconds into the time series, where vibration frequencies are focused around a single frequency component, even though the mean wind has minor fluctuations as seen by the fluctuations in the theoretical shedding frequency.

Conclusively, the cardinal direction of the wind flow along with the magnitude of the turbulence and stability in direction appears to determine the presence of VIV in the hangers. The wind magnitude determines the shedding frequency and hereby also the vibration frequencies of the hangers, where measurement data stipulate VIV for any wind magnitude in the range 3-20 m/s. Although, important to notice, the mode shape of the given activated mode might influence whether the sensor is positioned closer to a node or anti-node, in turn influencing the magnitude of the measured response.

## 7 Effect of Dampers

### 7.1 Vibration Response Characteristics

This chapter will cover time series of wind conditions known to induce VIV, in order to compare vibration response between the hangers to be able to assess the ability of the damper to dissipate energy from the hanger vibrations. For the given time series, the response of the hangers in terms of acceleration and displacement amplitudes and corresponding vibration frequencies are characterized. Furthermore, the response of the hangers are investigated for a wide range of wind velocities to characterize the effect of the damper with respect to different vibration frequencies.

#### 7.1.1 Dampers on Selected Hangers

Figures presented below comprise measurement data from a time series starting at 8 am the 16<sup>th</sup> of July 2021. Consequently, hanger 1 had no dampers installed, hanger 2 had only one damper, whereas hanger 3 had both dampers intact.

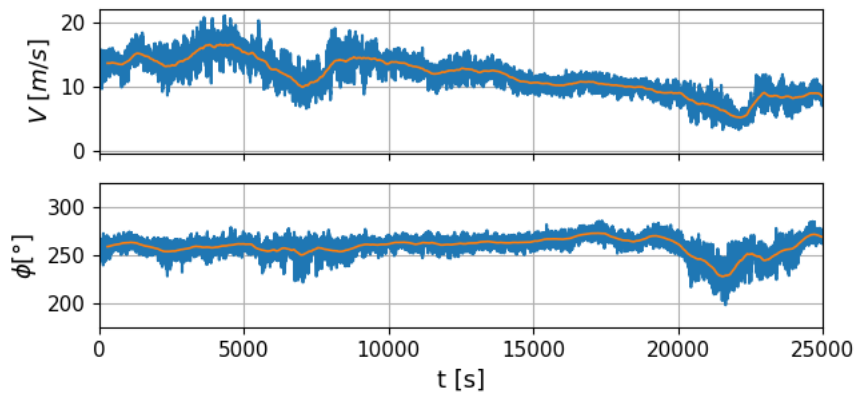


**Figure 7.1:** Wind measurements from time series started at 08:00 the 16<sup>th</sup> of July 2021

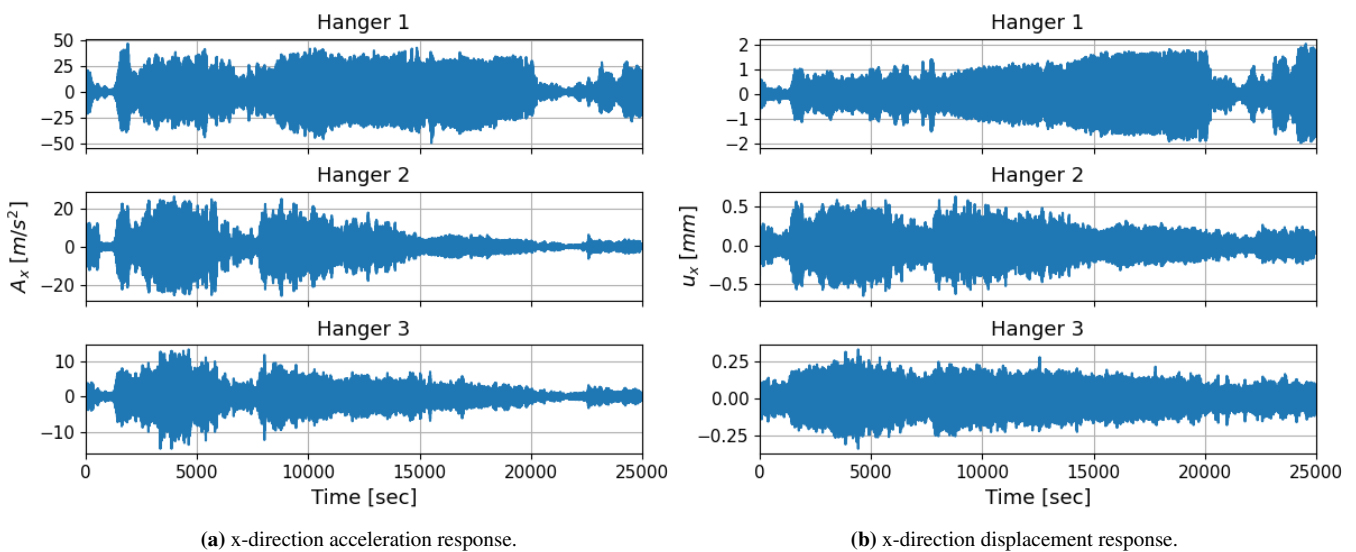
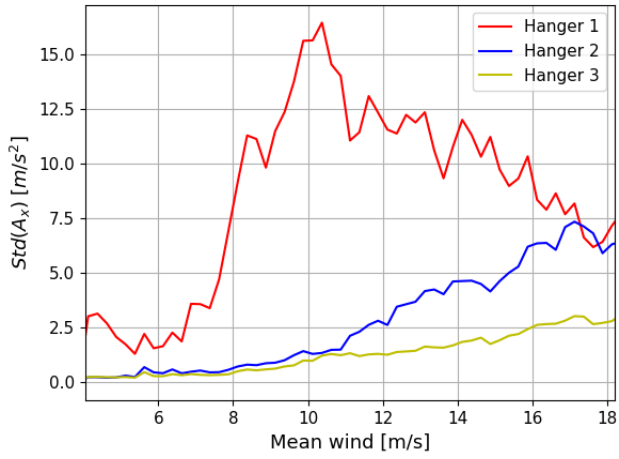
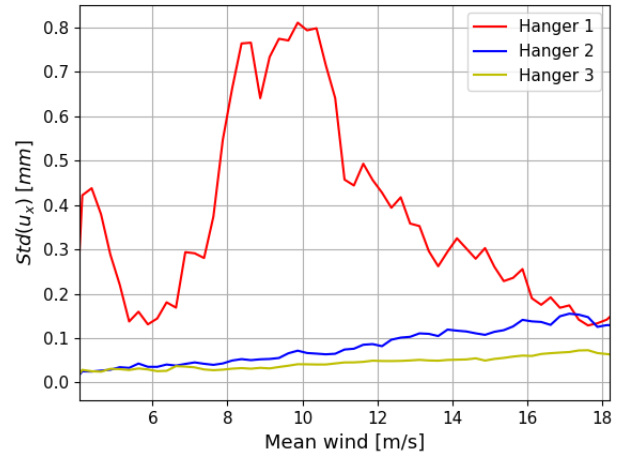


**Figure 7.2:** Response time series, 16<sup>th</sup> of July 2021.





(a) Standard deviation of x-direction accelerations for different wind magnitudes.



(b) Standard deviation of x-direction displacements for different wind magnitudes.

**Figure 7.3:** Standard deviations of response, 16<sup>th</sup> of July 2021.

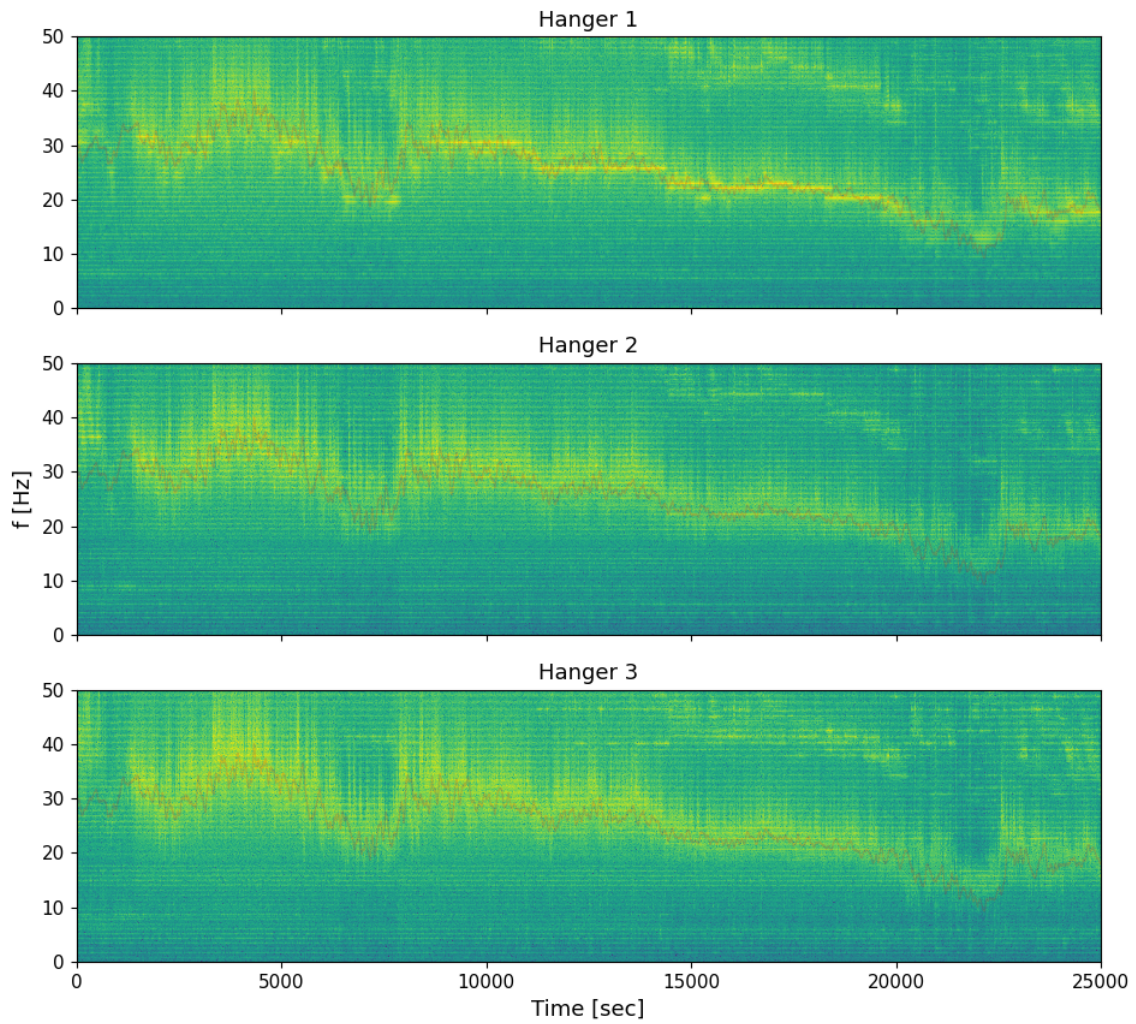


**Figure 7.4:** Spectrograms of vibrations in x-direction, 16<sup>th</sup> of July 2021.

Wind measurements, as presented in figure 7.1, may for the first 20 000 seconds be characterized by relatively stable winds coming in from the west/north-west direction, with low levels of turbulence. Noticeable again is the effect of unstable wind directions, where large acceleration amplitudes in hanger 1 is suddenly cut off at around 20 000 seconds into the time series, as shown in figure 7.2a. Corresponding wind measurements show a sudden change in wind direction accompanied by fluctuations in the direction of the wind of larger magnitude. Throughout the stable part of the time series, the first 20 000 seconds, hanger 1 has relatively constant amplitudes of acceleration, while acceleration amplitudes of hanger 2 and 3 decreases as the wind magnitude decreases from levels of 18 m/s to levels of 10 m/s. For the same time period, figure 7.2b illustrate displacements in hanger 1 increases monotonically as the wind magnitude decreases to levels of 10 m/s. In contrast, displacements in hanger 2 and 3 decreases monotonically as the wind magnitude decreases. Calculations of the standard deviations of the accelerations and displacements for different mean winds, as shown in figure 7.3, validate the observations from the time series. The response in hanger 2 and 3, installed with 1 and 2 damper(s) respectively, are closely correlated to the wind magnitude, where increasing wind magnitudes result in larger acceleration and displacement response in the hangers. Contrary to this, hanger 1 attains maximum response for wind magnitudes of around 10 m/s, and displays a decreasing trend for further increasing wind magnitudes.

The vibration frequencies of the hangers vary along with the changing magnitude of the wind, and are in line with the estimated theoretical shedding frequencies denoted by the red lines in figure 7.4. As previously mentioned, none of the signals presented in this thesis have undergone any filtering to remove unwanted frequency content, emphasizing the remarkable correlation of the measured vibration response to the theoretical shedding frequency. The first part of the time series, where mean winds are up to 18 m/s, vibration response for all three hangers appear to be composed of a wider range of frequencies. As the wind magnitude decreases and theoretical shedding frequencies drop down to levels of about 20 Hz, so does the actual vibration frequencies. The response of hanger 1 becomes more narrow banded, with amplitudes of vibration more closely focused around the theoretical shedding frequency. However, where the theoretical shedding frequency follows the development of the wind magnitude with corresponding fluctuations, the measured vibration frequency remains constant for longer time periods, matching the description of lock-in behaviour. Equivalent response characteristics are not apparent in hanger 2 and 3, both installed with dampers. For hanger 2 and 3, the magnitude of the response seems to decrease as the magnitude of the wind decreases, as seen by the brightness of the colour in the spectrograms decreasing. Also, in contrast to the response of hanger 1, the signal seems to maintain more of its bandwidth.

Equivalent hanger response characteristics as to what is described above is observed for a numerous amount of time series. Following is a time series from the 19<sup>th</sup> of July 2021, starting at 8 am. Presented in figure 7.5 is the wind measurements of the time series, which reveals two distinct and separate sections of relatively stable and equal wind directions. The first section at 0-5000 seconds with a corresponding mean wind of about 10 m/s, and the latter section starting at 15 000 seconds with a corresponding mean wind of about 13-15 m/s. The remaining part of the time series include winds of lower magnitude and greater instabilities in the wind direction.

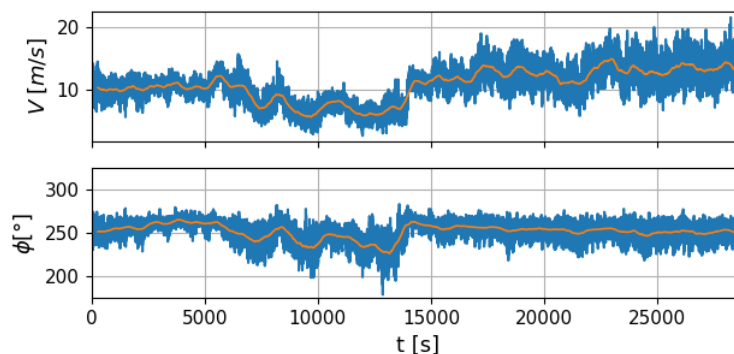


**Figure 7.5:** Wind measurements from time series started at 08:00 the 19<sup>th</sup> of July 2021



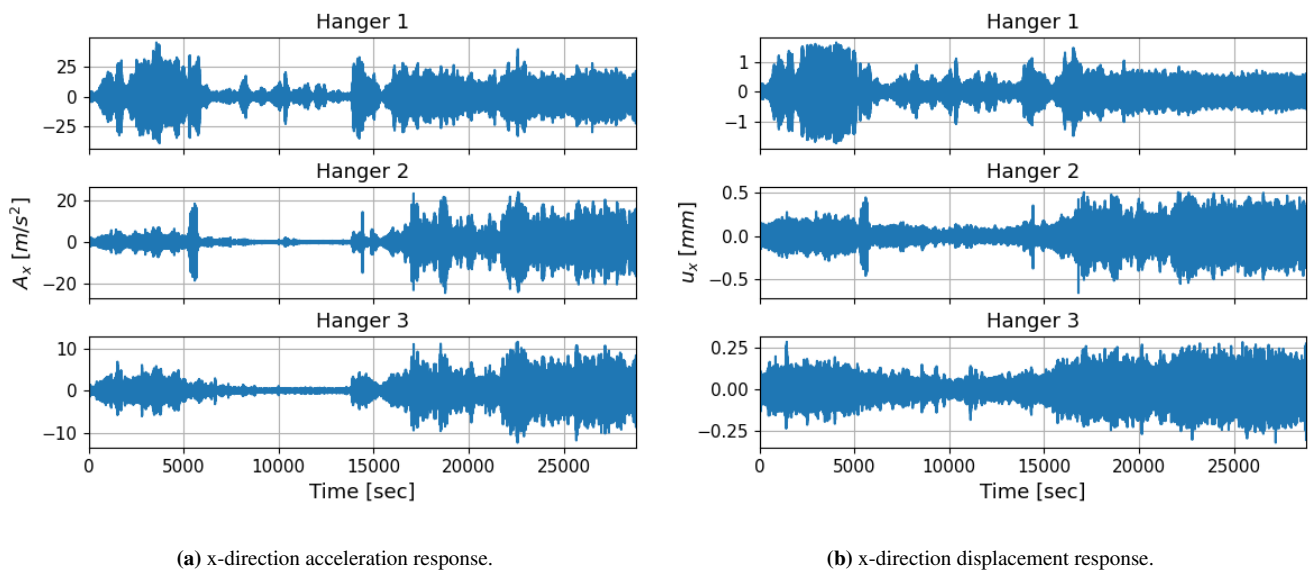


**Figure 7.6:** Response time series, 19<sup>th</sup> of July 2021.

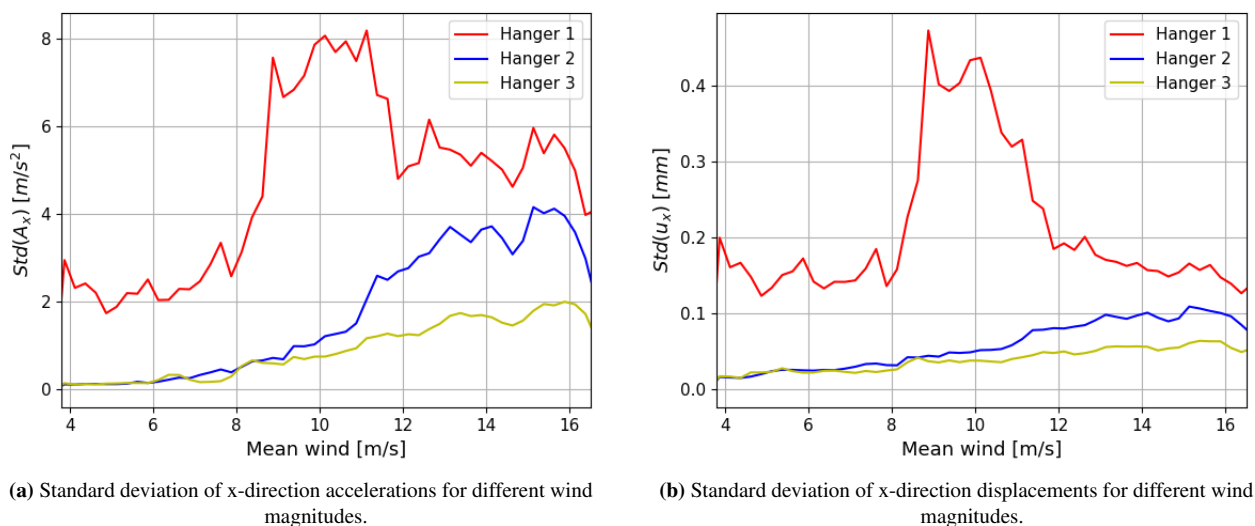


**Figure 7.7:** Standard deviations of response, 19<sup>th</sup> of July 2021.

Looking at the first section in figure 7.6a, acceleration amplitudes of hanger 2 and 3 are in the same range while the amplitudes of hanger 1 is significantly higher, at values exceeding  $25 \text{ m/s}^2$ . For the second section comprised of larger mean winds, the acceleration amplitudes of hanger 1 is slightly reduced, whereas amplitudes of hanger 2 and 3 have increased to levels of where amplitudes of hanger 2 are in the same range to those of hanger 1. For the displacement response as shown in 7.6b, hanger 2 and 3 demonstrate similar development as for the acceleration response, with increasing displacements for increasing mean winds. Equivalent to the observations based on the time series from the 16<sup>th</sup> of July, the response in hanger 1 is of larger magnitude for mean winds of about 10 m/s compared to higher levels of mean wind. This applies to both accelerations and displacements of hanger 1. Again, calculations of the standard deviation of the acceleration and displacements for different wind magnitudes, as in figure 7.7, substantiate the observations from the time series where maximum response of hanger 1 is reached for wind magnitudes of about 10-11 m/s.

For the middle section of the time series, the window between 6000 and 14000 seconds, the response amplitudes are negligible compared to the rest of the time series. Again, the lack of presence of VIV is coinciding with unstable wind conditions, while this time, it is definitely not caused by increased turbulence levels, as these levels are in fact greater for the second half of the time series. In this case, the low response amplitudes appear to be caused by the instability in the direction of the wind alone.

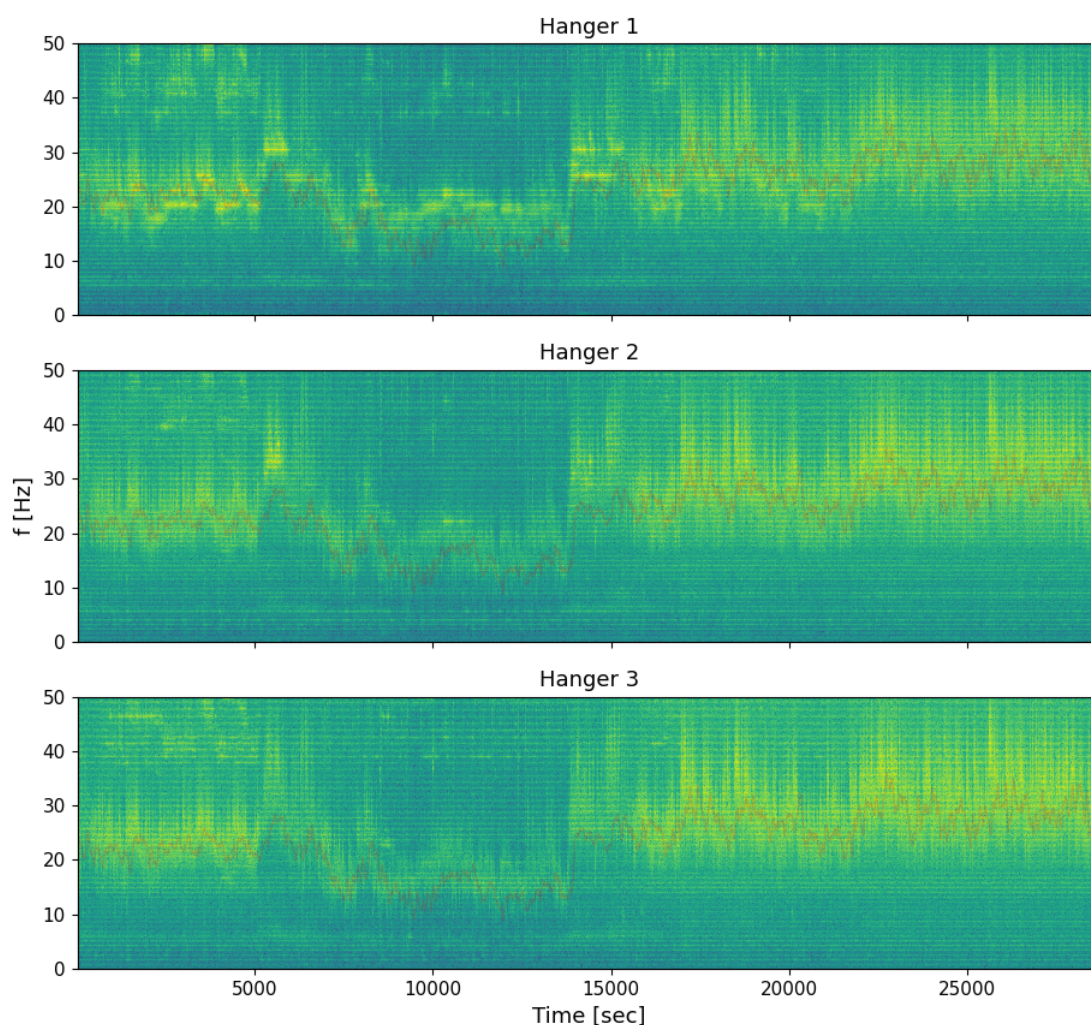


**Figure 7.8:** Spectrograms of vibrations in x-direction, 19<sup>th</sup> of July 2021.

The frequency content of the vibration response in the hangers, as shown in figure 7.8, again confirms the observations regarding the bandwidth of the response for different frequencies. The vibration response of hanger 1, without any damper, tends to be narrow banded for moderate wind levels corresponding to shedding frequencies up to 25 Hz. Higher wind magnitudes tend to induce a more broad-banded response in the hanger, noticeable in the second section of the spectrogram for hanger 1, starting at 15 000 seconds. In contrast to the narrow banded response of hanger 1, hanger 2 and 3 has a scattered and broad-banded response for all frequencies. Regardless of the narrow- or broad-banded response, the theoretical shedding frequency is still very much aligned with the vibration response of all hangers.

### 7.1.2 Dampers on all Hangers

The measurement period of 2021 was ended in October, and when measurements again was initiated in February of 2022, dampers were installed on all three hangers, both in x- and y-directions. Unfortunately, acceleration measurements from hanger 3 seems to be faulty as only positive accelerations are registered. Consequently, exclusively response data from hanger 1 and 2 has been used in further analysis.

Wind measurements, as given in figure 7.9, indicate west/north-westerly wind directions, equal to the previously introduced time series from the measurement period in 2021. The wind direction of the time series is relatively stable, whereas turbulence levels are quite high. Measurement data also demonstrate clear gusts in the wind velocity at around 5000 and 15000 seconds into the time series. The response for the given time series is identical both in terms of accelerations and displacements for hanger 1 and 2, as demonstrated in figure 7.10. In contrast to previously analyzed time series, the time series starting at 16:00 the 27<sup>th</sup> of February 2022 has mean winds of higher magnitudes, compared to the time series from 2021. Presented in section 7.1.1, hangers with either one or two dampers showed an increasing trend in the magnitude of the response for increasing mean winds. The aim of analyzing time series of even larger wind magnitudes is to verify whether this trend still holds true.

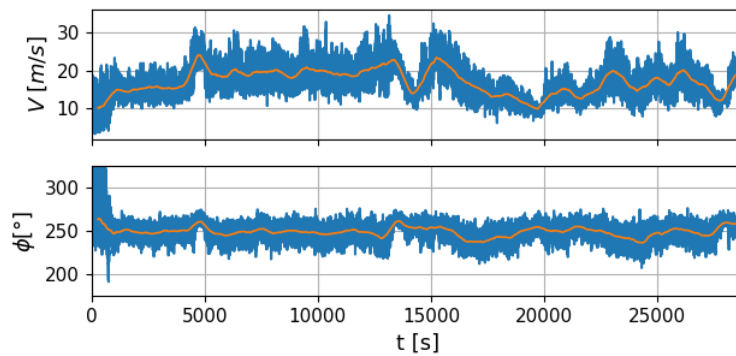
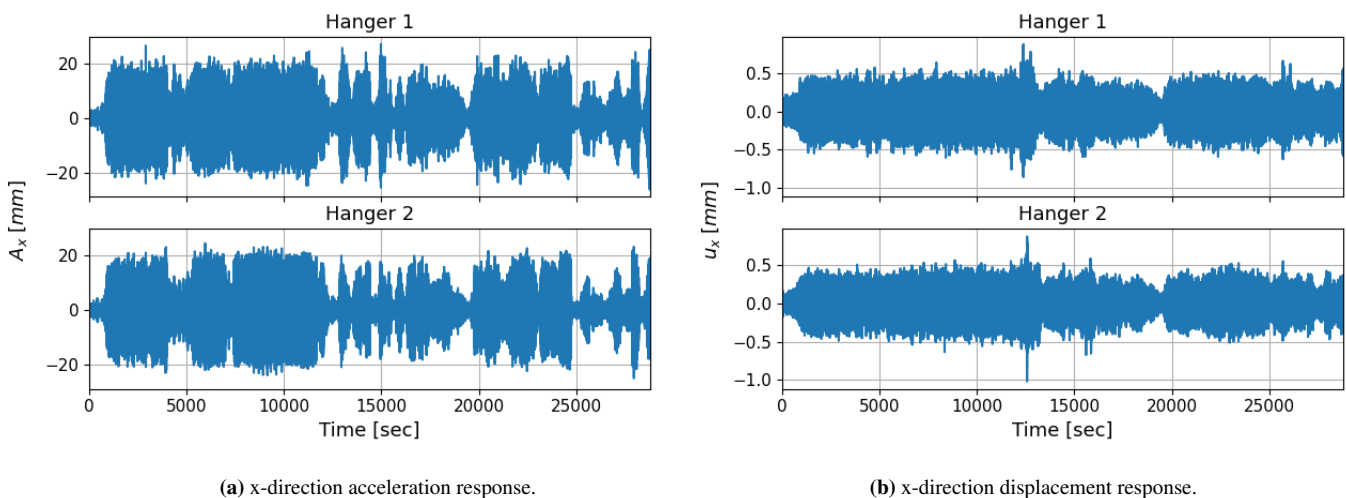


Figure 7.9: Wind measurements from time series started at 16:00 the 27<sup>th</sup> of February 2022

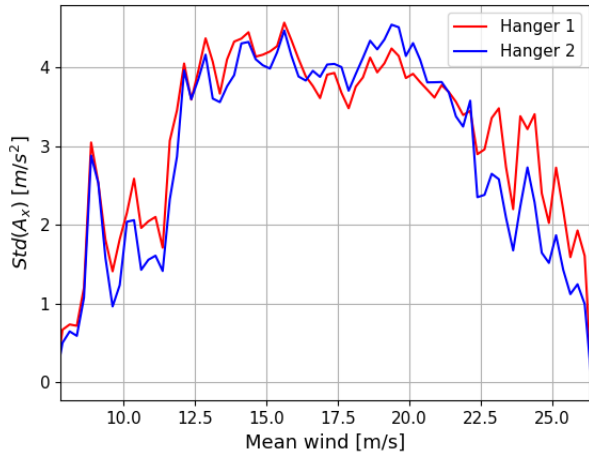


(a) x-direction acceleration response.

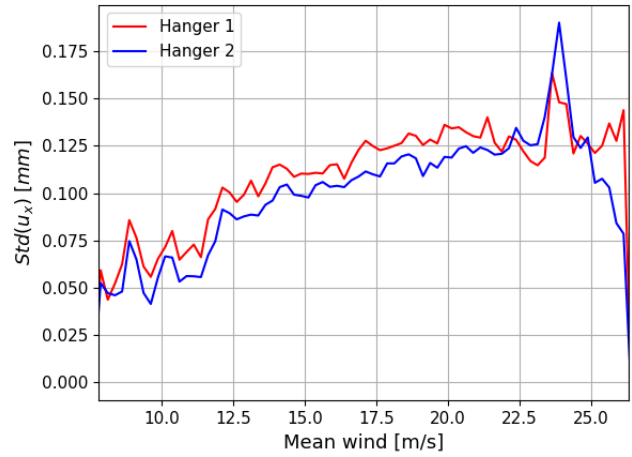
(b) x-direction displacement response.

Figure 7.10: Response time series, 27<sup>th</sup> of February 2022.





(a) Standard deviation of x-direction accelerations for different wind magnitudes.



(b) Standard deviation of x-direction displacements for different wind magnitudes.

**Figure 7.11:** Standard deviations of response, 27<sup>th</sup> of February 2022.

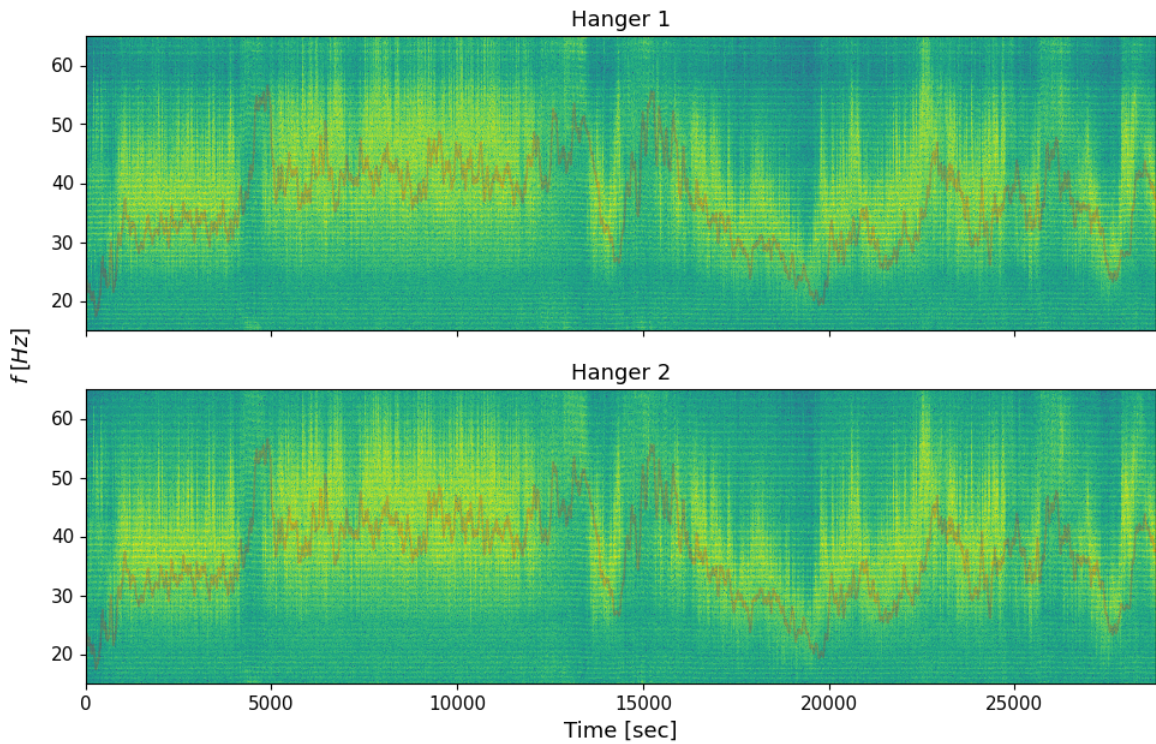


**Figure 7.12:** Spectrograms of vibrations in x-direction, 27<sup>th</sup> of February 2022.

The standard deviations of the response for different wind magnitudes are presented in figure 7.11. Although the magnitude of the standard deviations is lower compared to maximum levels of the previously introduced time series, this is solely due to the fact that all hangers now have dampers installed. The magnitude is in good correspondence with previous response levels of the hangers with one or two dampers installed. However, the trend in the amplitudes of the standard deviations stipulate different response characteristics compared to what is observed in previous time series. The standard deviations of the accelerations show a decreasing trend for mean winds above 20 m/s, whereas previous data have indicated a monotonic increase in acceleration amplitudes. This suggests the monotonic increase in response amplitudes might be limited to mean winds up to 20 m/s. In contrast, the displacement response has similar characteristics to the previously observed measurement data, with a monotonic increasing trend for increasing mean winds.

Looking at the wind measurements and frequency content of the response, in figure 7.9 and 7.12 respectively, the mean wind only reaches levels of over 20 m/s for very short periods of time. Approximately 5000 seconds into the time series the mean wind increases to levels exceeding 20 m/s from levels of 15 m/s, which corresponds to a sudden increase in the theoretical shedding frequency from about 35 Hz to 55 Hz. An equivalent increase in shedding frequency and wind magnitude is observed around the 15 000 second-mark, where in both cases vibration frequencies in the hanger are non-detectable, suggesting the time period of these high levels of mean wind is too short to induce VIV in the hangers. Consequently, the estimation of the standard deviations for the accelerations might be misleading in the sense that the wind magnitude only reaches these high levels in temporary wind gusts. On the other hand, stable wind conditions of wind velocities in this range rarely occur, only in the more unlikely event of a storm. Due to the limited amount of data under these conditions, response characteristics for higher mean winds remain uncertain.

## 7.2 Operating Range of the Stockbridge Damper

Throughout the measurement period at the Hålogaland bridge, the maximum amplitudes of acceleration observed for hanger 1 is about  $50 \text{ m/s}^2$ , occurring for mean winds of about 10-12 m/s before dampers were installed. After damper installations, maximum amplitudes are reduced to levels of around  $25 \text{ m/s}^2$  for mean winds around 20 m/s. Displacements in hanger 1 are also drastically reduced after dampers were installed, as shown in figure 7.13, here presented by standard deviations of the displacement by the use of consecutive 3-second windows. Once again, notice the absolute maximum standard deviation of the displacements occurring in the end of May 2021, with corresponding moderate levels of wind velocities around 10-12 m/s.

Acceleration measurements of hanger 1 before and after damper installation provides a good estimate of the effect of the SD's installed at the Hålogaland bridge. Results indicate that the dampers are able to successfully dissipate energy for wind velocities of a wide range. Especially noteworthy is the elimination of the peak in responses for wind magnitudes around 10-12 m/s, corresponding to shedding frequencies in the range 21-25 Hz, provided a Strouhal number of 0.185 is used. For increasing wind velocities above 12 m/s, the magnitude of the accelerations for the hanger without any damper is naturally reduced, while the magnitude of accelerations increases for the hangers with one or two dampers installed. This suggests the energy dissipation through the damper decreases as wind velocities increase above levels of 12 m/s. Based on these observations, the SD's mounted to the hangers at the Hålogaland bridge seems to be tuned to dissipate energy for vibrations of frequencies lower than 25 Hz, corresponding to wind velocities below 12 m/s.

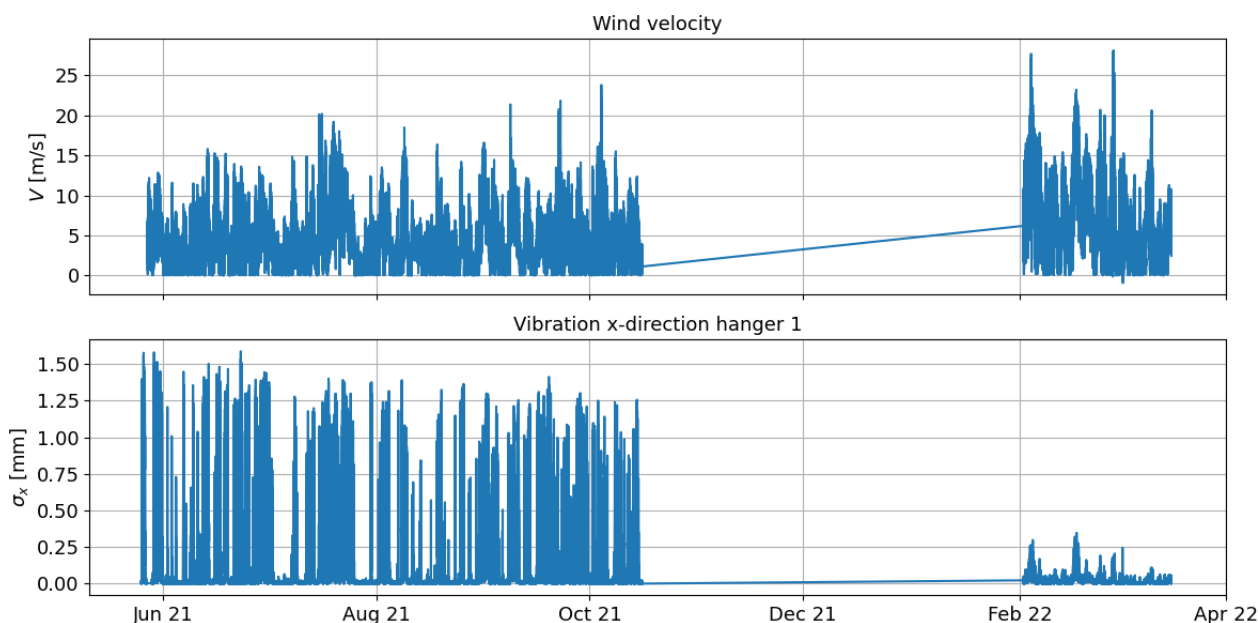


**Figure 7.13:** Wind velocities and corresponding standard deviations of vibrations in x-direction for hanger 1.

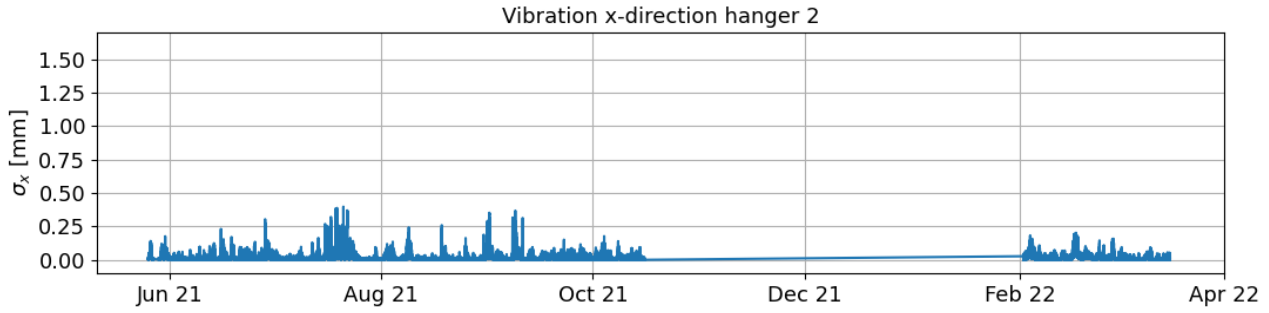


Figure 7.14: Standard deviations of vibrations in x-direction for hanger 2.

### 7.2.1 Effect of Multiple Dampers

In 2021 hanger 2 had only one damper, mounted to the west side of the hanger, designed to dissipate energy from the vibrations in the y-direction. However, results from measurement data suggest the damper is highly effective also for vibrations in the x-direction. Where hanger 1 reaches acceleration amplitudes of  $50 \text{ m/s}^2$ , hanger 2 only reaches amplitudes of  $25 \text{ m/s}^2$ . Similar characteristics is seen for the displacement response in 2021, where amplitudes of hanger 2 is significantly lower than the ones found for hanger 1. After dampers in x- and y-directions are installed on both hangers, the amplitudes of the standard deviations of the displacements for hanger 1 and 2 are approximately in the same range, as shown in figure 7.13 and 7.14. Consequently, results indicate that one single damper will significantly reduce the amplitudes of vibration in the hangers, especially for moderate wind velocities of 10-12 m/s. For higher wind velocities, the slope of the standard deviations of the acceleration amplitudes is greater for the hanger with one damper compared to the one with two dampers, as shown in figure 7.3 and 7.7. Accordingly, the effect of two dampers instead of one increases as the wind velocities increases. The increased damping effects of two dampers in contrast to one is also validated through the measurement data of hanger 3, where maximum observed acceleration amplitudes is in the range of  $10 \text{ m/s}^2$ , significantly lower than the ones found for hanger 2 with only one damper.

### 7.2.2 Damper Effectiveness for Small Response Amplitudes

Vibrations in y-direction have not been attributed any attention so far due to the low vibration response amplitudes. However, response characteristics of y-direction vibrations is useful in the analysis of damper effectiveness for vibrations of high frequencies and small acceleration amplitudes, consistent with inline vibration response.

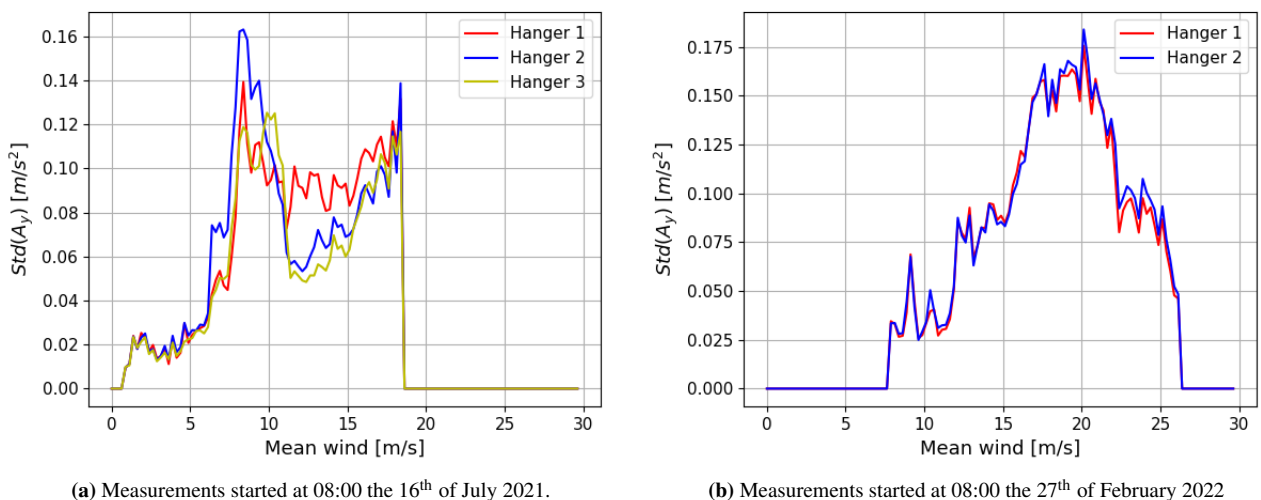


Figure 7.15: Standard deviations of accelerations in y-direction.

Figure 7.15a and 7.15b show the calculated standard deviations of the y-direction accelerations for the first time series given in section 7.1.1 and the time series in section 7.1.2, respectively. Comparing the standard deviations of y-direction vibrations in figure 7.15a and corresponding standard deviations for the x-direction, provided in figure 7.3a, the substantial difference in the magnitude of vibrations is apparent. Nevertheless, for the y-direction responses, all three hangers regardless of the damper installation have relatively similar responses.

Equivalent characteristics of larger standard deviations for the x-direction vibrations compared to the y-direction vibrations are also observed for the time series from February 2022, with a full damper installation, given in figure 7.15b and 7.11a. The differences in amplitudes between the x- and y-direction accelerations are significantly lower for this time series, compared to the 2021 measurements without a full damper installation. This is solely caused by the reduced amplitudes of the x-direction accelerations due to damper installations, as the y-direction amplitudes are in fact higher for the time series where the hangers have a full damper installation. The largest response amplitudes for the time series in 2022 occur for wind velocities larger than the existing range in the 2021-measurement. Nevertheless, vibration response in the y-direction is characterized by low response amplitudes for all wind velocities. The magnitude of the response is also independent of the number of dampers installed, suggesting the response amplitudes are too low for the damper to be activated. As previously discussed, the damper in the y-direction dissipates more energy from the x-direction vibrations than it does from the y-direction vibrations. This further substantiates the previous statement of too low excitation amplitudes for the damper to be activated, as vibrations in the x-direction are of greater magnitude than the inline vibrations in the y-direction.

### 7.3 Causes of Error in Response Analysis

Observations based on the measurement data demonstrate the vast amount of variables influencing the response of the hangers, where direction and magnitude of the wind, stability in the direction of the wind and amount of turbulence is some of the most important factors. Moreover, as the characterization of the vibration response for different mean winds are solely based on measurement data from the bridge site, several unwanted variables are introduced into the analysis of the response. Due to the nature of its location, the bridge is subjected to temperature changes, passing traffic on the bridge deck and strong wind gusts, which may all affect the measurement data increasing the uncertainty with respect to the accuracy of the results.

#### 7.3.1 Turbulence Levels

A large contributor to the uncertainty in the analyzes is the magnitude of the turbulence in the freestream wind flow, where increased levels of turbulence is found to broaden the force spectrum of the cross-flow shedding forces<sup>[20]</sup>. The vibration response of hanger 1, before dampers were installed, is characterized by a narrow-banded response for moderate wind velocities while the response is more wide-banded for higher wind velocities. However, for all the time series analyzed, the magnitude of the turbulence is also slightly higher for higher wind velocities compared to the lower wind velocities, which might also cause an increase in the bandwidth of the response. Consequently, the exact cause of the broad banded response for higher vibration frequencies, and whether it is an inherent response characteristic for higher vibration frequencies or an effect of the increased levels of turbulence, remain uncertain.

#### 7.3.2 Temperature Effects

*Cantero et al* found differences in the natural frequencies of the hangers at the Hardanger bridge for two separate measurements performed withing a few hours apart from each other. A slight increase in ambient temperature in the time between the two measurements was found to be the cause of the deviations<sup>[24]</sup>. Natural frequencies and corresponding mode shapes are of great importance in the response of the hangers related to VIV. The frequency of the shedding force is determined by the mean wind and cross sectional shape of the body subjected to the wind flow. The shedding frequency is however not affected by a change in the natural frequencies of the hangers. Consequently, the change in natural frequencies will only affect which mode is activated for the given mean wind. A relocation of each individual mode shape with respect to the mean wind might cause the response to decrease for some wind velocities, whilst there is an increase in the response for other wind velocities. Moreover, this might also affect the damper-location and whether the damper is placed closer to a node or anti-node, influencing the effectiveness of the damper. Given the location of the bridge, it is likely to be

subjected to temperatures in the range of  $-10^{\circ}$  to  $+20^{\circ}$  each year, with occasional days of temperatures exceeding these values. Based on the substantial temperature range in the operating conditions of the bridge, a difference in response throughout the seasons of a year is possible.

### 7.3.3 Basis of Comparison

Challenges arise when the differences in response within each consecutive hanger is to be compared. For the measurement data available, challenges finding equivalent time series with respect to turbulence intensity, wind velocity and direction, in addition to relatively equal stability of the wind-direction, have proven to be difficult. Additionally, the wind measurements are conducted at hanger number 7, located 80-120 meters from the hangers investigated in this thesis. Undoubtedly, the lack of a controlled environment will increase the uncertainty regarding the actual damper performance, and whether measurement data observations are caused by differences in the wind-field or by the effect of the damper itself. The vast amount of different combinations with respect to wind velocity and direction, levels of turbulence and other factors also increase the need for large amounts of data to be analyzed, as simple relations between the wind velocity and response alone does not exist.

In addition to the varying response of the same hanger depending on the temperature and wind conditions, differences in response between subsequent hangers are also observed. The tension in the hangers studied in this thesis might be different by design, causing different modes to be activated for equal conditions. Where vibrations in hanger 3 had maximum acceleration amplitudes of  $10m/s^2$  with two dampers installed, hanger 2 and 3 had acceleration amplitudes of  $20m/s^2$  the 27<sup>th</sup> of February, both with two dampers installed. In comparison, maximum acceleration amplitudes for hanger 1 without any dampers installed was  $50m/s^2$ . Choosing to compare the same time series, the uncertainty regarding differences in the hanger properties is introduced. On the other hand, choosing to compare the response of the same hanger, the uncertainty regarding differences in wind conditions and temperature is introduced. Needless to say, the estimation of the effectiveness of the damper will undoubtedly be affected by the choice of basis for comparison.



## 8 Discussion

This chapter will cover discussions on the correlation of the damper test and findings from the measurement data. It will also cover discussions regarding the possible causes of damper failure, and measures to reduce the occurrence and magnitude of the vibrations in the hangers. Lastly, limitations of the study will be presented.

### 8.1 Correspondence of the Damper Tests and Measurement Data

The results from the damper test performed by *TESolution* indicated that maximum energy dissipation through the dampers occur at an excitation frequency of around 20 Hz. This is in good correspondence with the trend in the response of the hangers, where dampers were found to effectively eliminate the peak in vibration response for hanger 1, occurring at wind speeds of around 10 m/s, corresponding to a vibration frequency of about 21 Hz. Furthermore, findings from the damper test imply a further increase in excitation frequencies above 20 Hz results in a monotonic and rapidly declining damper effectiveness. Measurement data from the hangers at the bridge site demonstrate similar characteristics. As presented in section 7.1.1, the response of the hangers with one or two dampers installed is characterized by a monotonic increasing trend in response amplitudes for increasing mean winds, or increasing vibration frequencies. Hence, the decline in energy dissipation through the damper is coinciding with the increase in response amplitudes for the hangers with one or more dampers installed.

The dynamic damper test included in the *TESolution damper performance test* also investigated the difference in response for an unused damper compared to the same damper subjected to a fatigue test. For the original unused damper, *TESolution* found a reduction of about 53% in the energy dissipation through the damper as the excitation frequency was increased from 20 to 30 Hz. As for the damper subjected to a fatigue test prior to the dynamic test, the reduction in damping effects were even more substantial with a corresponding 68% decrease in energy dissipation as the excitation frequency was increased from 20 to 30 Hz. Hence, the number of oscillating cycles the damper has been exposed to significantly influences the response and energy dissipating properties of the damper. More details on the duration and the way the fatigue test was performed will be covered in section 8.2.3. Based on observations from the measurement data, the damper subjected to the fatigue test is expected to demonstrate behaviour more alike the actual behaviour of the dampers installed at the Hålogaland bridge. Presuming the actual damper behaviour is much alike the damper subjected to the fatigue test, the energy dissipation through the dampers for a vibration frequency of 30 Hz is very limited. However, the actual decrease in damping as the excitation frequency goes from 20 to 30 Hz is difficult to validate through measurement data as the response of the hangers differ from one time series to the next. Isolating the response of the hangers influenced by the damper alone is difficult to achieve as other random phenomena as wind gusts will occur in an uncontrolled environment, undoubtedly influencing the response of the hangers. The only thing certain is that the response of the hangers are of the same order of magnitude for vibration frequencies around 30 Hz, suggesting the dampers have little or no effect.

As presented in section 4.1, the damping effects of the SD is caused by the energy dissipation through dry friction as bending is induced in the messenger cable. Consequently, displacements of the two masses of the SD should provide indirect information regarding the energy dissipation. Results from the damper test, further elaborated in section 4.3, imply the response of the two damper masses is shifted as the excitation frequency goes from 15 Hz to 30 Hz. For the excitation frequencies below 20 Hz, large displacements in the bottom mass and corresponding substantial bending of the bottom messenger cable occurs. For excitation frequencies in the range of 20-25 Hz, the displacement amplitudes of the bottom mass is somewhat reduced, nevertheless, still large enough to induce bending in the messenger cable. Additionally, displacements of the top mass resulting in bending of the top messenger cable occurs, causing both messenger-cables to contribute to the total energy dissipation. In contrast, for an excitation frequency of 30 Hz, only the top mass is found to induce any significant bending in the messenger cable, as the displacements of the bottom mass are negligible. Hence, the top messenger cable is solely responsible for the energy dissipation corresponding to an excitation frequency of 30 Hz, in contrast to both cables for lower modes. Comparing findings from the test conducted by *TESolution* to the damper displacement measurements, the reduction in energy dissipation for higher excitation frequencies is expected to be caused by the reduction in bending of the bottom messenger cable.

Important to note is that the damper test at NTNU was executed using a constant RMS value of the acceleration equal to  $5m/s^2$ . Although the magnitude of the accelerations are fairly representative for the response of the hangers with one or two dampers installed, the displacements are not. The displacement amplitudes during the damper test was smaller than the ones occurring in the hangers at the bridge site. As the SD exhibits nonlinear behaviour, meaning the effect of the damper is dependent upon both the excitation amplitude and frequency, the energy dissipation might be slightly different for the two cases. Nevertheless, the primary goal of this test was to investigate the displacements of the different damper parts at different frequencies, to analyze the magnitude of the response and which of the two masses are activated for different frequencies. Only the main trends in the response have been analyzed. Consequently, the different displacement amplitudes is not expected to have influenced the findings in any significant way.

## 8.2 Possible Causes of Damper Failure

As no acceleration data nor observations of the vibration response during the storm Frank is available, the characteristics of the vibrations, and hereby the actual cause of the damper failure is to this date unknown. Response characteristics of the hangers during strong winds are in general highly uncertain, as only limited amount of data exists during these conditions. Following this, research and observations of other suspension bridges during strong winds are presented. The findings will be compared to the wind and environmental conditions during the storm, to assess the plausibility of the theory. In addition, findings from the damper tests will be compared to the broken dampers to investigate whether there is any correlation in terms of displacement shape and fracture point. Amongst relevant topics considered as the cause of the damper failure is fatigue fracture due to continuous excitation. Furthermore, aerodynamic instabilities causing large amplitude vibrations and corresponding damper failures have been reported for other suspension bridges during strong winds<sup>[7]</sup>, and will also be considered as a possible cause of failure.

### 8.2.1 Background Information

Several dampers at the Hålogaland bridge was broken during the storm Frank that hit northern parts of Norway the 20<sup>th</sup> of January 2021, and lasted 2 days. The weather station “E10 Skitdalshøgda”, run by the Norwegian road administration and located approximately 20 km north-east of the Hålogaland bridge, have measurement data of wind speeds up to 36.7 m/s during the storm<sup>[33]</sup>. Winds were mainly easterly or south-easterly, with temperatures in the Narvik-area of  $-4^{\circ}\text{C}$  to  $-10^{\circ}\text{C}$  during the storm. After the storm had passed, the remaining parts of the broken dampers was sent back to the producer, TESolution, where the dampers were examined and a damper performance test was executed. The test concluded that the damage on the dampers must have been caused by vibration and/or environmental factors other than the design conditions. It is also mentioned that the fatigue life of the Stockbridge damper cannot be guaranteed if the cable is continuously excited by vibrations of high amplitudes such as galloping or parametric excitation.

### 8.2.2 Large Amplitude Vibrations

During the storm, icing was a commonly reported problem<sup>[33]</sup>. Research performed by *Demartino et al* and *Li et al* indicate that iced hangers are more prone to aerodynamic instabilities, causing large-amplitude vibrations, due to the increase in section irregularities compared to the dry hanger<sup>[34;35]</sup>. Findings are also supported by observations made at The Great East Belt Bridge in Denmark, where thinly iced hangers are observed in cases of violent vibrations<sup>[36]</sup>. Aerodynamic instabilities of this kind, often referred to as *den Hartog Galloping*, might occur for a variety of cross sectional shapes not including the perfectly shaped cylinder<sup>[37;2]</sup>. However, only small irregularities are needed for instabilities to occur, where surface roughness in some cases is sufficient for these vibrations to be induced. In the same manner as vibrations are dependent upon the nature of the surface roughness, possible instabilities caused by ice accretion depend on the shape and surface roughness of the icing<sup>[34]</sup>. The shape and thickness of the icing is found to depend on several different factors such as mean wind velocity, external temperature and diameter of the cylinder<sup>[35]</sup>. If the wind directions have been relatively stable during the accretion of the ice, the cross section with the ice included will be shaped somewhat elliptical. Ellipses are especially prone to galloping instability when the direction of the wind is not aligned with the symmetry line of the cross section, where flow aligned with the symmetry line is indicated to the left in figure

8.1<sup>[37]</sup>. Research performed by *Demartino et al* suggest that only slight changes in the angle of attack compared to the direction of where the ice was built up, indicated by  $\theta$  in the figure, will cause aerodynamic instabilities in the hanger<sup>[34]</sup>.

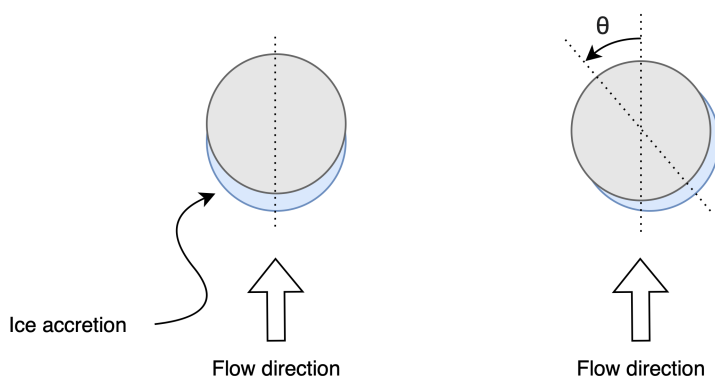


**Figure 8.1:** Ice accretion on hangers.

Wake-induced flutter, sometimes referred to as wake-induced galloping, is another aerodynamic phenomenon known to induce vibrations of large amplitudes. The phenomenon occurs when wake interference of an upstream hanger causes the leeward hanger to vibrate and become unstable<sup>[38;20]</sup>. Also for this phenomenon, iced hangers are found to reduce the critical wind speed of which wake induced galloping occurs<sup>[35]</sup>. However, observations of wake induced galloping in suspension bridges apply to the bridges where the hanger consists of several separate cables, as in the hangers of the Xihoumen Bridge in China<sup>[5]</sup>. The longest wake length of which interference of the downstream hanger will occur is somewhat uncertain as most research cover distances up to  $20D$ , where  $D$  is the diameter of the cylinder<sup>[39]</sup>. With a hanger diameter of 0.086 meters at the Hålogaland bridge,  $20D$  would correspond to 1.72 meters. Given an easterly wind direction, the actual distance between the leeward and windward hanger at the Hålogaland bridge is approximately 17 meters, suggesting wake interference is unlikely to happen between the hangers. In addition, wake effects is independent of the natural frequencies and hereby also the length of the hangers, which should imply vibrations in all hangers along the bridge would occur. However, observations of hanger response in suspension bridges suggest vibrations mainly occur in the longest hangers, the ones adjacent to the bridge towers<sup>[40]</sup>.

Corresponding to the theory of wake interference between bridge hangers, *Chen et al* found that vibrations of the hangers located in the wake of an upstream tower are greatly amplified<sup>[7]</sup>. However, wind directions during the storm Frank was easterly to south-easterly, causing the wake of the east bridge towers to mainly affect the west bridge towers. For a south-easterly wind direction, the direction of the location of hanger 1 would still deviate from the wind direction by about  $17.4^\circ$ . Although, the bridge tower is far wider than the hangers, and research suggest wake interference might occur in hangers with a  $15^\circ$  deviation from the angle of attack on the bridge tower<sup>[39]</sup>. Following this, wake interference of hanger 1 might be theoretically possible. However, hanger 2 would be located even further away from the wake of the tower, both in terms of distance and direction. In all, wake interference from the bridge towers seems like an unlikely cause of the violent vibrations causing the dampers to fail.

Observations of large-amplitude vibrations of the hangers in close proximity to the towers were also observed during a typhoon in China. The typhoon had wind velocities of 25-30 m/s and mean wind directions perpendicular to the bridge longitudinal direction, corresponding to measurements during the storm Frank. Despite the wind direction, the most violent vibrations was observed in the hangers located closest to the bride towers. Hangers at both sides of the bridge deck had vibrations of equivalent magnitude, excluding wake galloping as a likely cause of the vibrations. Also, the frequency of the vibrations was below 1 Hz, excluding VIV as the cause of the vibrations. Findings included the modes of the longest hangers and the main cables were closely spaced during strong winds. Following this, the authors concluded the violent vibrations of the hangers located close to the bridge tower might have been caused by the vibrations of the main cables of the bridge<sup>[6]</sup>. Research from 2021 performed by *Zhang et al* found that buffeting response of the main cables drive the longest hangers into resonance, and that motions in the longitudinal direction of the bridge is larger than the motions in the lateral direction. Moreover, findings included main cable excitation of just a few millimeters was enough to initiate hanger vibrations with corresponding displacements of up to 300 mm for the studied bridge with a main span of 1666 meters<sup>[40]</sup>.

### 8.2.3 Fatigue Life of the Damper

Vibrations caused by shedding vortices diminish as the displacements become sufficiently large<sup>[2]</sup>. Following this, the response related to VIV is more critical in terms of the fatigue life of the hanger and damper-system<sup>[8]</sup>. The author's attempt to find research related to VIV in suspension bridge hangers, where the vibration frequencies are higher than 30 Hz, is to date unsuccessful. A lot of research has been performed within the field of wind induced vibrations in overhead transmission lines, where vibration frequencies in the range of 3 Hz up to 150 Hz is to be expected<sup>[41]</sup>. However, due to the differences in structural properties, wind characteristics of the corresponding vibration frequencies involve laminar wind flows in the velocity range of 2-15 MPH, equivalent to about 0.9-6.7 m/s<sup>[42]</sup>. Consequently, the characteristics of the strong winds during the storm and whether the wind flow was stable enough to excite the hangers corresponding to high frequency VIV remain uncertain.

Regardless whether the hangers were excited by shedding vortices or other phenomenons causing large amplitude vibrations, the cause of the damper failure might still have been fatigue in the messenger cables. Aiming to assess the fatigue effects on the SD, TESolution performed a fatigue test on one of the dampers still intact from the Hålogaland bridge. A displacement amplitude of  $\pm 1$  mm and an excitation frequency of 26 Hz was used. The test lasted for a total of  $10^7$  cycles, equivalent to 107 hours, or 4 days and 11 hours. Knowing that these dampers are installed to dissipate energy under operating conditions for several years, a fatigue test with a duration of less than 5 days, and with displacement amplitudes similar to what is observed on a regularly basis, is of no significance in evaluating the fatigue life of the dampers. An other fatigue test with an excitation frequency of 23 Hz and corresponding displacement amplitude of  $\pm 3$  mm was also performed. However, the test had the same amount of cycles as the previous one, now with a total duration of 120 hours, still insignificant for the evaluation of the fatigue life of the damper.

### 8.2.4 Lessons from the Damper Test

Excitation frequencies below 15 Hz was initially excluded from the damper test as the response amplitudes are fairly low for the corresponding frequencies, regardless of whether dampers are installed or not. However, a test was performed to investigate the displacement response of the damper for low vibration frequencies, to be able to assess whether large amplitude vibrations or fatigue is the most likely cause of the damper failure. The damper test was performed for an excitation frequency of 5 Hz, but with a corresponding RMS acceleration of  $2 \text{ m/s}^2$  instead of  $5 \text{ m/s}^2$ , as displacements were too large for the latter option. Results indicated that the bottom mass obtained large displacements while the displacements of the top mass were negligible, as shown in figure 8.2. Also notice the relative displacements of the mid point of the damper to the bottom mass and the top mass. The relative displacement between the midpoint of the damper and the top mass is almost non-existent, and will accordingly not induce any bending and corresponding friction in the messenger cable connecting the top mass to the clamp. In contrast, the relative displacement between the bottom mass and the clamp is significant, causing great bending in the messenger cable.

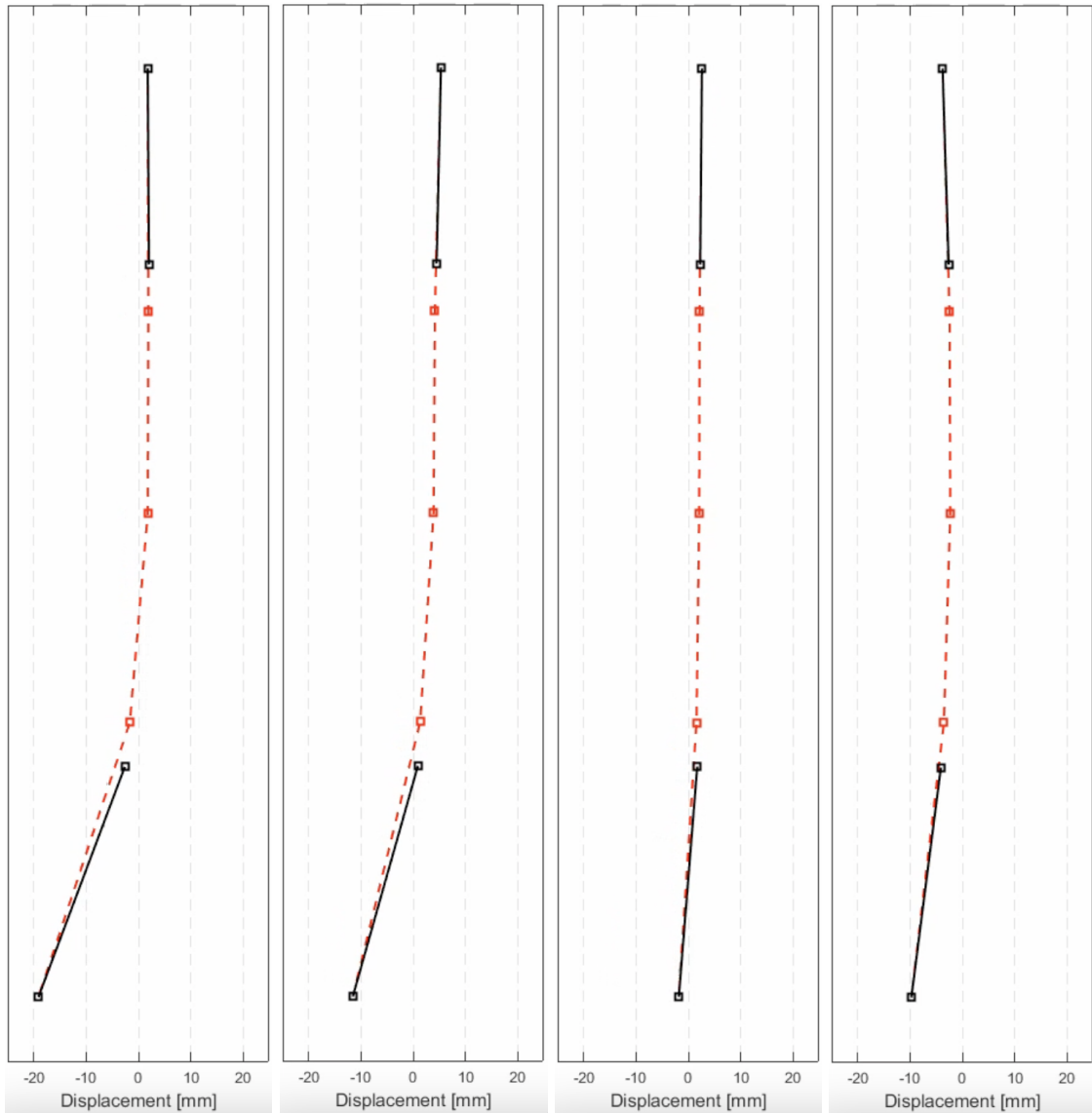


**Figure 8.2:** Displacements for an excitation frequency of 5 Hz and RMS acceleration of  $2 \text{ m/s}^2$ . Courtesy of Tengjiao Jiang.

Investigations of the broken dampers, performed by *TESolution*, include findings that the bottom messenger cable, connecting the biggest mass to the clamp, was most frequently damaged during the storm. For the given wind velocities during the storm, any occurrence of VIV would have a corresponding vibration frequency of 30 Hz or higher. For equivalently large vibration frequencies, the damper test suggest the top mass will obtain relatively large displacements, whilst the displacements of the bottom mass would be negligible. However, the response characteristics corresponding to high frequency VIV does not match the findings from the broken dampers, where the bottom cable was most frequently damaged. Hence, regular VIV during the storm is not likely to be the cause of the damper failure. Having said that, fatigue caused by VIV over a longer period of time prior to the storm might have influenced the fatigue life of the dampers, causing the dampers to fail as a random event during the storm.

### 8.3 Measures to Reduce the Magnitude of the Vibrations

Regardless of the cause of the damper failure, measures to reduce the magnitude of the vibrations in the hangers will always be beneficial to the structural health of the bridge. Following this, suggestions are made regarding possible measures to reduce the magnitude of VIV, increasing the fatigue life of the hangers, as well as measures to reduce the risk of large amplitude vibrations during strong winds.

#### 8.3.1 Amount of Dampers and Damper Location

As TESolution proposes in their damper performance report, an additional third damper, installed to mitigate vibrations in the cross-flow direction, would be beneficial to effectively reduce the magnitude of the vibrations. Findings from full scale experimental studies performed by *Di et al* support this statement<sup>[9]</sup>. For the Hålogaland bridge, the installation of three dampers in total would give two dampers in the x-direction and one in the y-direction. An other factor to consider for the total damping performance is the frequency tuning of the SD. Measurement data and results from *TESolution damper test* indicate that the dampers installed at the Hålogaland bridge successfully mitigates vibrations of frequencies around 20 Hz, whereas damping effects for vibrations of higher frequencies are reduced. Assuming a third damper is installed, an option would be to alter the frequency tuning of the additional damper in such a way its natural frequencies are increased, improving the damping effects at higher frequencies.

The location of the damper with respect to node or anti-node position might also influence the energy dissipation through the damper at higher frequencies. If the mode shape results in a node-position of the damper, the corresponding excitation amplitude will be close to zero. As found by *Di et al*, owing to the large inherent damping of the SD, relatively large hanger accelerations are required to activate the SD<sup>[9]</sup>. Hence, if placed at a node-position, the damper will be far less effective in terms of dissipating energy from the hanger. However, findings from the damper test conducted by *TESolution* verify the decline in energy dissipation for higher frequencies without the interaction of node or anti-node location. Consequently, the damper location may not solely be responsible for the reduction in energy dissipation, but might amplify the reduction if placed closer to a node-position for higher frequencies.

#### 8.3.2 Surface Roughness of Hangers

Challenges related to wind induced vibrations in hangers of suspension bridges and cables of cable-stayed bridges are often mitigated by physical installations of viscous dampers or TMD's<sup>[43;44;45]</sup>. Within the marine industry, flexible risers as well as pipelines are some of the structures susceptible to flow induced vibrations due to shedding vortices, equivalent to the previously described VIV of bridge hangers. Applicable damping systems for marine structures are more comprehensive than the ones used in bridge engineering<sup>[46;47]</sup>. Consequently, different approaches to vibration mitigation has been investigated, where the relation between surface roughness and flow induced vibrations are one of the areas studied. Research performed by *Gao et al* found that large surface roughness resulted in lower displacement amplitudes and smaller lock-in region, compared to the smooth cylinder<sup>[48]</sup>.

Surface roughness often refers to the unintentional roughness due to fabrication, however, other forms of roughness is intentional and systematic, like the dimples and helical strakes shown in figure 8.3. Dimples, equivalent to those found in golf-balls, have been investigated where the aerodynamic properties of the dimpled cylinder is compared to the corresponding properties of the regular smooth cylinder. Results indicate the effect of dimples on the aerodynamic response of the cylinder is highly dependent on the location of the dimples, their depth and their geometry<sup>[34]</sup>. Nevertheless, with the right configuration of dimples, a reduction in drag and fluctuating loads causing vibrations are expected<sup>[49;50]</sup>. Other research have investigated the effect of helical strakes wrapped around cylindrical shaped bodies to suppress VIV<sup>[34;51]</sup>. Results indicate the vibration amplitude of the cylinder with helical strakes is reduced by up to 98% compared to the smooth cylinder, due to the elimination of vortex shedding and lock-in phenomena<sup>[52]</sup>.

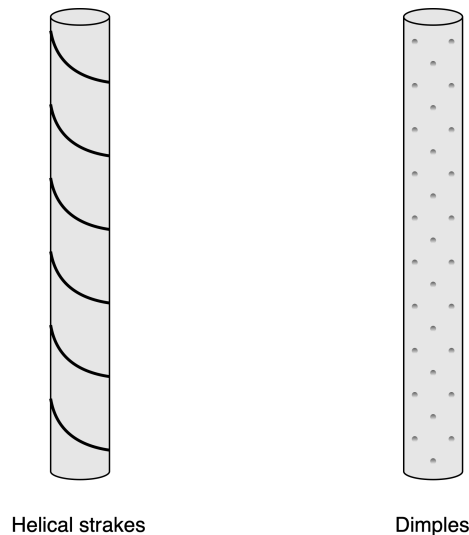


**Figure 8.3:** Illustration of helical strakes and dimples.

### 8.3.3 Hanger Material

Assuming the cause of the damper failure is the vibrations in the main cables and their closely spaced vibration frequencies to the natural frequencies of the longest hangers, one option would be to change the natural frequencies of the corresponding hangers. As *Zhang et al* mentions, the use of carbon fiber-reinforced polymer with its high tensile strength would reduce the mass of the hangers, increasing the natural frequencies of the hangers. Corresponding numerical analyses suggest replacing the hanger material would significantly reduce the response amplitudes of the longest hangers<sup>[40]</sup>. Although not entirely equivalent to the Hålogaland bridge due to the different connections, hangers of carbon fiber-reinforced polymer have been used in a full scale operating suspension bridge with great success<sup>[53]</sup>. However, little or no research has been performed investigating the effect of changing the hanger material with respect to other types of cable vibrations, such as VIV.

## 8.4 Limitations of the Study

Research conducted in the course of this thesis is solely confined to the response of the hangers and the corresponding wind measurements. As previously mentioned, wind measurements are sampled at an anemometer located 80-120 meters from the investigated hangers. However, no research have been performed in order to asses the homogeneity of the wind field, resulting in uncertainty whether the measurements are able to represent the actual wind conditions for the hangers studied in this thesis. Furthermore, the influence of the bridge tower on the response of the hangers, discussed in section 6.1.1, is not investigated further. As no wind measurements at the actual location of the hangers are conducted, the statements in the discussion of the above mentioned section remain unverified.

Influence on the hanger response caused by vibrations or displacements in the main cables or bridge deck is not taken into account. The influence of the position of the damper was introduced in section 4.1.1, and have later on in this thesis been suggested as a possible contributor to the reduced damping effects for higher frequencies. As mode shapes of the hangers are not investigated in this thesis, the actual location of the dampers and sensors, with respect to node or anti-node position, remain unknown. Lastly, and most important of all; only a small amount of data have been thoroughly investigated and analyzed. Verified by the results of the research, a numerous of different factors are known to influence the response of the hangers. To reduce the statistical bias in the research, more data needs to be analyzed.

## 9 Conclusion

The vibration frequencies of the hangers at the Hålogaland bridge are in good agreement with the derived theoretical shedding frequencies corresponding to VIV. The presence and magnitude of the vibrations is found to be dependent upon the wind direction and the corresponding stability in the wind direction, the magnitude of turbulence, and the mean wind. Wind conditions favourable for the presence of large amplitude VIV is stable winds of either westerly or easterly directions, corresponding to a wind direction perpendicular to the longitudinal direction of the bridge. The magnitude of the turbulence is not found to obstruct the presence of VIV, but rather influence the bandwidth and amplitudes of the vibration response. Furthermore, a number of factors believed to influence the response of the hangers have not been investigated thoroughly. Amongst those are temperature effects, tower shadowing and differences in tension between the hangers.

Validated through measurement data, the dampers are found to effectively reduce the magnitude of the response for vibration frequencies lower than 25 Hz. This is clearly demonstrated as the peak in response amplitudes for vibration frequencies of around 21-22 Hz is eliminated after hanger 1 was installed with dampers. In contrast, the dampers are found to have significantly reduced damping effects for vibration frequencies upwards of 25 Hz. This is validated by the monotonic increase in response amplitudes for increasing vibration frequencies in the hangers with one or more dampers installed. For vibration frequencies upwards of 30 Hz, the response amplitudes of the hangers studied in this thesis are of the same order of magnitude, regardless of the damper installation on the given hanger. The above described observations are in good correspondence with the findings from the damper test performed by *TESolution*, where a peak in energy dissipation is obtained for a vibration frequency of 20 Hz, followed by a rapid and monotonic decline in energy dissipation for exciting frequencies upwards of 20 Hz. According to the damper test, some damping properties remain for higher frequencies, as demonstrated in the measurement data by the minor differences in response amplitudes for hanger 2 and 3, where hanger 3 has an extra damper compared to hanger 2. However, differences in response amplitudes for the above mentioned hangers is present even when both hangers have two dampers installed, suggesting differences in hanger properties might also influence the response. The displacement measurements of the damper for different excitation frequencies demonstrated low displacement amplitudes for the lower mass at higher frequencies, and correspondingly insignificant bending in the lower messenger cable. Consequently, the findings from the *TESolution damper test* and measurement data of reduced damping effects at higher frequencies is believed to be caused by the reduction in bending of the lower messenger cable.

Although response amplitudes throughout the duration of the measurement period have been analyzed, only a small amount of time series have been investigated thoroughly with the aim of characterizing the damper effect for different vibration frequencies. Consequently, the results may have been affected by the choice of time series. To improve the statistical significance of the findings, more data should be analyzed. As for the cause of the damper failure, the response amplitudes throughout the measurement period suggest no particular incidents of abnormally large amplitudes have occurred, rather moderate levels of vibration corresponding to VIV. Consequently, the theory of fatigue failure of the dampers is strengthened. However, as no measurement data of equivalently large wind magnitudes as during the storm is available, the possible occurrence of large amplitude vibrations during the storm can not be discarded.

### 9.1 Further Work

After dampers were installed on all hangers, vibration frequencies upwards of 25 Hz seems to induce the largest response amplitudes in the hangers. Affecting the fatigue life of the hangers and dampers, further work should be aimed at reducing the amplitudes of these vibrations. With the knowledge of the energy dissipation at different frequencies, a possible measure to reduce these vibrations would be to install an additional damper with higher natural frequencies, aimed to dissipate energy at higher frequencies.

Even though the SD system is an affordable option compared to many other damping systems, the total cost associated with a potential need for re-installation at a regular basis is significant. More effort and further investigations should be directed towards finding the actual cause of the damper failure, increasing the robustness of the damper for potential similar response characteristics in the future. Consequently, a thorough fatigue test of considerably longer duration and equivalent or higher displacement amplitudes is needed to evaluate the actual fatigue life of a SD. Findings in favor of the theory of large amplitude vibrations include the frequently observed



failure of the bottom messenger cable. Additionally, the fact that all dampers mounted to hanger 1 failed whilst none of the dampers mounted to hanger 3 failed, might suggest main-cable interaction. To evaluate the theory of large amplitude-vibrations, wind tunnel testing of a full-scale hanger model with damper installed during strong winds is an option. However, assuming interaction between the main cables and the hangers are likely to occur during strong winds, the need for a more comprehensive model arises. Both due to the complexity of such a substantial model and the stochastic nature of the wind loading, full scale measurements during storms or typhoons are preferable to improve the understanding of the influence the main cables have on the longest hangers.

## References

- [1] D. E Newland. An introduction to random vibrations, spectral & wavelet analysis, 2005.
- [2] Einar N Strømmen. *Theory of Bridge Aerodynamics*. Springer-Verlag, Berlin, Heidelberg, 2. Aufl. edition, 2010. ISBN 3642136591.
- [3] Hubbell power systems, 2022. URL <https://www.hubbell.com/hubbellpowersystems/en/Products/Power-Utilities/Connectors/Spacers-Dampers/Stockbridge-Dampers/Vibration-Damper/p/1683872>. "[Online; accessed 29-May-2022]".
- [4] Allan Larsen and Guy L Larose. Dynamic wind effects on suspension and cable-stayed bridges. *Journal of sound and vibration*, 334(1):2–28, 2015. ISSN 0022-460X.
- [5] Shouying Li, Chunyun Xiao, Teng Wu, and Zhengqing Chen. Aerodynamic interference between the cables of the suspension bridge hanger. *Advances in structural engineering*, 22(7):1657–1671, 2019. ISSN 1369-4332.
- [6] ZT Zhang, XB Wu, ZQ Chen, and YJ Ge. Mechanism of hanger oscillation at suspension bridges: Buffeting-induced resonance. *Journal of Bridge Engineering*, 21(3):04015066, 2016.
- [7] Wenli Chen, Donglai Gao, Hui Li, and Hui Hu. Wake-flow-induced vibrations of vertical hangers behind the tower of a long-span suspension bridge. *Engineering Structures*, 169:188–200, 2018. ISSN 0141-0296. doi: <https://doi.org/10.1016/j.engstruct.2018.05.049>. URL <https://www.sciencedirect.com/science/article/pii/S0141029618315566>.
- [8] Teng Wu and Ahsan Kareem. An overview of vortex-induced vibration (viv) of bridge decks. *Frontiers of architecture and civil engineering in China*, 6(4):335–347, 2012. ISSN 2095-2430.
- [9] Fangdian Di, Limin Sun, Lei Qin, Lin Chen, Yiqing Zou, Lijun Jiang, and Yongquan Zhu. Full-scale experimental study on vibration control of bridge suspenders using the stockbridge damper. *Journal of bridge engineering*, 25(8): 4020047, 2020. ISSN 1084-0702.
- [10] Statens vegvesen Vegdirektoratet. Hålogalandsbrua på E6 nord for Narvik påført mindre skader etter stormen Frank. <https://www.vegvesen.no/vegprosjekter/europaveg/e6halogalandsbrua/nyhetsarkiv/halogalandsbrua-pa-e6-nord-for-narvik-pafort-mindre-skader-etter-stormen-frank/>, 2021. "[Online; accessed 19-April-2022]".
- [11] Carlo Rainieri. Operational modal analysis of civil engineering structures : An introduction and guide for applications, 2014.
- [12] Anil K Chopra. Dynamics of structures : theory and applications to earthquake engineering, 2012.
- [13] Gerhart I Schuëller and Masanobu Shinozuka. *Stochastic methods in structural dynamics*, volume 10. Springer Science & Business Media, 2012.
- [14] James W Cooley and John W Tukey. An algorithm for the machine calculation of complex fourier series. *Mathematics of computation*, 19(90):249–259, 1965. ISSN 0025-5718.
- [15] Lokenath Debnath. Wavelet transforms and time-frequency signal analysis, 2001.
- [16] D Sundararajan. Fourier analysis—a signal processing approach, 2018.
- [17] F.J Harris. On the use of windows for harmonic analysis with the discrete fourier transform. *Proceedings of the IEEE*, 66(1):51–83, 1978. ISSN 0018-9219.
- [18] Robert Ashford King. Digital filtering in one and two dimensions : design and applications, 1989.
- [19] Yuegang Wang, Shao Ji, and Hongtao Xu. Non-stationary signals processing based on stft. In *2007 8th International Conference on Electronic Measurement and Instruments*, pages 3–301–3–304. IEEE, 2007. ISBN 1424411351.
- [20] Yukio Tamura and Ahsan Kareem. *Advanced Structural Wind Engineering*. Springer Japan, Tokyo, 2013. ISBN 9784431547198.
- [21] C Norberg. Fluctuating lift on a circular cylinder: review and new measurements. *Journal of fluids and structures*, 17(1):57–96, 2003. ISSN 0889-9746.
- [22] Remi Bourguet, George E Karniadakis, and Michael S Triantafyllou. Vortex-induced vibrations of a long flexible cylinder in shear flow. *Journal of fluid mechanics*, 677:342–382, 2011. ISSN 0022-1120.

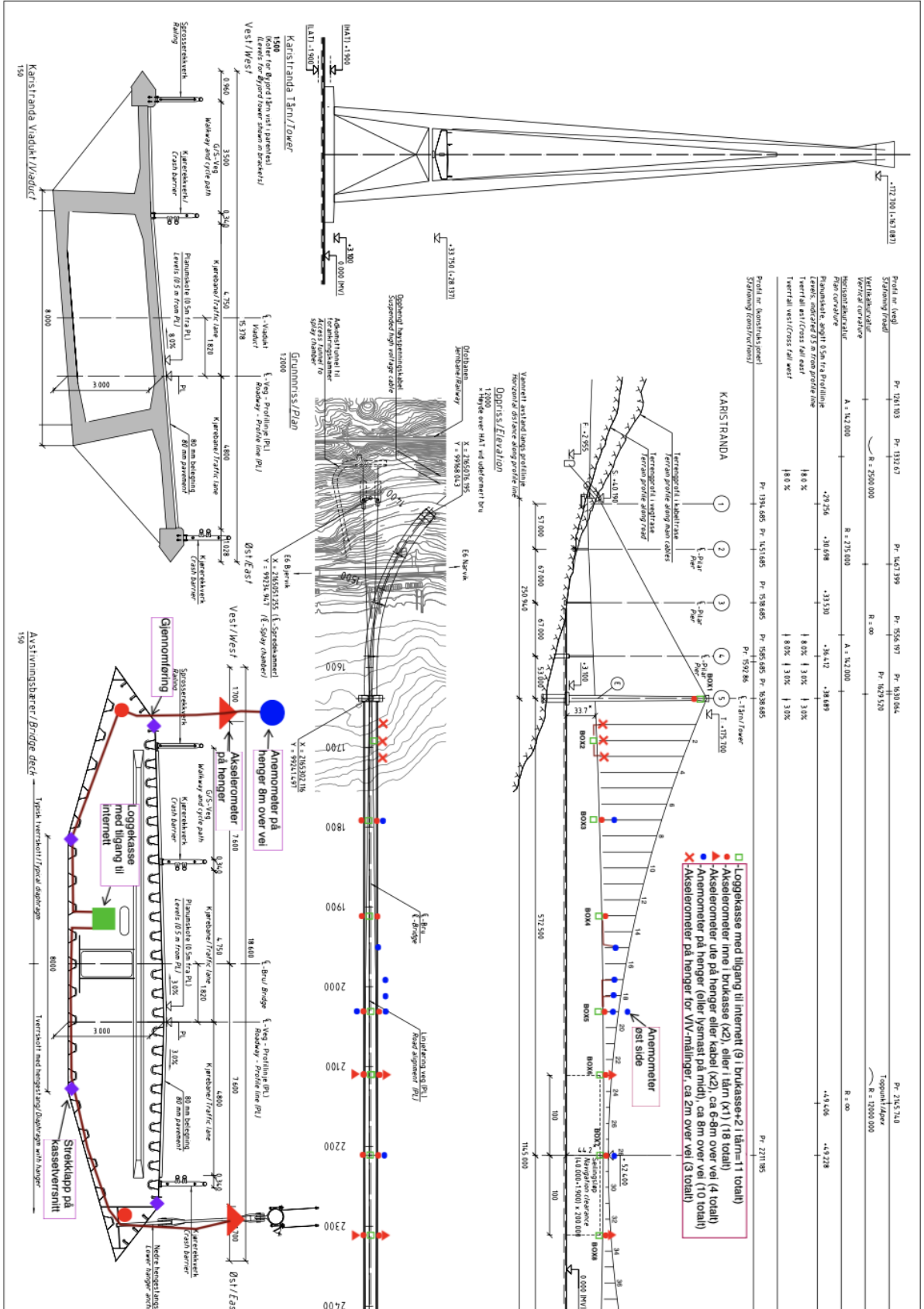
- [23] J. A Main and N. P Jones. Evaluation of viscous dampers for stay-cable vibration mitigation. *Journal of bridge engineering*, 6(6):385–397, 2001. ISSN 1084-0702.
- [24] Daniel Cantero, Ole Øiseth, and Anders Rønnquist. Indirect monitoring of vortex-induced vibration of suspension bridge hangers. *Structural health monitoring*, 17(4):837–849, 2018. ISSN 1475-9217.
- [25] D Sauter and P Hagedorn. On the hysteresis of wire cables in stockbridge dampers. *International journal of non-linear mechanics*, 37(8):1453–1459, 2002. ISSN 0020-7462.
- [26] Oumar Barry, Donatus CD Oguamanam, and Der Chyan Lin. Aeolian vibration of a single conductor with a stockbridge damper. *Proceedings of the Institution of Mechanical Engineers. Part C, Journal of mechanical engineering science*, 227(5):935–945, 2013. ISSN 0954-4062.
- [27] Francesco Foti and Luca Martinelli. Hysteretic behaviour of stockbridge dampers: Modelling and parameter identification. *Mathematical problems in engineering*, 2018:1–17, 2018. ISSN 1024-123X.
- [28] G Diana, A Cigada, M Belloli, and M Vanali. Stockbridge-type damper effectiveness evaluation. i. comparison between tests on span and on the shaker. *IEEE transactions on power delivery*, 18(4):1462–1469, 2003. ISSN 0885-8977.
- [29] Anders Brandt and Rune Brincker. Integrating time signals in frequency domain – comparison with time domain integration. *Measurement*, 58:511–519, 2014. ISSN 0263-2241. doi: <https://doi.org/10.1016/j.measurement.2014.09.004>. URL <https://www.sciencedirect.com/science/article/pii/S0263224114003832>.
- [30] K. M. M. Prabhu. Window functions and their applications in signal processing, 2014.
- [31] Stephen Orlando, Adam Bale, and David A Johnson. Experimental study of the effect of tower shadow on anemometer readings. *Journal of wind engineering and industrial aerodynamics*, 99(1):1–6, 2011. ISSN 0167-6105.
- [32] Hans Andre Mangen Olsen and Eirin Gundersen Lunde. Parametric excitation of hangers at the hardanger bridge, 2016. URL <http://hdl.handle.net/11250/2407310>.
- [33] Meteorologisk Institutt. Ekstremværet Frank er over. <https://www.met.no/nyhetsarkiv/ekstremvaeret-frank-ekstremt-kraftige-vindkast-i-deler-av-nordland-og-troms>, 2021. "[Online; accessed 09-May-2022]".
- [34] C. Demartino and F. Ricciardelli. Aerodynamics of nominally circular cylinders: A review of experimental results for civil engineering applications. *Engineering Structures*, 137:76–114, 2017. ISSN 0141-0296. doi: <https://doi.org/10.1016/j.engstruct.2017.01.023>. URL <https://www.sciencedirect.com/science/article/pii/S0141029617300974>.
- [35] Shengli Li, Qing Li, Pan Guo, Xin Liu, Dongwei Wang, and Xidong Wang. Wake-induced vibrations of iced pin joint hangers of suspension bridges based on wind tunnel test and new method of transiting test. *Structures (Oxford)*, 32:588–603, 2021. ISSN 2352-0124.
- [36] Henrik Gjelstrup and Christos Georgakis. Aerodynamic instability of a cylinder with thin ice accretion. In *8th International symposium on cable dynamics*, 2009.
- [37] G. Alonso, J. Meseguer, A. Sanz-Andrés, and E. Valero. On the galloping instability of two-dimensional bodies having elliptical cross-sections. *Journal of Wind Engineering and Industrial Aerodynamics*, 98(8):438–448, 2010. ISSN 0167-6105. doi: <https://doi.org/10.1016/j.jweia.2010.02.002>. URL <https://www.sciencedirect.com/science/article/pii/S0167610510000152>.
- [38] Haruki Fukushima, Tomomi Yagi, Takuya Shimoda, and Kyohei Noguchi. Wake-induced instabilities of parallel circular cylinders with tandem and staggered arrangements. *Journal of wind engineering and industrial aerodynamics*, 215:104697, 2021. ISSN 0167-6105.
- [39] Yu Zhou and Md Mahbub Alam. Wake of two interacting circular cylinders: A review. *The International journal of heat and fluid flow*, 62:510–537, 2016. ISSN 0142-727X.
- [40] Zhitian Zhang, Jiadong Zeng, Ledong Zhu, and Yaojun Ge. Buffeting-induced resonances of hangers at a long-span suspension bridge and mitigation countermeasure. *Journal of bridge engineering*, 26(9):4021064, 2021. ISSN 1084-0702.
- [41] N.K Vaja, O.R Barry, and E.Y Tanbour. On the modeling and analysis of a vibration absorber for overhead powerlines with multiple resonant frequencies. *Engineering structures*, 175:711–720, 2018. ISSN 0141-0296.

- [42] Robert Whapham. Aeolian vibration of conductors: Theory, laboratory simulation & field measurement. In *Electrical Transmission and Substation Structures 2012: Solutions to Building the Grid of Tomorrow*, pages 262–274. American Society of Civil Engineers, 2012.
- [43] Limin Sun, Junjie Sun, Satish Nagarajaiah, and Lin Chen. Inerter dampers with linear hysteretic damping for cable vibration control. *Engineering structures*, 247:113069, 2021. ISSN 0141-0296.
- [44] C. S Cai, W. J Wu, and X. M Shi. Cable vibration reduction with a hung-on tmd system. part i: Theoretical study. *Journal of vibration and control*, 12(7):801–814, 2006. ISSN 1077-5463.
- [45] W. J Wu and C. S Cai. Cable vibration reduction with a hung-on tmd system, part ii: Parametric study. *Journal of vibration and control*, 12(8):881–899, 2006. ISSN 1077-5463.
- [46] Ramkumar Kandasamy, Fangsen Cui, Nicholas Townsend, Choon Chiang Foo, Junyan Guo, Ajit Sheno, and Yeping Xiong. A review of vibration control methods for marine offshore structures. *Ocean engineering*, 127:279–297, 2016. ISSN 0029-8018.
- [47] B.V.E. How, S.S. Ge, and Y.S. Choo. Active control of flexible marine risers. *Journal of Sound and Vibration*, 320(4):758–776, 2009. ISSN 0022-460X. doi: <https://doi.org/10.1016/j.jsv.2008.09.011>. URL <https://www.sciencedirect.com/science/article/pii/S0022460X08007578>.
- [48] Yun Gao, Zhi Zong, Li Zou, and Zongyu Jiang. Effect of surface roughness on vortex-induced vibration response of a circular cylinder. *Ships and offshore structures*, 13(1):28–42, 2018. ISSN 1744-5302.
- [49] Bo Zhou, Xikun Wang, Wie Min Gho, and Soon Keat Tan. Force and flow characteristics of a circular cylinder with uniform surface roughness at subcritical reynolds numbers. *Applied Ocean Research*, 49:20–26, 2015. ISSN 0141-1187. doi: <https://doi.org/10.1016/j.apor.2014.06.002>. URL <https://www.sciencedirect.com/science/article/pii/S0141118714000510>.
- [50] PW Bearman and JK Harvey. Control of circular cylinder flow by the use of dimples. *AIAA journal*, 31(10):1753–1756, 1993.
- [51] Yun Gao, Shixiao Fu, Leixin Ma, and Yifan Chen. Experimental investigation of the response performance of viv on a flexible riser with helical strakes. *Ships and offshore structures*, 11(2):113–128, 2016. ISSN 1744-5302.
- [52] T. Zhou, S.F. Mohd. Razali, Z. Hao, and L. Cheng. On the study of vortex-induced vibration of a cylinder with helical strakes. *Journal of Fluids and Structures*, 27(7):903–917, 2011. ISSN 0889-9746. doi: <https://doi.org/10.1016/j.jfluidstructs.2011.04.014>. URL <https://www.sciencedirect.com/science/article/pii/S0889974611000776>.
- [53] Zhi Fang, Kuangyi Zhang, and Bing Tu. Experimental investigation of a bond-type anchorage system for multiple frp tendons. *Engineering Structures*, 57:364–373, 2013. ISSN 0141-0296. doi: <https://doi.org/10.1016/j.engstruct.2013.09.038>. URL <https://www.sciencedirect.com/science/article/pii/S0141029613004501>.

# Appendix

## A Technical Drawings and Installation Configurations

### A.1 Sensor Overview



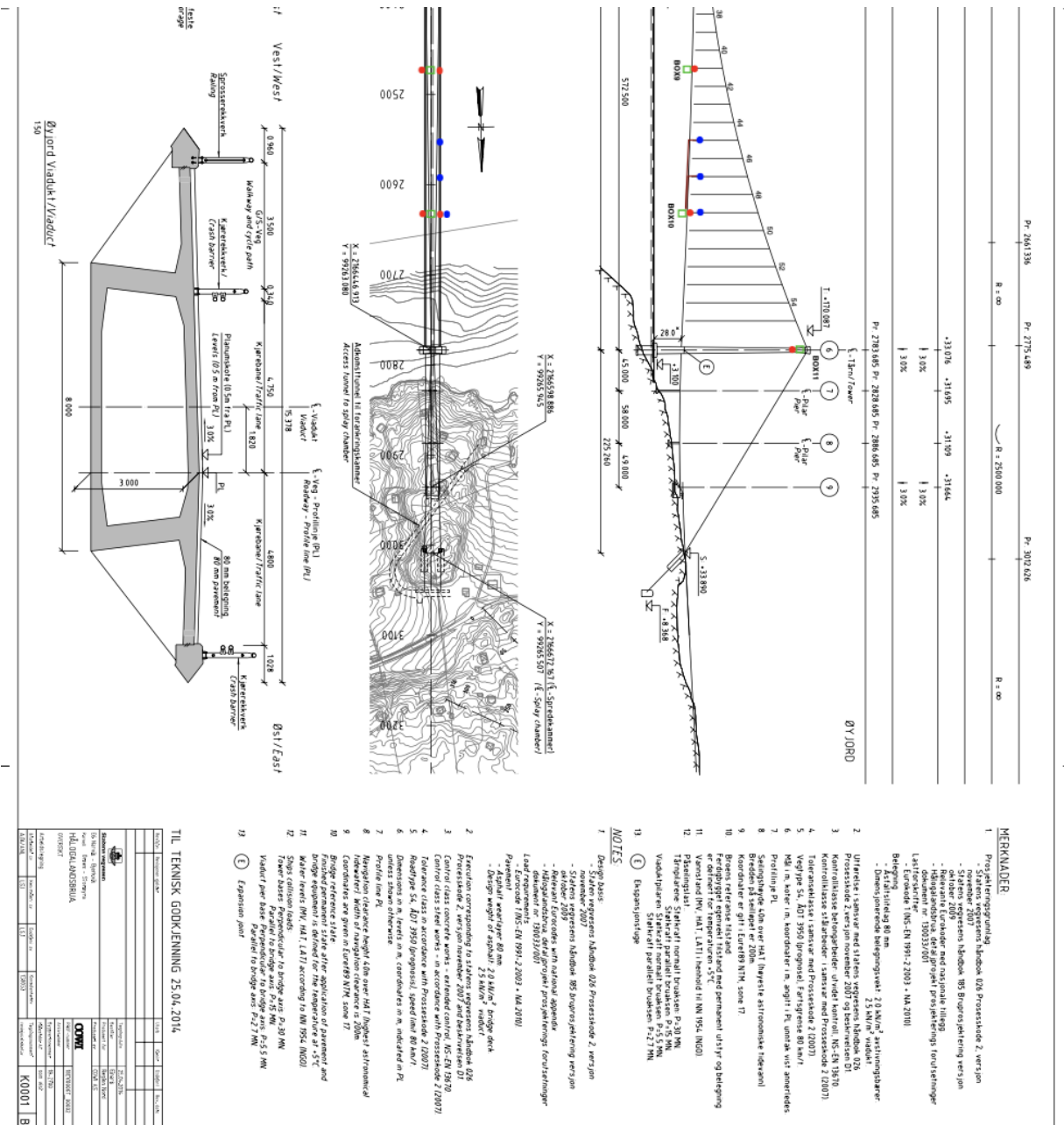


Figure A.1: Sensor overview



## A.2 Anemometer Installation



**Figure A.2:** Anemometer at hanger 7, mounted to the south-side of the hanger.



### A.3 Connections of the Hangers



**Figure A.3:** Connection of the hangers to the bridge deck, with equivalent connections to the main cables.



## B Damper-test

### B.1 Tracking Points

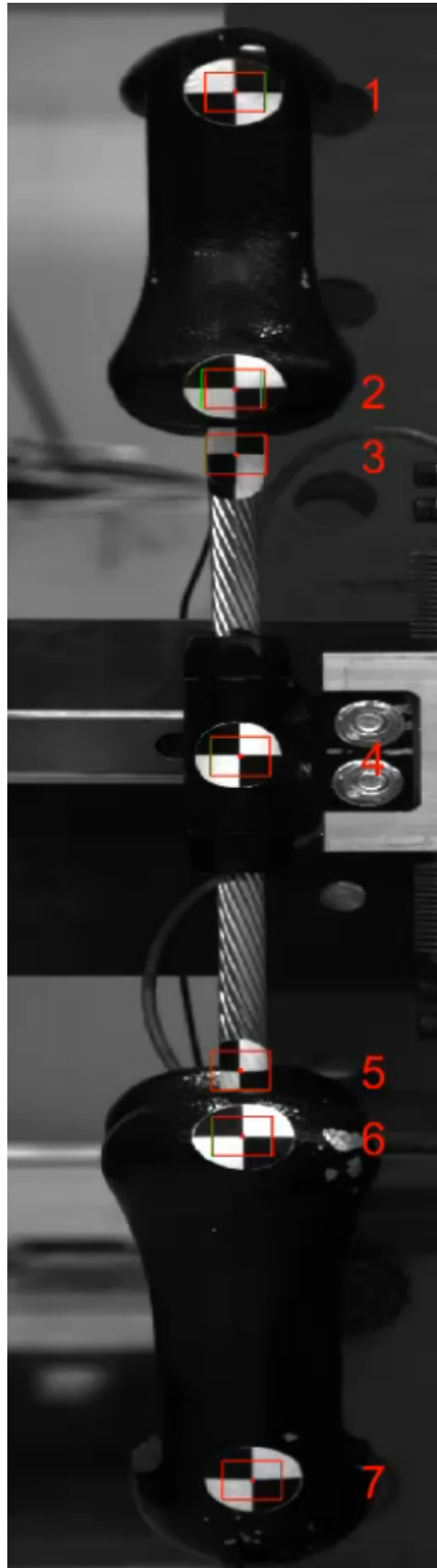


**Figure B.1:** Tracking points with corresponding numbering.

## C Python-scripts

### C.1 clean\_data.py

```
1 import numpy as np
2 from scipy.interpolate import interp1d
3
4
5 def remove_error(data, fs, status):
6     '''
7     -----
8     Inputs:
9     data : time series
10    fs : sampling frequency
11    status : vector of status codes from the sensor
12
13    Outputs:
14    newData : cleaned time series
15    error_ratio : amount of error values in time series
16    -----
17    Function returns the clean time series with a time vector. Time
18    is assumed to start from zero. The new series have the same sampling rate as the input
19    Linear interpolation is conducted to preserve the sampling rate
20    '''
21    # Generate time vector
22    l = np.max(np.shape(data))
23    t = np.arange(0, l) * 1 / fs
24    t1 = t # Store initial time vector
25
26    # Deleting the values that have error
27    error_ind = np.where(np.logical_and(status != '00', status != '0A'))[0]
28
29    # Apply linear interpolation if there are error values
30    # Have to do a for loop to be able to differentiate between direction and the other
31    # components
32    if np.size(error_ind) != 0:
33        data = np.delete(data, error_ind, axis=0)
34        t = np.delete(t, error_ind)
35        newData = np.zeros((l, 3))
36        for i in range(3):
37            if np.size(data[:, i]) == 0:
38                newData[:, i] = np.zeros((l, np.shape(data[:, i])[1]))
39                error_ratio = 1
40            # elif i==0:
41            #     func = lambda x, y, xi : interp1d(x, y)(xi)
42            #     newData[:, i] = angcall(func, l, [t, data[:, i], t1])
43            #     error_ratio = np.size(error_ind)/l
44            else:
45                newData[:, i] = interp1d(t, data[:, i])(t1)
46                error_ratio = np.size(error_ind) / l
47        else:
48            newData = data
49            error_ratio = 0
50    return newData, error_ratio
51
52
53 def remove_std(data, fs, x):
54     '''
55     Input
56     x : discard values greater than x*std in an absolute manner
57     data : time series
58     fs : sampling frequency
59     min : time interval in minutes for standard deviation estimate
60
61     Output
62     datn : time series
```

```

63     stdtrig : bool proclaiming if there were any values exceeding limit
64     -----
65     Function discards values larger than x times the standard deviation in an absolute
66     sense.
67     Returns a clean time series with same sampling rate as input. Linear interpolation is
68     conducted
69     to preserve the sampling rate.
70     '''
71     # datd = signal.detrend(data, axis=0)
72     datd = data
73     # Generate time vector
74     l = np.max(np.shape(data))
75     t = np.arange(0, l) * 1 / fs
76     t1 = t
77
78     ind = []
79     datn = np.zeros((1, 2))
80     for i in range(2):
81         dummy = np.argwhere(datd[:, i] > np.mean(datd[:, i], axis=0) + x * np.std(datd[:,
82             i], axis=0))
83         dummy2 = np.argwhere(datd[:, i] < np.mean(datd[:, i], axis=0) - x * np.std(datd[:,
84             i], axis=0))
85         ind = np.concatenate((dummy, dummy2))
86
87         if np.size(ind) != 0:
88             stdtrig = True
89         else:
90             stdtrig = False
91
92         if stdtrig:
93             ind = np.sort(ind, axis=0)
94
95             dat = np.delete(datd[:, i], ind, axis=0)
96             t = np.delete(t1, ind)
97
98             datn[:, i] = interp1d(t, dat)(t1)
99         else:
100            datn[:, i] = data[:, i]
101     return datn, stdtrig

```

## C.2 functions.py

```

1  import numpy as np
2  from pandas import DataFrame
3
4  def moving_mean(array, window_size, f_s):
5      """
6      This function gives the running mean
7
8      Arguments
9      -----
10     array : double
11         The time series to find the running mean of
12     window_size : double
13         Size of averaging window, given as size of the total array
14     f_s : double
15         Sampling frequency of the array
16
17     Returns
18     -----
19     mean_values : double
20         running mean values of the entire input array
21     t_meanValues : double
22         time array for mean_values
23

```

```

24     Reference :
25
26     """
27     # mean_values = np.convolve(array, np.ones(window_size), 'valid') / window_size
28     mean_values = np.array(np.squeeze(DataFrame(array).rolling(window=int(window_size),
29         center=True).mean()))
30     t_meanValues = np.arange(0, len(mean_values))/f_s
31
32     return t_meanValues, mean_values
33
34 def moving_std(array, window_size, f_s):
35     """
36     This function gives the running mean
37
38     Arguments
39     -----
40     array : double
41         the time series to find the running standard deviation of
42     window_size : double
43         size of averaging window, given as size of the total array
44     f_s : double
45         sampling frequency
46     Returns
47     -----
48     standard_deviation : double
49         running mean values of the entire input array
50     t_standardDeviation : double
51         time array for the standard deviation array
52
53     Reference:
54
55     """
56
57     standard_deviation = np.array(np.sqrt(np.squeeze(DataFrame(np.square(array)).rolling(
58         window=int(window_size), center=True).mean()) - np.square(np.squeeze(DataFrame(
59         array).rolling(window=int(window_size), center=True).mean()))))
60     t_standardDeviation = np.arange(0, len(standard_deviation))/f_s
61
62     return t_standardDeviation, standard_deviation

```

### C.3 acc\_response.py

```

1  import matplotlib.pyplot as plt
2  import matplotlib.colors
3  import numpy as np
4  from nptdms import TdmsFile
5  from functions import moving_mean
6  import clean_data as cd
7  from scipy import signal
8
9  plt.rcParams['agg.path.chunksize'] = 1000000
10
11
12  plt.close('all')
13  """
14  Data from anode002 - Acceleration data for the hangers
15  Data from anode003 - Wind data
16  """
17
18  # Dampers were installed on all hangers the 20th of december 2021
19
20  file_path = "2021-07-16-08-00-00Z.tdms"
21
22  basepath_acc = "/Users/ingvildsolheim/Documents/Masteroppgave/tdms-files/anode002/"
23  acc_tdms_file = TdmsFile.read(basepath_acc+file_path)

```

```

24
25 basepath_wind = "/Users/ingvildsolheim/Documents/Masteroppgave/tdms-files/anode003/"
26 wind_tdms_file = TdmsFile.read(basepath_wind+file_path)
27
28 """
29
30 Wind data
31 """
32 wind_data = wind_tdms_file["W03-7-1"]
33 # Time-axis wind
34 dt_wind = (wind_data["timestamp"][1]-wind_data["timestamp"][0])*10**(-9) # converted from
      nanoseconds to seconds
35 Fs_wind = int(np.round(1/dt_wind))
36
37 magnitude_raw = wind_data["magnitude"][:]
38 direction_raw = wind_data["direction"][:]
39 vertical_velocity_raw = wind_data["vertical_velocity"][:]
40 status = wind_data["status_code"][:]
41
42 rawWind = np.transpose(np.array([magnitude_raw, direction_raw, vertical_velocity_raw]))
43
44 # Cleaning up the wind-measurements
45 (cleanWind, error_ratio) = cd.remove_error(rawWind, Fs_wind, status)
46 magnitude = cleanWind[:, 0]
47 direction = cleanWind[:, 1]
48 vertical_velocity = cleanWind[:, 2]
49 print(f'Error ratio is: {error_ratio}')
50
51
52 # Moving mean of magnitude and direction
53 window_size_1min = 60 # [sec]
54 window_size_10min = 600 # [sec]
55
56 (t_wind, meanWind_1min) = moving_mean(magnitude, window_size_1min*Fs_wind, Fs_wind)
57 (t_wind, meanWind_10min) = moving_mean(magnitude, window_size_10min*Fs_wind, Fs_wind)
58 (t_wind, meanDirection_10min) = moving_mean(direction, window_size_10min*Fs_wind, Fs_wind)
59
60
61 """
62
63 Acceleration data
64 """
65 acceleration_data = acc_tdms_file["acceleration_data"]
66
67 # Time-axis accelerations
68 dt_acc = (acceleration_data["timestamp"][1]-acceleration_data["timestamp"][0])*10**(-9) #
      converted from nanoseconds to seconds
69 Fs_acc = int(np.round(1/dt_acc))
70 g = 9.81 # [m/s^2]
71
72 # Hanger 1 (Accelerations given in m/s^2)
73 conversion_factor1x = 0.10145
74 conversion_factor1y = 0.10077
75 A02_1x = acceleration_data["A02-1x"][:] * g / conversion_factor1x
76 A02_1y = acceleration_data["A02-1y"][:] * g / conversion_factor1y
77 acc1_raw = np.transpose(np.array([A02_1x, A02_1y]))
78 (acc1_clean, stdtrig1) = cd.remove_std(acc1_raw, Fs_acc, 10)
79 A02_1x = acc1_clean[:, 0] - np.mean(acc1_clean[:, 0])
80 A02_1y = acc1_clean[:, 1] - np.mean(acc1_clean[:, 1])
81 if stdtrig1:
82     print(f'Acceleration data for Hanger 1 was adjusted')
83
84 # Hanger 2 (Accelerations given in m/s^2)
85 conversion_factor2x = 0.10286
86 conversion_factor2y = 0.10106
87 A02_2x = acceleration_data["A02-2x"][:] * g / conversion_factor2x

```

```

88 A02_2y = acceleration_data["A02-2y"][:]*g/conversion_factor2y
89 acc2_raw = np.transpose(np.array([A02_2x, A02_2y]))
90 (acc2_clean, stdtrig2) = cd.remove_std(acc2_raw, Fs_acc, 20)
91 A02_2x = acc2_clean[:, 0] - np.mean(acc2_clean[:, 0])
92 A02_2y = acc2_clean[:, 1] - np.mean(acc2_clean[:, 1])
93 if stdtrig2:
94     print(f'Acceleration data for Hanger 2 was adjusted')
95
96 # Hanger 3 (Accelerations given in m/s^2)
97 conversion_factor3x = 0.09897
98 conversion_factor3y = 0.10239
99 A02_3x = acceleration_data["A02-3x"][:]*g/conversion_factor3x
100 A02_3y = acceleration_data["A02-3y"][:]*g/conversion_factor3y
101 acc3_raw = np.transpose(np.array([A02_3x, A02_3y]))
102 (acc3_clean, stdtrig3) = cd.remove_std(acc3_raw, Fs_acc, 20)
103 A02_3x = acc3_clean[:, 0] - np.mean(acc3_clean[:, 0])
104 A02_3y = acc3_clean[:, 1] - np.mean(acc3_clean[:, 1])
105 if stdtrig3:
106     print(f'Acceleration data for Hanger 3 was adjusted')
107
108 t_acc = np.arange(0, len(A02_1x))*dt_acc
109
110
111 ##### Acceleration response
112
113 # Hanger 1
114 fig, ax = plt.subplots(4, 1, sharex=True)
115 plt.suptitle('Hanger 1')
116
117 plt.subplot(4, 1, 1)
118 plt.plot(t_acc, A02_1x)
119 plt.ylabel(r'$A_{x}$ [m/s^2]$')
120 plt.grid()
121
122 plt.subplot(4, 1, 2)
123 plt.plot(t_acc, A02_1y)
124 plt.ylabel(r'$A_{y}$ [m/s^2]$')
125 plt.grid()
126
127 plt.subplot(4, 1, 3)
128 plt.plot(t_wind, magnitude)
129 plt.plot(t_wind, meanWind_10min, linewidth=1.2)
130 plt.ylabel(r'$Magnitude$ [m/s]$')
131 plt.grid()
132
133 plt.subplot(4, 1, 4)
134 plt.plot(t_wind, direction)
135 plt.plot(t_wind, meanDirection_10min, linewidth=1.2)
136 plt.ylabel(r'$\phi$ [degree]$')
137 plt.grid()
138
139 plt.xlabel('t [s]')
140 plt.show()
141
142
143 # Hanger 2
144 fig, ax = plt.subplots(4, 1, sharex=True)
145 plt.suptitle('Hanger 2')
146
147 plt.subplot(4, 1, 1)
148 plt.plot(t_acc, A02_2x)
149 plt.ylabel(r'$A_{x}$ [m/s^2]$')
150 plt.grid()
151
152 plt.subplot(4, 1, 2)
153 plt.plot(t_acc, A02_2y)

```

```

154 plt.ylabel(r'$A_{y}$ [m/s^2]$')
155 plt.grid()
156
157 plt.subplot(4, 1, 3)
158 plt.plot(t_wind, magnitude)
159 plt.plot(t_wind, meanWind_10min, linewidth=1.2)
160 plt.ylabel(r'$Magnitude$ [m/s]$')
161 plt.grid()
162
163 plt.subplot(4, 1, 4)
164 plt.plot(t_wind, direction)
165 plt.plot(t_wind, meanDirection_10min, linewidth=1.2)
166 plt.ylabel(r'$\phi$ [\degree]$')
167 plt.grid()
168
169 plt.xlabel('t [s]')
170 plt.show()
171
172
173 # Hanger 3
174 fig, ax = plt.subplots(4, 1, sharex=True)
175 plt.suptitle('Hanger 3')
176
177 plt.subplot(4, 1, 1)
178 plt.plot(t_acc, A02_3x)
179 plt.ylabel(r'$A_{x}$ [m/s^2]$')
180 plt.grid()
181
182 plt.subplot(4, 1, 2)
183 plt.plot(t_acc, A02_3y)
184 plt.ylabel(r'$A_{y}$ [m/s^2]$')
185 plt.grid()
186
187 plt.subplot(4, 1, 3)
188 plt.plot(t_wind, magnitude)
189 plt.plot(t_wind, meanWind_10min, linewidth=1.2)
190 plt.ylabel(r'$Magnitude$ [m/s]$')
191 plt.grid()
192
193 plt.subplot(4, 1, 4)
194 plt.plot(t_wind, direction)
195 plt.plot(t_wind, meanDirection_10min, linewidth=1.2)
196 plt.ylabel(r'$\phi$ [\degree]$')
197 plt.grid()
198
199 plt.xlabel('t [s]')
200 plt.show()
201
202 ##### Turbulence intensity
203
204 l_section = 30 # [min]
205 N_sections = np.round(len(magnitude)/(l_section*Fs_wind*60)).astype(int)
206 I_u = np.zeros(N_sections)
207
208
209 for i in range(N_sections):
210     meanWind_turbulence = np.mean(magnitude[i*(60*Fs_wind*l_section):(i+1)*(60*Fs_wind*
211         l_section)])
212     turbulence = magnitude[i*(60*Fs_wind*l_section):(i+1)*(60*Fs_wind*l_section)] -
213         meanWind_turbulence
214     std_turbulence = np.std(turbulence)
215     I_u[i] = std_turbulence / meanWind_turbulence
216
217 plt.figure()
218 plt.suptitle('Turbulence Intensity', fontsize=15)
219 plt.plot(np.linspace(0+l_section*60/2, t_wind[-1]-l_section*60/2, N_sections), I_u, '-')

```

```

218 plt.ylabel('Turbulence Intensity', fontsize=13)
219 plt.xlabel('Time [sec]', fontsize=13)
220 plt.xticks(fontsize=11)
221 plt.yticks(fontsize=11)
222 plt.xlim([0, t_wind[-1]])
223 plt.grid()
224 plt.show()
225
226 ##### Polar plot direction
227
228 polar_direction_mean = np.deg2rad(meanDirection_10min)
229 polar_direction_mean_converted = polar_direction_mean - np.pi
230
231 polar_direction = np.deg2rad(direction)
232 polar_direction_converted = polar_direction - np.pi # Converts so it shows where the wind
           comes from
233 t_polar = t_wind
234
235 plt.figure()
236 ax = plt.subplot(111, projection='polar')
237 ax.set_theta_offset(np.deg2rad(90))
238 plt.polar(polar_direction_converted, t_polar, '-', linewidth=0.4)
239 plt.polar(polar_direction_mean_converted, t_polar, '-', linewidth=0.9)
240 plt.show()
241
242
243 #####
244 """"
245 STANDARD DEVIATION VS. MEAN WIND
246 """"
247
248 ##### Standard deviation of accelerations VS mean wind: X-direction
249
250 t_section = 28800 # can convert to separate lines for different sections
251 N_sections = np.round(len(t_wind)/(Fs_wind*t_section)).astype(int)
252
253 V = np.arange(0, 30, 0.25)
254 std_1x = np.zeros((N_sections, len(V)))
255 std_2x = np.zeros((N_sections, len(V)))
256 std_3x = np.zeros((N_sections, len(V)))
257
258
259 plt.figure()
260 plt.suptitle('Accelerations in x-direction', fontsize=13)
261 for j in range(N_sections):
262     V_mean = np.zeros(len(V))
263
264     meanWind_subset = meanWind_1min[(Fs_wind * t_section * j): (Fs_wind * t_section * (j
           +1))]
265     A02_1x_subset = A02_1x[(Fs_acc * t_section * j): (Fs_acc * t_section * (j + 1))]
266     A02_2x_subset = A02_2x[(Fs_acc * t_section * j): (Fs_acc * t_section * (j + 1))]
267     A02_3x_subset = A02_3x[(Fs_acc * t_section * j): (Fs_acc * t_section * (j + 1))]
268
269     for i in range(len(V)-1):
270         V_mean_indexes = np.where(np.logical_and(meanWind_subset > V[i], meanWind_subset <
           V[i+1]))[0]
271         if len(V_mean_indexes) != 0:
272             acc_indexes = np.round(V_mean_indexes*Fs_acc/Fs_wind).astype(int)
273             std_1x[j, i] = np.std(A02_1x_subset[acc_indexes])
274             std_2x[j, i] = np.std(A02_2x_subset[acc_indexes])
275             std_3x[j, i] = np.std(A02_3x_subset[acc_indexes])
276             V_mean[i] = 1 / 2 * (V[i] + V[i + 1])
277
278     plt.plot(sorted(V_mean), std_1x[j, :], '-', color='r')
279     plt.plot(sorted(V_mean), std_2x[j, :], '-', color='b')
280     plt.plot(sorted(V_mean), std_3x[j, :], '-', color='y')

```



```

281 plt.ylabel(r'Standard deviation of accelerations  $[m/s^2]$ ', fontsize=13)
282 plt.xlabel('Mean wind [m/s]', fontsize=13)
283 plt.legend(['Hanger 1', 'Hanger 2', 'Hanger 3'], fontsize=11)
284 plt.xticks(fontsize=11)
285 plt.yticks(fontsize=11)
286 plt.grid()
287 plt.show()
288
289
290
291 ##### Standard deviation VS mean wind: Y-direction
292
293 std_1y = np.zeros((N_sections, len(V)))
294 std_2y = np.zeros((N_sections, len(V)))
295 std_3y = np.zeros((N_sections, len(V)))
296
297
298 plt.figure()
299 plt.suptitle('Accelerations in y-direction', fontsize=13)
300 for j in range(N_sections):
301     V_mean = np.zeros(len(V))
302
303     meanWind_subset = meanWind_1min[(Fs_wind * t_section * j): (Fs_wind * t_section * (j
304         +1))]
305     A02_1y_subset = A02_1y[(Fs_acc * t_section * j): (Fs_acc * t_section * (j + 1))]
306     A02_2y_subset = A02_2y[(Fs_acc * t_section * j): (Fs_acc * t_section * (j + 1))]
307     A02_3y_subset = A02_3y[(Fs_acc * t_section * j): (Fs_acc * t_section * (j + 1))]
308
309     for i in range(len(V)-1):
310         V_mean_indexes = np.where(np.logical_and(meanWind_subset > V[i], meanWind_subset <
311             V[i+1]))[0]
312         if len(V_mean_indexes) != 0:
313             acc_indexes = np.round(V_mean_indexes*Fs_acc/Fs_wind).astype(int)
314             std_1y[j, i] = np.std(A02_1y_subset[acc_indexes])
315             std_2y[j, i] = np.std(A02_2y_subset[acc_indexes])
316             std_3y[j, i] = np.std(A02_3y_subset[acc_indexes])
317             V_mean[i] = 1 / 2 * (V[i] + V[i + 1])
318
319     plt.plot(sorted(V_mean), std_1y[j, :], '-', color='r')
320     plt.plot(sorted(V_mean), std_2y[j, :], '-', color='b')
321     plt.plot(sorted(V_mean), std_3y[j, :], '-', color='y')
322
323 plt.ylabel(r'Standard deviation of accelerations  $[m/s^2]$ ', fontsize=13)
324 plt.xlabel('Mean wind [m/s]', fontsize=13)
325 plt.legend(['Hanger 1', 'Hanger 2', 'Hanger 3'], fontsize=11)
326 plt.xticks(fontsize=11)
327 plt.yticks(fontsize=11)
328 plt.grid()
329 plt.show()
330
331 ""
332 VIBRATION FREQUENCY ANALYSIS
333 ""
334
335 ##### Theoretical shedding frequencies
336 St = 0.185
337 D = 0.086 # [m]
338 f_shedding = St*meanWind_1min/D
339 f_inline = 2*St*meanWind_1min/D
340
341
342 ##### Spectrograms
343
344 # Hanger 1

```

```

345 f, t, Sxx1 = signal.spectrogram(A02_1x, fs=Fs_acc, nperseg=Fs_acc*10, noverlap=Fs_acc*5)
346 f, t, Syy1 = signal.spectrogram(A02_1y, fs=Fs_acc, nperseg=Fs_acc*10, noverlap=Fs_acc*5)
347
348 # Hanger 2
349 f, t, Sxx2 = signal.spectrogram(A02_2x, fs=Fs_acc, nperseg=Fs_acc*10, noverlap=Fs_acc*5)
350 f, t, Syy2 = signal.spectrogram(A02_2y, fs=Fs_acc, nperseg=Fs_acc*10, noverlap=Fs_acc*5)
351
352 # Hanger 3
353 f, t, Sxx3 = signal.spectrogram(A02_3x, fs=Fs_acc, nperseg=Fs_acc*10, noverlap=Fs_acc*5)
354 f, t, Syy3 = signal.spectrogram(A02_3y, fs=Fs_acc, nperseg=Fs_acc*10, noverlap=Fs_acc*5)
355
356
357 """ y-lim conditions in spectrogram plots
358 if St*np.min(magnitude)/D-5 < 0:
359     ymin_CF = 0
360 else:
361     ymin_CF = St*np.min(magnitude)/D-5
362 if St*np.max(magnitude)/D+5 > Fs_acc/2:
363     ymax_CF = 100
364 else:
365     ymax_CF = St*np.max(magnitude)/D+5
366
367
368 if 2*St*np.min(magnitude)/D-5 < 0:
369     ymin_IL = 0
370 else:
371     ymin_IL = 2*St*np.min(magnitude)/D-5
372 if 2*St*np.max(magnitude)/D+5 > Fs_acc/2:
373     ymax_IL = 100
374 else:
375     ymax_IL = 2*St*np.max(magnitude)/D+5
376
377 """ Plots of spectrogram, log-scale
378
379 # Hanger 1
380
381 fig, ax = plt.subplots(2, 1, sharex=True)
382 plt.suptitle('Hanger 1', fontsize=15)
383
384 plt.subplot(2, 1, 1)
385 plt.title('x-direction', fontsize=13)
386 plt.pcolormesh(t, f, Sxx1, norm=matplotlib.colors.LogNorm())
387 plt.plot(t_wind, f_shedding, color='red', alpha=0.15, linewidth=0.9)
388 plt.ylabel('f [Hz]', fontsize=13)
389 plt.yticks(fontsize=11)
390 plt.ylim(ymin_CF, ymax_CF)
391
392 plt.subplot(2, 1, 2)
393 plt.title('y-direction', fontsize=13)
394 plt.pcolormesh(t, f, Syy1, norm=matplotlib.colors.LogNorm())
395 plt.plot(t_wind, f_inline, color='red', alpha=0.15, linewidth=0.9)
396 plt.ylabel('f [Hz]', fontsize=13)
397 plt.ylim(ymin_IL, ymax_IL)
398 plt.xlabel('Time [sec]', fontsize=13)
399 plt.xticks(fontsize=11)
400 plt.yticks(fontsize=11)
401 plt.show()
402
403
404 # Hanger 2
405 fig, ax = plt.subplots(2, 1, sharex=True)
406 plt.suptitle('Hanger 2')
407
408 plt.subplot(2, 1, 1)
409 plt.title('x-direction')
410 plt.pcolormesh(t, f, Sxx2, norm=matplotlib.colors.LogNorm())

```

```

411 plt.plot(t_wind, f_shedding, color='red', alpha=0.15, linewidth=0.9)
412 plt.ylabel('f [Hz]')
413 plt.ylim(ymin_CF, ymax_CF)
414
415 plt.subplot(2, 1, 2)
416 plt.title('y-direction')
417 plt.pcolormesh(t, f, Syy2, norm=matplotlib.colors.LogNorm())
418 plt.plot(t_wind, f_inline, color='red', alpha=0.15, linewidth=0.9)
419 plt.ylabel('f [Hz]')
420 plt.ylim(ymin_IL, ymax_IL)
421 plt.xlabel('Time [sec]')
422 plt.show()
423
424
425 # Hanger 3
426 fig, ax = plt.subplots(2, 1, sharex=True)
427 plt.suptitle('Hanger 3')
428
429 plt.subplot(2, 1, 1)
430 plt.title('x-direction')
431 plt.pcolormesh(t, f, Sxx3, norm=matplotlib.colors.LogNorm())
432 plt.plot(t_wind, f_shedding, color='red', alpha=0.15, linewidth=0.9)
433 plt.ylabel('f [Hz]')
434 plt.ylim(ymin_CF, ymax_CF)
435
436 plt.subplot(2, 1, 2)
437 plt.title('y-direction')
438 plt.pcolormesh(t, f, Syy3, norm=matplotlib.colors.LogNorm())
439 plt.plot(t_wind, f_inline, color='red', alpha=0.15, linewidth=0.9)
440 plt.ylabel('f [Hz]')
441 plt.ylim(ymin_IL, ymax_IL)
442 plt.xlabel('Time [sec]')
443 plt.show()
444
445
446 """
447
448 Displacements
449 """
450
451 """ Displacements through frequency domain analysis
452
453 accelerations = np.array([A02_1x, A02_1y, A02_2x, A02_2y, A02_3x, A02_3y]) # [m/s^2]
454
455 # Integrate by fft
456 fourier_amp_acc = np.fft.fft(accelerations, accelerations.shape[1], axis=1)
457 freq = np.fft.fftfreq(fourier_amp_acc.shape[1], dt_acc)
458 freq[np.abs(freq) < 1.5] = 1
459 fourier_amp_acc[:, np.abs(freq) < 1.5] = 0
460
461 fourier_amp_disp = -fourier_amp_acc / ((2 * np.pi * np.abs(np.transpose(freq[:, np.newaxis
462 ]))) ** 2)
463 displacements = np.fft.ifft(fourier_amp_disp, accelerations.shape[1], axis=1) # [m]
464 displacements_mm = displacements*1000 # [mm]
465
466 for i in range(3):
467     fig, ax = plt.subplots(2, 1, sharex=True)
468     plt.suptitle(f'Displacements hanger {i+1}')
469
470     plt.subplot(2, 1, 1)
471     plt.title('x-direction')
472     plt.plot(t_acc, np.real(displacements_mm[i*2, :]))
473     plt.ylabel('Displacement [mm]')
474     plt.grid()
475

```

```

476     plt.subplot(2, 1, 2)
477     plt.title('y-direction')
478     plt.plot(t_acc, np.real(displacements_mm[i*2+1, :]))
479     plt.ylabel('Displacement [mm]')
480     plt.grid()
481
482     plt.xlabel('Time [sec]')
483     plt.show()
484
485
486     ##### Standard deviation of displacements in x-direction
487
488     V = np.arange(0, 30, 0.25)
489     V_mean = np.zeros(len(V))
490
491     std_1x_disp = np.zeros(len(V))
492     std_2x_disp = np.zeros(len(V))
493     std_3x_disp = np.zeros(len(V))
494
495     plt.figure()
496     plt.suptitle('Displacements in x-direction', fontsize=13)
497     for i in range(len(V)-1):
498         V_mean_indexes = np.where(np.logical_and(meanWind_1min > V[i], meanWind_1min < V[i+1])
499             )[0]
500         if len(V_mean_indexes) != 0:
501             disp_indexes = np.round(V_mean_indexes*Fs_acc/Fs_wind).astype(int)
502             std_1x_disp[i] = np.std(displacements_mm[0, disp_indexes])
503             std_2x_disp[i] = np.std(displacements_mm[2, disp_indexes])
504             std_3x_disp[i] = np.std(displacements_mm[4, disp_indexes])
505             V_mean[i] = 1 / 2 * (V[i] + V[i + 1])
506
507     plt.plot(sorted(V_mean), std_1x_disp[:, ], '-', color='r')
508     plt.plot(sorted(V_mean), std_2x_disp[:, ], '-', color='b')
509     plt.plot(sorted(V_mean), std_3x_disp[:, ], '-', color='y')
510
511     plt.ylabel(r'Standard deviation of displacements $[mm]$', fontsize=13)
512     plt.xlabel('Mean wind [m/s]', fontsize=13)
513     plt.legend(['Hanger 1', 'Hanger 2', 'Hanger 3'], fontsize=11)
514     plt.xticks(fontsize=11)
515     plt.yticks(fontsize=11)
516     plt.grid()
517     plt.show()
518
519     # Standard deviation of displacements in y-direction
520
521     V = np.arange(0, 30, 0.25)
522     V_mean = np.zeros(len(V))
523
524     std_1y_disp = np.zeros(len(V))
525     std_2y_disp = np.zeros(len(V))
526     std_3y_disp = np.zeros(len(V))
527
528     plt.figure()
529     plt.suptitle('Displacements in y-direction')
530     for i in range(len(V)-1):
531         V_mean_indexes = np.where(np.logical_and(meanWind_1min > V[i], meanWind_1min < V[i+1])
532             )[0]
533         if len(V_mean_indexes) != 0:
534             disp_indexes = np.round(V_mean_indexes*Fs_acc/Fs_wind).astype(int)
535             std_1y_disp[i] = np.std(displacements_mm[1, disp_indexes])
536             std_2y_disp[i] = np.std(displacements_mm[3, disp_indexes])
537             std_3y_disp[i] = np.std(displacements_mm[5, disp_indexes])
538             V_mean[i] = 1 / 2 * (V[i] + V[i + 1])
539
540     plt.plot(sorted(V_mean), std_1y_disp[:, ], '-', color='r')
541     plt.plot(sorted(V_mean), std_2y_disp[:, ], '-', color='b')

```

```
540 plt.plot(sorted(V_mean), std_3y_disp[:, '-'], color='y')
541
542 plt.ylabel(r'Standard deviation of displacements [mm]')
543 plt.xlabel('Mean wind [m/s]')
544 plt.legend(['Hanger 1', 'Hanger 2', 'Hanger 3'])
545 plt.grid()
546 plt.show()
```

